MEASUREMENT OF THE $B^\circ - \bar{B}^\circ$ MIXING PARAMETER USING DIMUON EVENTS COLLECTED WITH THE DØ DETECTOR

by

Eric B. James

A Dissertation Submitted to the Faculty of the

DEPARTMENT OF PHYSICS

In Partial Fulfillment of the Requirements
For the Degree of

DOCTOR OF PHILOSOPHY

In the Graduate College

THE UNIVERSITY OF ARIZONA

1995

STATEMENT BY AUTHOR

This dissertation has been submitted in partial fulfillment of requirements for an advanced degree at The University of Arizona and is deposited in the University Library to be made available to borrowers under rules of the Library.

Brief quotations from this dissertation are allowable without special permission, provided that accurate acknowledgement of source is made. Requests for permission for extended quotation from or reproduction of this manuscript in whole or in part may be granted by the head of the major department or the Dean of the Graduate College when in his or her judgement the proposed use of the material is in the interests of scholarship. In all other instances, however, permission must be obtained from the author.

SIGNED: _____

ACKNOWLEDGEMENTS

A large number of people have played a role in helping me to complete this dissertation, and I would like to take this opportunity to thank as many of those people as possible. First and foremost, I would like to thank my advisor Ken Johns whose guidance, support, and friendship have been invaluable over the course of my graduate studies. In addition, I would like to extend a particular thanks to Alex Smith and David Fein who have been my compatriots in this endeavor from the beginning. Without their companionship it's certain that life in Batavia would have been most unpleasant. I would also like to thank all the members of the high energy group at the University of Arizona and my fellow collaborators on the DØ experiment. In particular, Dave Hedin and Andrzej Zieminski deserve special mention due to the large amount of guidance which they provided over the course of this analysis.

A special thanks also to my other friends and drinking buddies who have been a major part of my life here in Tucson over the past six years. In particular, I would like to thank Kit Wellman, Paige Coelho, Michael "Kimone" Tooke, Jennifer Toothacker, Ron Norton, Lon Gallagher, Patrick McGuire, and Tammy Ward. Kudos also to the Buffet Bar and Crockpot which perhaps too often served as a second home during my time in Tucson. A special mention also to my long pals David Friedman and Laura Fineberg who have been there for me as long as I can remember. Finally, I want to thank my entire family for their continued support over the course of the long number of years which it has taken me to reach this point in my academic career. I am indeed fortunate to have such a supportive and loving family.

To my parents.

TABLE OF CONTENTS

LIST OF FIGURES

LIST OF TABLES

ABSTRACT

The DØ experiment at Fermilab has determined the $B^\circ - \bar{B}^\circ$ mixing probability χ using dimuon events produced in $p\bar{p}$ collisions at $\sqrt{s} = 1.8$ TeV. Using a sample of 183 dimuon events, we have determined the time and flavor averaged mixing probability χ to be $0.09 \pm 0.04(stat) \pm 0.03(sys)$ in agreement with the present world average for this parameter.

Chapter 1

Introduction

1.1 The Standard Model

The primary goal of modern particle physics is to provide a detailed understanding of the fundamental components of nature and the forces which regulate their interactions. The immense amount of experimental data which has been collected over the past several decades from both accelerator and non-accelerator experiments has led to the development of the Standard Model (SM) which has proven extremely successful at describing the phenomenology of high energy particle interactions. The Standard Model is a quantum field theory which is based upon the idea of local gauge invariance [1]. The basic components of the Standard Model are an $SU(2)_L \otimes U(1)_Y$ gauge theory which describes electroweak interactions and an $SU(3)_C$ gauge theory referred to as Quantum Chromodynamics (QCD) which describes strong interactions. At the present time there is no experimental result which significantly contradicts the description of matter provided by the Standard Model.

In the Standard Model matter is composed of twelve fundamental spin 1/2 particles known as fermions each of which also has a corresponding fundamental antiparticle. The fermions are grouped into three parallel sets of lepton and quark

doublets.

$$\begin{pmatrix} \nu_e \\ e \end{pmatrix} \quad \begin{pmatrix} \nu_\mu \\ \mu \end{pmatrix} \quad \begin{pmatrix} \nu_\tau \\ \tau \end{pmatrix} \quad \text{Leptons}$$

$$\begin{pmatrix} u \\ d \end{pmatrix} \quad \begin{pmatrix} c \\ s \end{pmatrix} \quad \begin{pmatrix} t \\ b \end{pmatrix} \quad \text{Quarks} \tag{1.1}$$

With the recent discovery of the top quark [2][3], the existence of all twelve fermions has been experimentally confirmed. The existence of additional quark and lepton families is ruled out by experimental measurements of the Z° decay width to invisible particles ($Z^\circ \rightarrow \nu\bar{\nu}$) at LEP [4][5][6][7].

Leptons are distinguished from quarks by their inability to interact via the strong interaction. Each lepton family consists of one charged lepton (e,μ,τ) and one uncharged neutrino (ν_e,ν_μ,ν_τ). Lepton number, defined as the difference between the number of particles and antiparticles of a specific lepton family present in an isolated system, is found to be independently conserved for each of the three lepton families in all particle interactions. The existence of these separate lepton numbers and mass differences are the only known distinctions between the three charged leptons. Since neutrinos have zero charge, their interaction with matter is restricted to the weak force. Until recently neutrinos were assumed to be massless particles. However, recent measurements of solar and atmospheric neutrino fluxes are suggestive of oscillations between different neutrino flavors which would require the existence of mass differences between the different flavor states. A number of neutrino oscillation experiments are presently in the process of studying this question further [8]. Some specific properties of leptons are listed in Table 1-1.

Two properties which characterize QCD are called asymptotic freedom and infrared slavery. The first means that as $Q^2 \rightarrow \infty$ where Q is defined as the magnitude of the momentum transfer in a particle collision, the strong coupling

Lepton	Charge	Mass (MeV/c^2)
ν_e	0	$< 5.1 \times 10^{-6}$
e	-1	.51100
ν_μ	0	< 0.27
μ	-1	105.66
ν_τ	0	< 31
τ	-1	1777.1

Table 1-1: Properties of leptons in the Standard Model.

constant $\alpha_s(Q^2) \rightarrow 0$ and the quarks appear "free". The second is that in the limit as $Q^2 \rightarrow 0$ quarks are confined within hadrons although this experimental fact is not proven. Quarks are assumed to carry color charge of one of three colors usually referred to as red, green, and blue. While quarks carry color, the observed spectra of hadrons which they form appear as color neutral objects. Properties of the different quark flavor states are given in Table 1-2.

In the gauge theories which describe strong and electroweak interactions the forces between particles are mediated by gauge vector bosons (particles with integral spin). In both the strong and electroweak theories these bosons can be identified with the vector gauge fields which are introduced to preserve the local gauge invariance of the theories. A total of eight gauge fields are required in strong interaction theory to maintain local gauge invariance under $SU(3)_C$, and the vector bosons identified with these fields are known as gluons. Strong interactions are a consequence of couplings which exist between specific color states of individual quarks due to the existence of the eight different gauge fields. Quarks interact strongly by exchanging color through the gluons which are associated with these fields. Since the symmetry of the $SU(3)_C$ gauge theory is unbroken, each of the eight gluons is massless. In addition, each of the gluons carries its own color charge and hence gluons are also allowed to interact with one another. This self-

Quark Flavor	Quark Charge	Effective Mass (GeV/c^2)
Up	+ 2/3	0.002 - 0.008
Down	− 1/3	0.005 - 0.015
Charm	+ 2/3	1.3 - 1.5
Strange	− 1/3	0.1 - 0.3
Top	+ 2/3	160 - 190
Bottom	− 1/3	4.7 - 5.3

Table 1-2: Properties of quarks in the Standard Model.

interaction is in direct contrast to the electromagnetic interaction where the force propagating bosons are charge neutral photons which cannot interact directly with each other.

In the Weinberg-Salam model which describes electroweak interactions four gauge fields are required to ensure local gauge invariance under $SU(2)_L \otimes U(1)_Y$. In the unbroken symmetry of this gauge theory the vector bosons associated with these gauge fields would remain massless. However, the short range of weak force implies that the propagating bosons associated with this force must be massive. These bosons are found to acquire mass through the introduction of the Higgs mechanism [9] which spontaneously breaks the gauge symmetry of the theory while allowing it to remain renormalizable. The propagators of the charged current weak interaction are known as the $W^{\pm}$ bosons, and the propagator of the neutral current weak interaction is referred to as the Z° boson. The respective masses of the $W^{\pm}$ and Z° bosons are 80 GeV/c^2 and 91 GeV/c^2. The one remaining vector boson which is still massless in the broken symmetry created by the Higgs mechanism is the photon which mediates the electromagnetic interaction.

A unique property of weak charged current interactions is that quark and lepton flavor are not conserved quantities. Each of the quark and lepton doublets shown in (1.1) has a corresponding weak isospin doublet which contains the left handed

forms of the fermions in the doublet. The lepton and quark flavors within each weak isospin doublet are coupled via the charged current, and flavor changing transitions between the two states are allowed. Conversely, right handed forms of fermions do not couple via the charged current and hence no flavor changing transitions between right handed flavor states are permitted.

It has been experimentally demonstrated that the weak charged current also couples quarks between different weak isospin doublets. This experimental fact implies that the quark eigenstates involved in the weak interaction are not equivalent to the mass eigenstates. In order to account for this phenomenon, the weak eigenstates of the isospin doublets are taken to be a mixture of the three flavor states. The standard method method for accomplishing this modification is to write the down type quark state within each weak isospin doublet as a linear combination of the three down quark mass states.

$$\begin{pmatrix} d' \\ s' \\ b' \end{pmatrix} = \begin{pmatrix} V_{ud} & V_{us} & V_{ub} \\ V_{cd} & V_{cs} & V_{cb} \\ V_{td} & V_{ts} & V_{tb} \end{pmatrix} \begin{pmatrix} d \\ s \\ b \end{pmatrix} \tag{1.2}$$

The matrix in the above parameterization is known as the Cabbibo-Kobayashi-Maskawa (CKM) matrix. The linear combinations of the down quark mass states which are used to construct the weak eigenstates of the isospin doublets are described by the mixing angles contained in this matrix. The transition amplitude between two different quark flavors has a coupling strength which is directly related to the corresponding CKM matrix element. Thus, the general form of the weak charged current in this parameterization is

$$J^{\mu} = \begin{pmatrix} \overline{u} & \overline{c} & \overline{t} \end{pmatrix} \frac{\gamma_{\mu}(1-\gamma^5)}{2} V_{CKM} \begin{pmatrix} d \\ s \\ b \end{pmatrix}. \tag{1.3}$$

1.2 $B^\circ - \bar{B}^\circ$ Mixing

As discussed in the previous section particle interactions which proceed via the weak interaction are not required to conserve quark flavor. In the b quark system interactions of this type lead to mixing between neutral b mesons and their respective antiparticles. Analogous to the neutral kaon system, the flavor eigenstates of the strong interaction in the neutral b meson system ($|B^\circ\rangle$, $|\bar{B}^\circ\rangle$) are not equivalent to the eigenstates of the weak interaction. However, since the observation of a neutral b meson state at any given time must result in the detection of one mass state or the other, the weak eigenstates can be constructed from a linear combination of the flavor eigenstates. Although the Standard Model predicts CP violation in the b quark system, the magnitude of such effects are expected to be small with respect to mixing. Therefore, in dealing with mixing it is possible to make an approximation in which CP is treated as a good quantum number of the weak eigenstates. Due to the fact that the CP quantum mechanical operator has eigenvalues of $\pm$ 1, the weak eigenstates can be constructed as

$$CP|B_1\rangle = |B_1\rangle = \frac{1}{\sqrt{2}}(|B^\circ\rangle + |\bar{B}^\circ\rangle) \tag{1.4}$$

and

$$CP|B_2\rangle = -|B_2\rangle = \frac{1}{\sqrt{2}}(|\bar{B}^\circ\rangle - |B^\circ\rangle). \tag{1.5}$$

The quantum mechanical time evolution of the weak eigenstates can be used to construct the future composition of a neutral b meson state which is initially produced as a $|B^\circ\rangle$ or a $|\bar{B}^\circ\rangle$. For example, an initial state of $|B^\circ\rangle$ can be written in terms of the weak eigenstates as

$$|B^\circ(t=0)\rangle = |B^\circ\rangle = \frac{1}{\sqrt{2}}(|B_1\rangle + |B_2\rangle). \tag{1.6}$$

Quantum mechanical time evolution of the weak eigenstates leads to a construction of the same state after some time t such that

$$|B^\circ(t)\rangle = \frac{1}{\sqrt{2}}(|B_1\rangle e^{-im_1 t-\frac{\Gamma_1}{2}t} + |B_2\rangle e^{-im_2 t-\frac{\Gamma_2}{2}t}) \tag{1.7}$$

where m_i and Γ_i represent the mass and decay widths of the weak eigenstates.

In order to formulate the probabilities for observing the neutral b meson as a $|B^\circ\rangle$ or a $|\bar{B}^\circ\rangle$ after some time t, it is necessary to convert the expression for $|B(t)\rangle$ into one which is written in terms of the strong eigenstates. Substitution of the expressions for the weak eigenstates found in (1.4) and (1.5) in addition to some mathematical manipulation leads to the formulation

$$|B^\circ(t)\rangle = \frac{1}{2}e^{-im_1 t-\frac{\Gamma_1}{2}t}(|B^\circ\rangle(1 + e^{-i\Delta m t-\frac{\Delta\Gamma}{2}t}) + |\bar{B}^\circ\rangle(1 - e^{-i\Delta m t-\frac{\Delta\Gamma}{2}t})) \tag{1.8}$$

where $\Delta m \equiv m_2 - m_1$ and $\Delta\Gamma \equiv \Gamma_2 - \Gamma_1$.

The probability for finding the initial $|B^\circ\rangle$ state in a $|\bar{B}^\circ\rangle$ state after time t can be extracted as the square of the amplitude of the $|\bar{B}^\circ\rangle$ term in the expression for $|B(t)\rangle$ as shown:

$$[Prob(B^\circ \to \bar{B}^\circ)](t) = \frac{1}{4}|e^{-im_1 t-\frac{\Gamma_1}{2}t}|^2|(1 - e^{-i\Delta m t-\frac{\Delta\Gamma}{2}t})|^2. \tag{1.9}$$

After further mathematical manipulation the expression in (1.9) becomes

$$[Prob(B^\circ \to \bar{B}^\circ)](t) = \frac{1}{4}e^{-\Gamma_1 t}(1 + e^{-\Delta\Gamma t} - 2e^{-\frac{\Delta\Gamma}{2}t}cos(\Delta m t)). \tag{1.10}$$

At this point it is possible to make several approximations to (1.10) which are unique to mixing between neutral b mesons. These approximations result from the fact that the difference in the decay width between neutral b mesons and their respective antiparticles is expected to be small. This situation provides a direct contrast to the situation observed in the kaon system where the K_S and K_L have very different decay widths. The approximation which one makes in the

b quark system is that $\Gamma = \Gamma_1 \sim \Gamma_2$ in conjunction with the slightly stronger constraints that $\Delta\Gamma \ll \Delta m, \Gamma$. The expression which results from applying these approximations to (1.10) is

$$[Prob(B^\circ \rightarrow \bar{B}^\circ)](t) = \frac{1}{2}e^{-\Gamma t}(1 - cos(\Delta m t)). \tag{1.11}$$

A particularly intuitive formulation of this expression can be made through the introduction of particle lifetime, $\tau = 1/\Gamma$ as shown:

$$[Prob(B^\circ \rightarrow \bar{B}^\circ)](t) = \frac{1}{2}e^{-\frac{t}{\tau}}\left(1 - cos\left(\frac{\Delta m}{\Gamma}\frac{t}{\tau}\right)\right). \tag{1.12}$$

This parameterization introduces the dimensionless mixing parameter $\Delta m/\Gamma$, a measure of the mixing oscillation frequency relative to the normalized neutral meson lifetime. The oscillations in the probabilities for finding the initial $|B^\circ\rangle$ state in both its original state and its mixed state are plotted for two different values of $\Delta m/\Gamma$ in the upper half of Fig. 1-1. These plots clearly illustrate the oscillatory behavior introduced via the mixing mechanism, the frequency of which is directly dependent on the size of the fundamental parameter $\Delta m/\Gamma$.

In principal, direct measurements of oscillation frequency can be made with detectors which utilize high precision silicon vertex detectors capable of measuring the decay length of the b meson. The general procedure for attempting such a measurement is to attempt the partial reconstruction of specific decay channels of the neutral b meson. This reconstruction provides information regarding the state of the neutral b meson at the time of its decay in addition to information regarding the decay length l and the Lorentz boost $\beta\gamma$ of the meson which are both necessary to reconstruct its proper decay time $t_{decay} = l/\beta\gamma c$. In addition, the intial state of the $B^\circ - \bar{B}^\circ$ pair must be identified which is most often accomplished using a tag from the semileptonic decay of the opposite b hadron. Once these event characteristics are determined, the oscillation frequency can be directly extracted

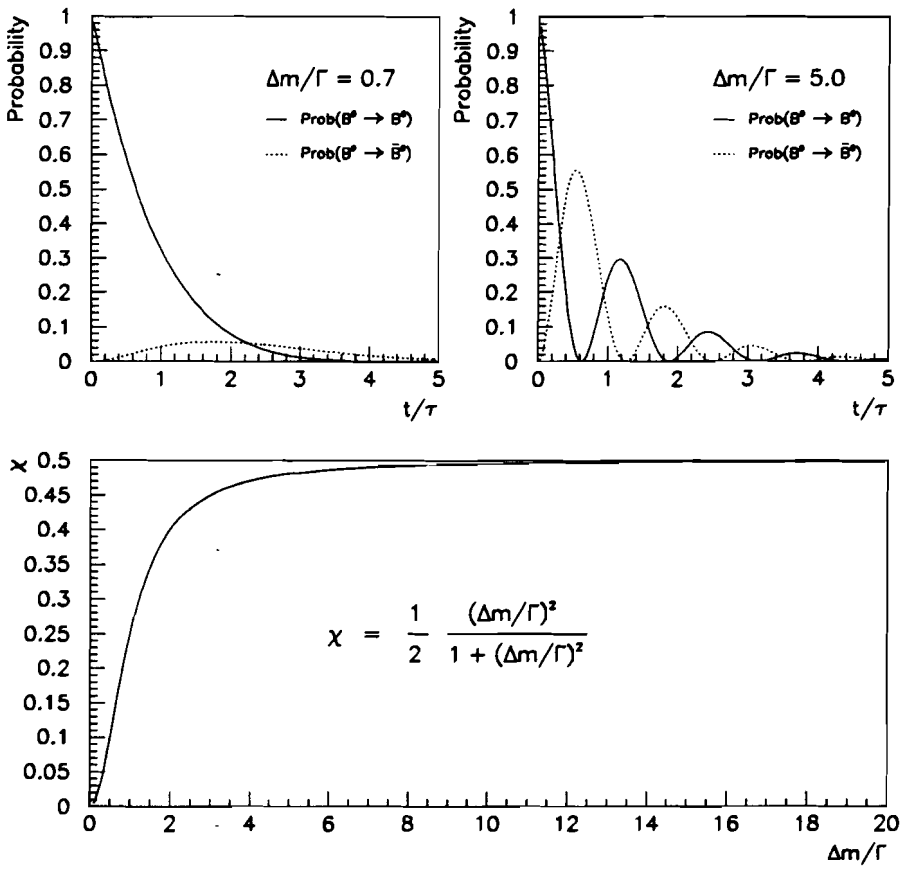

Figure 1-1: Time evolution of probability functions for $B^\circ \rightarrow B^\circ$ [solid line] and $B^\circ \rightarrow \bar{B}^\circ$ [dotted line] for different values of $\Delta m/\Gamma$ (top half). Time integrated mixing probability χ as a function of $\Delta m/\Gamma$ (bottom half).

from the observed time dependent fraction of decays which occur from the mixed state. The main limitation for this type of measurement is in the obtainable resolution for the proper decay time. As shown in Fig. 1-1, larger values of $\Delta m/\Gamma$ produce rapid oscillations in the mixing probabilities which are not possible to resolve using present detector configurations.

Alternative methods are also available for measuring the mixing parameter in cases where information regarding the decay length of the neutral b meson is not available. Integration of the expression for the $Prob(B^\circ \rightarrow \bar{B}^\circ)$ found in (1.12) over all time gives an expression for the time independent mixing probability χ which is defined as the total probability that a $|B^\circ\rangle$ will decay as a $|\bar{B}^\circ\rangle$. The result of this integration as of function of the fundamental mixing parameter $\Delta m/\Gamma$ is

$$\chi = \frac{1}{2}\left(\frac{(\frac{\Delta m}{\Gamma})^2}{1+(\frac{\Delta m}{\Gamma})^2}\right). \tag{1.13}$$

The value of χ is constrained to lie in the region between 0.0 and 0.5 with the later value corresponding to maximal mixing. The lower half of Fig. 1-1 shows the relationship between χ and $\Delta m/\Gamma$. The value for χ saturates near its maximal value for large values of $\Delta m/\Gamma$, indicative of the loss in resolving power which is inherent to faster oscillations.

An intuitive approach for understanding this loss in resolution is to note that when $\Delta m/\Gamma$ becomes large enough so that several probability oscillations take place within the typical decay time of the neutral meson, knowledge of the initial meson state becomes more uncertain. Counting experiments are often utilized to measure the time independent mixing probability. For example, one can look at events where each of the quarks in a $b\bar{b}$ pair decays semileptonically. Since the semileptonic decay of b-quarks and $\bar{b}$-quarks produce oppositely charged leptons, time averaged mixing can be determined from the ratio of like sign to unlike sign lepton pairs found in an event sample. The main drawback to this type of analysis

is that all other backgrounds to dilepton production have to be well modeled in order to extract the subset of events in the sample which result from the direct semileptonic decay of $b\bar{b}$ pairs.

1.3 Standard Model Constraints

The Standard Model mechanisms for mixing are second order weak interactions. The box diagrams for these processes are illustrated in Fig. 1-2. The dominant contribution to mixing between neutral b mesons is due to the exchange of a top quark, and the expression for the Standard Model prediction of the mass difference between weak eigenstates which is calculated from the corresponding diagram is

$$\Delta m_q = \left| \left(\frac{G_F^2}{6\pi^2} \right) B f_B^2 m_B m_t^2 \eta_{QCD} f \left(\frac{m_t^2}{m_W^2} \right) (V_{tb}^* V_{tq})^2 \right|. \tag{1.14}$$

The variables in (1.14) are the Fermi coupling constant G_F, the bag parameter B, the b meson decay constant f_B, the W mass m_W, the b meson mass m_B, the top quark mass m_t, a QCD radiative correction η_{QCD}, and the Cabibbo-Kobayahi-Maskawa (CKM) matrix elements V_{tb} and V_{tq}. The values for the bag parameter and b meson decay constant must be calculated theoretically. Although a considerable spread in results exist, the most recent calculations of $f_b\sqrt{B}$ for B_d^o suggest large values around 200-240 MeV [10]. The function $f(x)$ which describes the top quark mass dependence in (1.14) is

$$f(x) = \frac{1}{4} + \frac{9}{4(1-x)} - \frac{3}{2}\frac{1}{(1-x)^2} - \frac{3}{2}\frac{x^2 ln(x)}{(1-x)}. \tag{1.15}$$

The q notation in (1.14) is used to distinguish between the two flavors of neutral mesons (B_d^o, B_s^o) found in the b-quark system. In principal, a measurement of Δm_q can be used to extract a value for the respective CKM matrix element V_{tq} ($q = d, s$). Due to the large uncertainties associated with the mass of the top quark

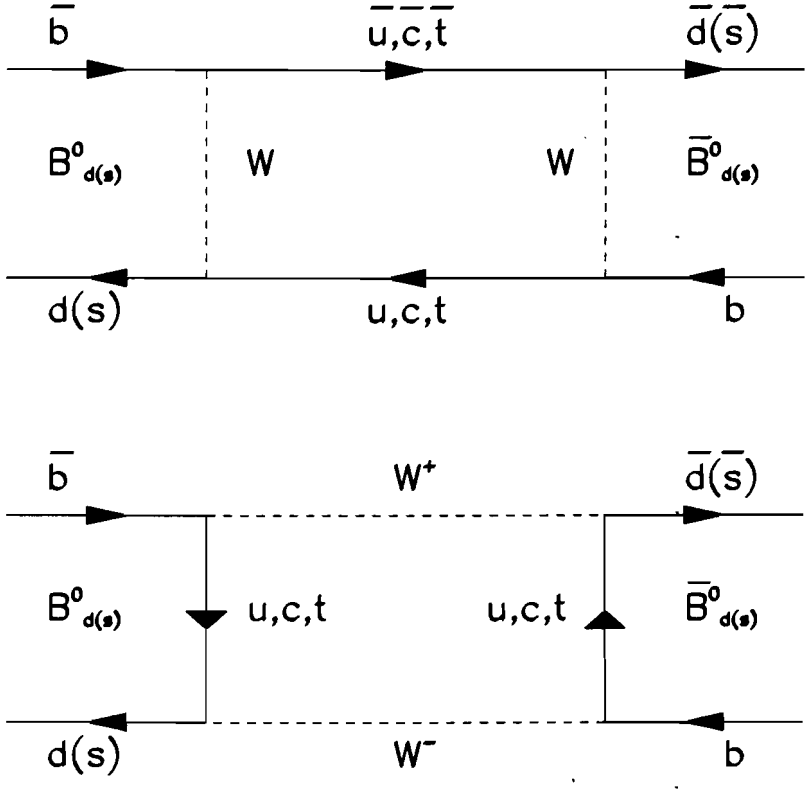

Figure 1-2: Feynman diagrams for $B^\circ - \bar{B}^\circ$ mixing.

and the theoretical calculation of Bf_B, the resulting errors on the extraction of the individual CKM matrix elements from measurements of the mass difference between weak eigenstates are large. On the other hand, if measurements of both Δm_d and Δm_s are utilized, a more precise determination of the ratio between V_{td} and V_{ts} can be made using

$$\frac{\Delta m_d}{\Delta m_s} = \frac{f_{B_d}^2 B_{B_d} m_{B_d} \eta_{QCD_d}}{f_{B_s}^2 B_{B_s} m_{B_s} \eta_{QCD_s}} \left|\frac{V_{td}}{V_{ts}}\right|^2 . \tag{1.16}$$

The ratio of $Bf_B^2 m_B \eta_{QCD}$ for the two different neutral b meson flavors is expected to be close to one. Therefore, the ratio of V_{td}/V_{ts} can be related to the ratio of the weak eigenstate mass differences with much greater precision.

It is also possible to use (1.16) to extract estimates for the mixing parameters using values of the CKM matrix elements determined from independent experimental measurements. The requirement of unitarity on the CKM matrix reduces the number of independent variables which can be used to describe the matrix elements from eighteen to nine. This number is further restricted by the requirement that a phase change for each of the six quark wave functions should not have an effect on the physics described by the matrix. However, since an overall phase change should similarly have no physical effect, the actual number of independent variables which are needed to describe the elements of the CKM matrix is 18 - 9 - (6 - 1) = 4. In the context of mixing a particularly useful representation of the CKM matrix is the Wolfenstein parameterization [11] as shown.

$$\begin{pmatrix} V_{ud} & V_{us} & V_{ub} \\ V_{cd} & V_{cs} & V_{cb} \\ V_{td} & V_{ts} & V_{tb} \end{pmatrix} = \begin{pmatrix} 1-.5\lambda^2 & \lambda & A\lambda^3(\rho - i\eta) \\ -\lambda & 1-.5\lambda^2 & A\lambda^2 \\ A\lambda^3(1-\rho-i\eta) & -A\lambda^2 & 1 \end{pmatrix} \tag{1.17}$$

The present experimental values for the parameters utilized in the Wolfenstein parameterization are $\lambda = 0.2205 \pm .0018$, $A = 0.90 \pm 0.12$, and $\sqrt{\rho^2+\eta^2} = 0.39 \pm 0.07$ [12]. One constraint placed on the elements of the CKM matrix from the

requirement of unitarity can be expressed as

$$V_{ud}V_{ub}^{*} + V_{cd}V_{cb}^{*} + V_{td}V_{tb}^{*} = 1. \tag{1.18}$$

The form of the unitarity condition in (1.18) can be modified through substitution of the matrix elements in (1.17) and further mathematical manipulation to give

$$\frac{V_{ub}^{*}}{\lambda V_{cb}} + \frac{V_{td}}{\lambda V_{cb}} = 1. \tag{1.19}$$

This formulation defines a triangle in the η-ρ plane as illustrated in Fig. 1-3. The top corner of the triangle is constrained to lie in the semicircular region constructed from the experimental restriction on $\sqrt{\rho^2 + \eta^2}$. The side of the triangle given by $V_{td}/\lambda V_{cb}$ is therefore restricted in magnitude to the condition where the top corner of the triangle lies at the far left edge of the semicircle along the ρ axis. This condition along with experimental measurements of λ and the Wolfenstein stipulation that $V_{cb} = -V_{ts}$ places an upper limit on the magnitude of V_{td}/V_{ts} of 0.335 and a corresponding lower limit on $\Delta m_s/\Delta m_d$ of 9.0 from (1.16). Recent measurements of χ_d which are discussed further in Section 1.4.1 suggest a value for $\Delta m_d/\Gamma$ on the order of 0.7. Therefore, the resulting Standard Model lower limit on the value of $\Delta m_s/\Gamma$ is roughly 5.5 with the most likely values being in the range between 8-24 [12]. The prediction of large values for $\Delta m_s/\Gamma$ means that mixing in the $B_s^{\circ} - \bar{B}_s^{\circ}$ system will most likely occur in a frequency range which is very difficult to measure experimentally.

1.4 Previous Experimental Results for χ

In the past several years, a large number of experiments have produced measurements of the time integrated mixing probability χ for the $B^{\circ} - \bar{B}^{\circ}$ system. These

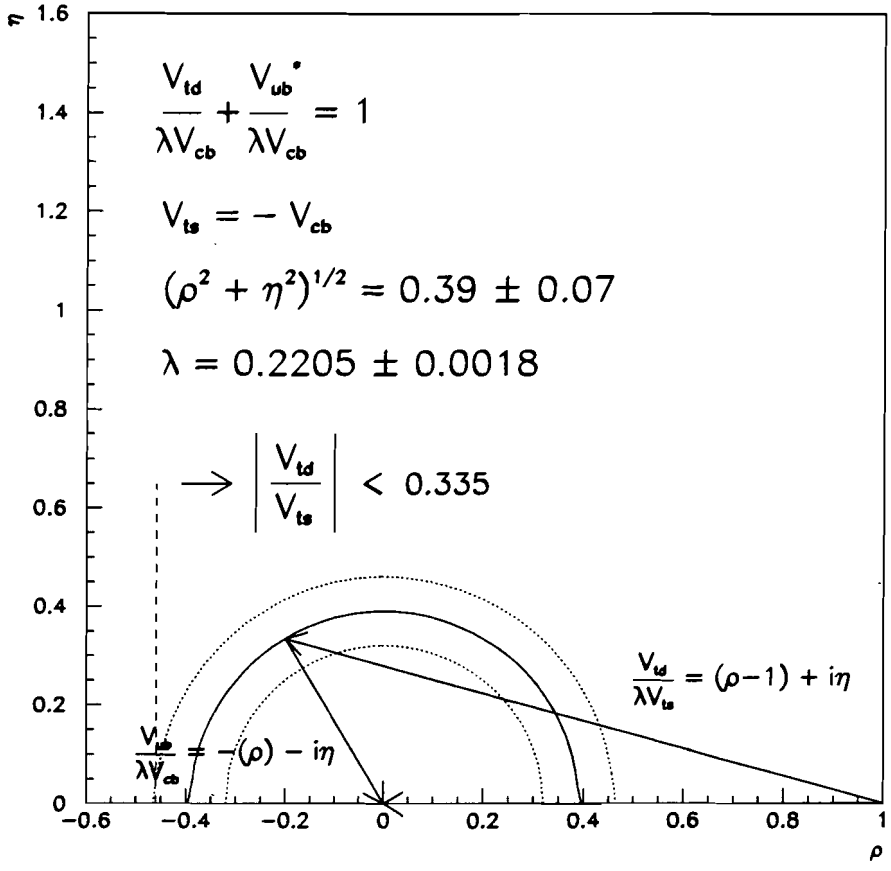

Figure 1-3: Triangle condition implied from unitarity in the ρ-η plane. The semi-circular region represents the experimental restriction on $(\rho^2 + \eta^2)^{\frac{1}{2}}$.

measurements can be grouped into two separate categories. One group of measurements are performed at e^+e^- colliders which operate at the $\Upsilon(4s)$ resonance. Since the threshold for producing $B_s^\circ - \bar{B}_s^\circ$ pairs lies above the $\Upsilon(4s)$ resonance, measurements of the time integrated mixing probability at these colliders provide a direct result for χ_d. Measurements of χ performed at higher energy colliders such as LEP and the Fermilab Tevatron, on the other hand, furnish a mixing probability representative of both χ_d and χ_s since the hadronization of $b\bar{b}$ quark pairs at these colliders results in the production of both neutral meson flavors. A more detailed description of each type of measurement is provided in the following sections.

1.4.1 Measurements of χ_d on the $\Upsilon(4s)$

The $\Upsilon(4s)$ resonance is constrained to decay in pairs of b mesons limited to B^+B^- and $B_d^\circ\bar{B}_d^\circ$. The wavefunctions of the two b mesons are required to have a fixed phase relationship which means that if the first meson is seen to decay in a particular flavor state, the second meson will necessarily be found in the opposite flavor state at the time of the decay. However, the second meson will continue to undergo mixing oscillations until it decays at some later time which results in a finite probability for observing the two mesons in identical flavor states at the time of their respective decays. The probability for observing both decays in the B_d° state at times t_1 and t_2 is

$$P(B_d^\circ, B_d^\circ, t_1, t_2) = \frac{1}{2} exp\left(-\Gamma(t_1 + t_2)\right)\left[1 - cos\left(\Delta m_d(t_2 - t_1)\right)\right]. \qquad (1.20)$$

This expression can be integrated over all times t_1 and t_2 to give a time independent formulation of the total probability for observing the decay of both neutral mesons in the same flavor state. The expression for the time averaged mixing probability χ_d constructed from the time integrated probabilities for observing the

decays of neutral b meson pairs in like and unlike flavor states is

$$\chi_d = \frac{N(B_d^\circ B_d^\circ) + N(\bar{B}_d^\circ \bar{B}_d^\circ)}{N(B_d^\circ B_d^\circ) + N(\bar{B}_d^\circ \bar{B}_d^\circ) + N(B_d^\circ \bar{B}_d^\circ)}. \tag{1.21}$$

In general, the flavor state of the b meson is determined via the lepton charge from the associated semileptonic decay channel. Due to the fact that the production of charged b meson pairs can also result in dilepton events, the expression for χ_d in terms of the raw number of observed like and unlike sign dilepton pairs includes an additional correction term Λ which can be simply expressed as the fraction of observed dilepton pairs resulting from the decay of a charged meson pair to the total number of observed dilepton pairs. The resulting formulation for χ_d is

$$\chi_d = \left(\frac{1}{1-\Lambda}\right) \frac{N(\ell^-\ell^-) + N(\ell^+\ell^+)}{N(\ell^-\ell^-) + N(\ell^+\ell^+) + N(\ell^+\ell^-)}. \tag{1.22}$$

The value for Λ is known to be on the order of 0.5, but the experimental uncertainty associated with this parameter turns out to provide the single largest contribution to the systematic error in measurements of χ_d from lepton counting experiments. Several measurements have attempted to overcome this uncertainty through the partial reconstruction of specific decay channels associated with the decay of neutral b mesons. For example, the reconstruction of a D^* through the decay channel $D^{*-} \rightarrow \bar{D}^\circ \pi^-$ along with the identification of a properly signed lepton can explicitly identify the decay of a neutral b meson in the channel $B^\circ \rightarrow D^{*-}\ell^+\nu$. The increased sensitivity of this type of measurement due to the lack of dependence on Λ is somewhat offset due to the drop in statistics which results from the use of specific decay channels and experimental limits on reconstruction efficiency. The most recent experimental results for χ_d [13][14][15] are shown in Fig. 1-4.

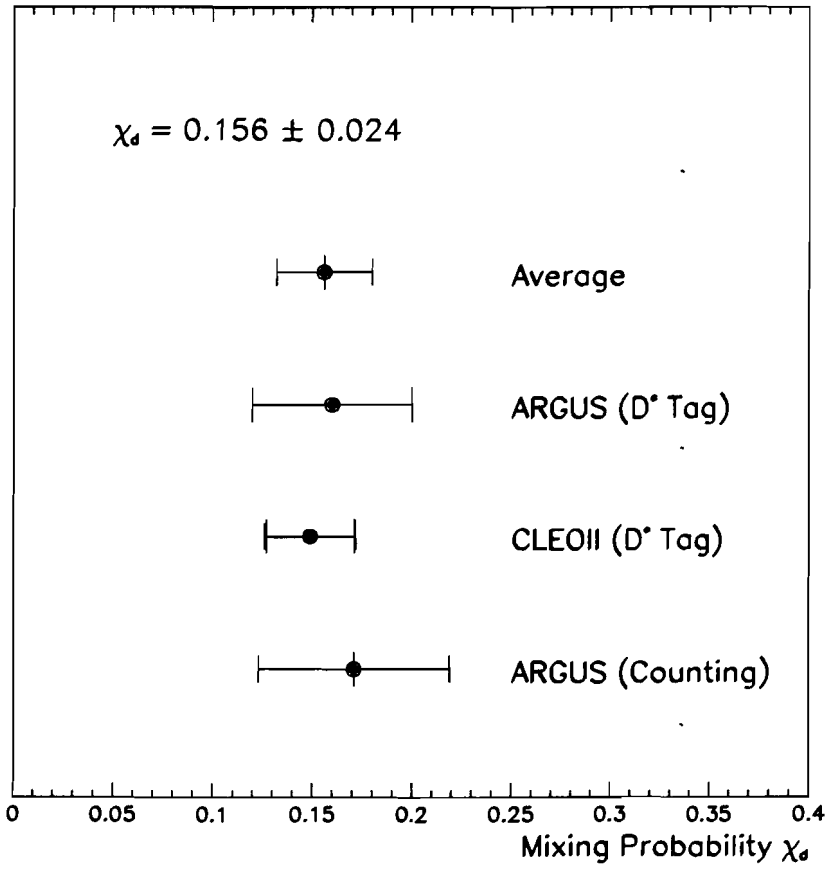

Figure 1-4: Recent experimental measurements of the B_d^0 mixing probability χ_d.

1.4.2 Measurements of χ at high energy colliders

Production of $b\bar{b}$ quark pairs above the b-production threshold is accomplished at LEP and the Fermilab Tevatron through Z° decays and $p\bar{p}$ collisions respectively. The hadronization of these quark pairs results in the production of all varieties of b hadrons including B_d°, B_s°, B^-, and Λ_b plus antiparticles where Λ_b is meant to represent potential b-baryon states. The flavor of each hadron is tagged using either the lepton charge from the associated semileptonic decay channel or in some cases from a jet charge variable which is generally defined as a weighted average over all charged particles within a jet opposite to a single observed tag from a semileptonic decay channel. Since semileptonic decays from all of the hadron states are possible, the mixing probability which one measures at these colliders is an average defined as

$$\chi = \frac{f_d\chi_d + f_s\chi_s}{f_d + f_s + f_u + f_\Lambda}. \tag{1.23}$$

In the above expression the f_i represent a product of the production rate for the given hadron state with the respective semileptonic branching ratio. The f_i variables are often defined to be normalized with respect to each other in which case the denominator of (1.23) simply reduces to one. Since the hadronization of the b and $\bar{b}$ are uncorrelated with respect to each other, the value for χ in terms of the number of observed like and unlike sign lepton pairs is

$$2\chi(1-\chi) = \frac{N(\ell^-\ell^-) + N(\ell^+\ell^+)}{N(\ell^-\ell^-) + N(\ell^+\ell^+) + N(\ell^+\ell^-)}. \tag{1.24}$$

This formulation assumes, however, that both leptons are produced from the direct semileptonic decay of the b hadrons. In practice, a careful accounting of the different fractions of lepton pairs where one or both leptons originates from other background production processes must be done in order to properly extract a result for χ. Cascade decays of the type $b \to c \to \ell$ are particularly troublesome since the

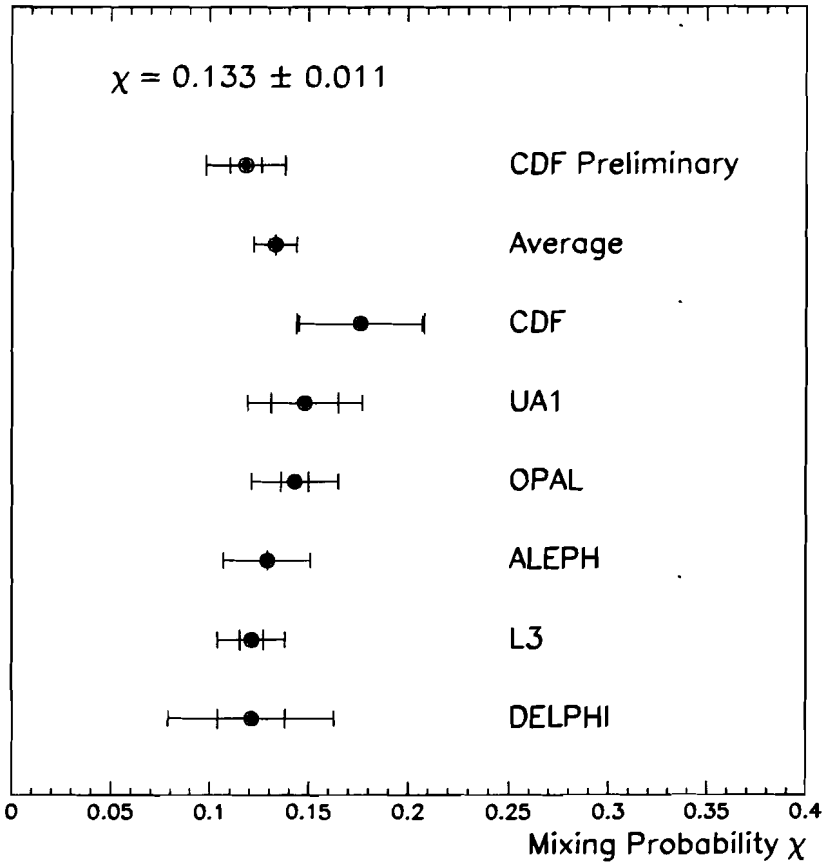

Figure 1-5: Recent experimental measurements of the flavor averaged mixing probability χ.

lepton charge produced in this type of decay is directly opposite to that produced in the direct semileptonic decay of the same b-quark. Therefore, an event in which one lepton is produced through the direct semileptonic decay of one b hadron while another is obtained from a cascade decay from the opposite b hadron will mimic the mixing process via the production of a like sign dilepton event. Recent experimental measurements of the mixing probability χ [16][17][18][19][20][21][22] are summarized in Fig. 1-5. The results obtained at different colliders are not directly comparable since the values for f_d and f_s are dependent on the hadronization of the produced $b\bar{b}$ pairs. However, these differences are thought to be small in comparison to the present scale of the errors associated with these measurements.

The method used to extract a value of χ_s from a measured value of χ is illustrated in Fig. 1-6. In this illustration the preliminary CDF result for χ from the 1992-93 collider run at Fermilab is used in conjunction with the world average for χ_d to produce a constraint on the value for χ_s. In order to extract this constraint from (1.23), a theoretical estimate for the normalized parameters f_d and f_s is utilized [17]. This estimate is partially based on measurements of $N(K^+)/N(\pi^+)$ obtained from the ISR pp collider at center of mass energies of 45 and 63 GeV [23]. These measurements were made based on the highest energy kaons and pions within the event sample which in most cases originated directly from scattered quarks within the proton. Therefore, the average z value associated with the fragmentation that produced these mesons was generally high, a situation comparable to that for b-quark which also tends to have a very hard fragmentation. The measured value of $N(K^+)/N(\pi^+)$ needs to be corrected for pions coming from K^* decays after which a value of 0.55 ± 0.05 can be extracted for f_s/f_d. The differences in the semileptonic branching ratios for the different b-hadrons are assumed to be negligible which along with the allowance for a 10% hadronization fraction into b baryon states leads to the result that $f_u : f_d : f_s = 0.375 : 0.375 : 0.15$.

The dotted lines in Fig. 1-6 represent the experimental limits on χ_d, while the dashed lines represent experimental constraints imposed from the measurement of χ based on the values for f_d and f_s given above. As discussed in Section 1.3 a Standard Model constraint can be placed on the relationship between Δm_d and Δm_s using experimental measurements of the CKM matrix elements. The corresponding constraint on the relationship between χ_d and χ_s is illustrated with the hatched region in Fig. 1-6. The hatched region is that which is allowed in the Standard Model based on experimental measurements of the CKM matrix elements. The present mixing results are consistent with large values of χ_s up to the maximal value of 0.5 and are therefore suggestive of high frequency oscillations in the $B_s^\circ - \bar{B}_s^\circ$ system.

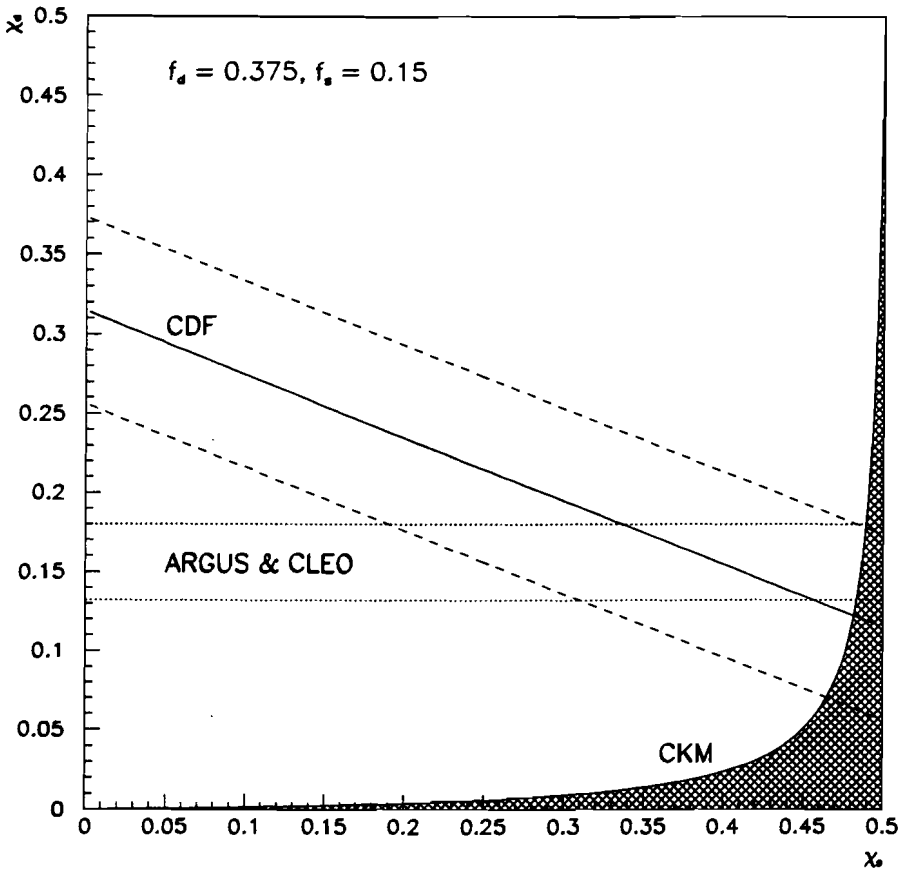

Figure 1-6: Experimental constraints on mixing probability χ_s using recent measurements of χ_d and χ. The hatched region is that is allowed from Standard Model constraints.

Chapter 2

DØ Detector

The primary focus of the DØ detector is the study of high mass states and large P_T phenomena which are produced in $p\bar{p}$ collisions at $\sqrt{s} = 1.8$ TeV. In particular, the physics objectives of searching for the top quark and making precision measurements of W and Z bosons were predominant influences on detector design. The design goals for the detector were superior identification of electrons and muons, good measurement of parton jets through highly segmented calorimetry with good energy resolution, and well controlled measurement of missing E_T. In order to meet these goals, it was decided not to include a central magnetic field within the central tracking region of the detector. A calorimetric measurement of particle energies is advantageous in that neutral and charged hadrons are treated on an equal footing, and the reduced size of a non-magnetic tracking system provides an opportunity for enhanced calorimetry and muon detection.

The DØ detector is divided into three main subsystems which in general operate independently from one another. Fig. 2-1 shows a cutaway view of the different detector subsystems. The non-magnetic inner tracking region occupies the area immediately adjacent to the accelerator beam pipe. The tracking elements are surrounded both radially and at the ends by components of the DØ liquid argon calorimeter which are designed to provide complete calorimetric coverage of the solid angle surrounding the collision point. The muon subsystem consists of three

layers of proportional drift chambers which enclose the calorimeter elements and provide substantial muon coverage of the solid angle. In order to make a momentum determination of muon tracks, a magnetized iron toroid is positioned between the inner and central layers of muon chambers. An analysis of the bend of a muon track in the magnetic field of the iron toroid results in sign and momentum determination. A brief description of the Fermilab Tevatron collider and each of the detector subsystem is provided in the subsequent sections. In addition, a more detailed description of the entire detector can be found in [24].

2.1 Fermilab Tevatron $p\bar{p}$ Collider

The Fermilab Tevatron is currently the highest energy particle accelerator in the world. The accelerator mode which was utilized in the 1992-93 collider run produced $p\bar{p}$ collisions at a center of mass energy of $\sqrt{s} = 1.8$ TeV in two luminous regions of the accelerator as illustrated in Fig. 2-2. A peak instantaneous luminosity of $\sim 1 \times 10^{31}$ s^{-1} cm^{-2} was obtained during this period which was a factor of two above what was anticipated at the beginning of the run.

The Fermilab collider actually consists of seven independent particle accelerators [25]. Protons originate as hydrogen ions which are accelerated to 750 KeV in the electrostatic field of the Cockroft-Walton preaccelerator. The ions are then accelerated to 200 MeV in the Linac linear accelerator and subsequently passed through a carbon foil which strips off any remaining electrons. The resulting proton beam is passed into the Booster synchrotron which ramps the protons to 8 GeV prior to their injection into the main ring. The main ring accelerator has a circumference of 3.7 miles and consists of a string of 774 dipole and 240 quadrupole magnets in conjunction with 18 dual RF cavities. Once inside the main ring the protons are focused into six high density bunches and accelerated to 120 GeV.

During the periods when collisions are taking place in the Tevatron, accelerated

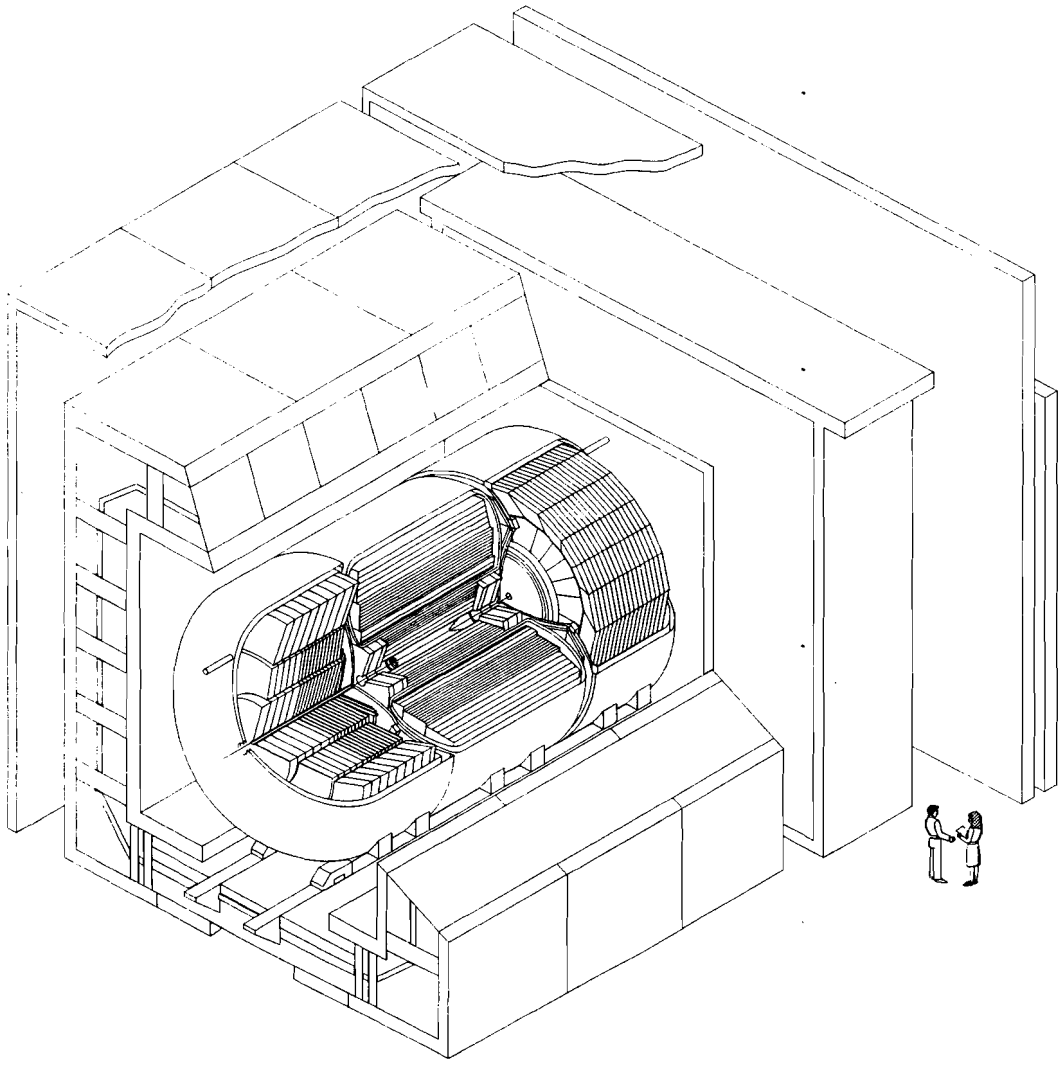

Figure 2-1: Cutaway view of the DØ detector showing all three major detector subsystems (Central Tracking, Liquid Argon Calorimeter, and Muon Detector).

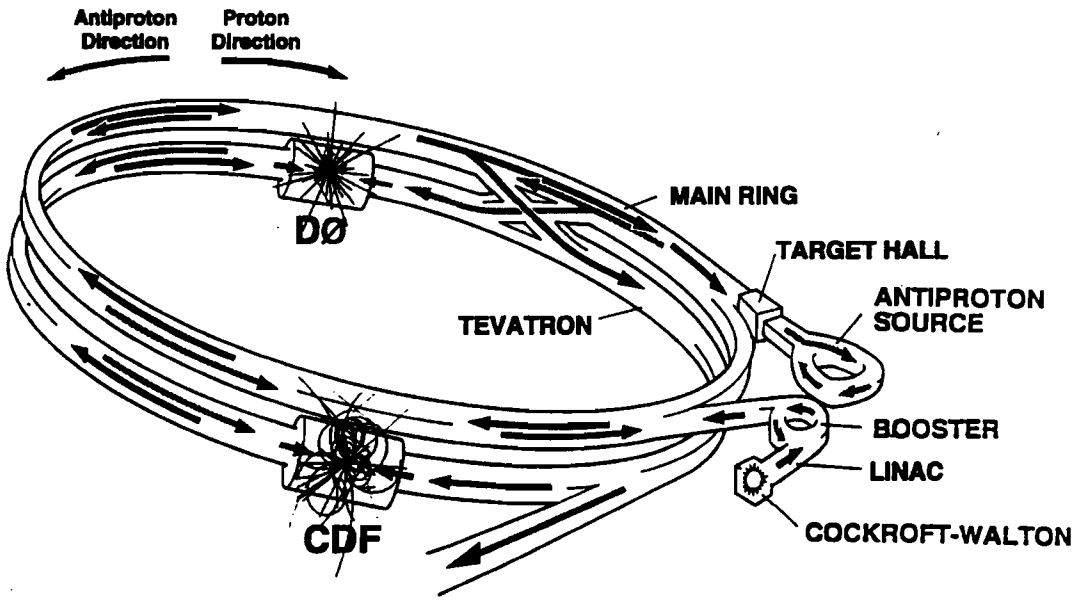

Figure 2-2: Illustration of the Fermilab Tevatron $p\bar{p}$ collider showing the DØ and CDF interaction regions and the various lower energy accelerators.

proton bunches in the main ring are used to produce antiprotons for subsequent collider runs. The protons are directed into a nickel target which yields about 10^7 antiprotons per 10^{12} incident protons. A dipole magnet selects antiprotons in the energy range around 8 GeV and passes them in to the Debuncher ring which further reduces the momentum spread and transverse beam profile of the captured antiprotons using a process known as stochastic cooling. Upon reduction of the their phase space, the antiprotons are transferred into the Accumulator where they are adiabatically decelerated by 150 MeV into a stable orbit referred to as a "stack core". The momentum spread and transverse beam profile of the antiprotons stored in the accumulator is continually controlled using stochastic cooling systems. During the 2.4 s antiproton production cycle there are periods of considerable beam losses in the main ring. Since the main ring passes directly through the upper half of the detector, these losses significantly effect data collection at DØ. These effects

will be discussed in greater detail in Section 3.1.3.

When required for $p\bar{p}$ collisions, antiprotons are transferred from the Accumulator into the main ring where their energy is ramped to 150 GeV prior to their injection into the Tevatron. The Tevatron utilizes superconducting magnets maintained at a temperature of 4.6 K to accelerate protons and antiprotons to an energy of 900 GeV. At the start of each collider run six proton and six antiproton bunches are injected into six of the 1113 RF buckets around the ring at intervals which are roughly equidistant with respect to each other. Once all of the bunches are present the Tevatron is ramped to its full energy at which point the counter-circulating bunches begin to pass through each other approximately every 3.5 μs. Once the beams have been stabilized, the luminosity in the interaction regions of the accelerator is greatly increased using a pair of superconducting low-beta quadrupole magnetics situated at both ends of the DØ and CDF detectors. These magnets focus the beams as they enter the interaction regions to a transverse width of $\sigma_{x,y}$ ~ 40 μm which results in a longitudinal interaction region along the incident beam direction with a width of $\sigma_z = 30$ cm.

2.2 Central Tracking

The DØ detector utilizes a non-magnetic tracking system which fits into the volume bounded by a radial distance of 78 cm in the direction perpendicular to the beam pipe and a longitudinal distance of $\pm$ 135 cm in either direction along the beam pipe from the central interaction point. The major design goals of the system are the measurement of the position of the interaction vertex and the suppression of backgrounds to electron candidates in the calorimeter. One source of background to prompt electrons comes from photon conversions into electron pairs within the tracking volume. In order to reduce this background as much as possible, the lowest possible density materials are used in the construction of the tracking elements to

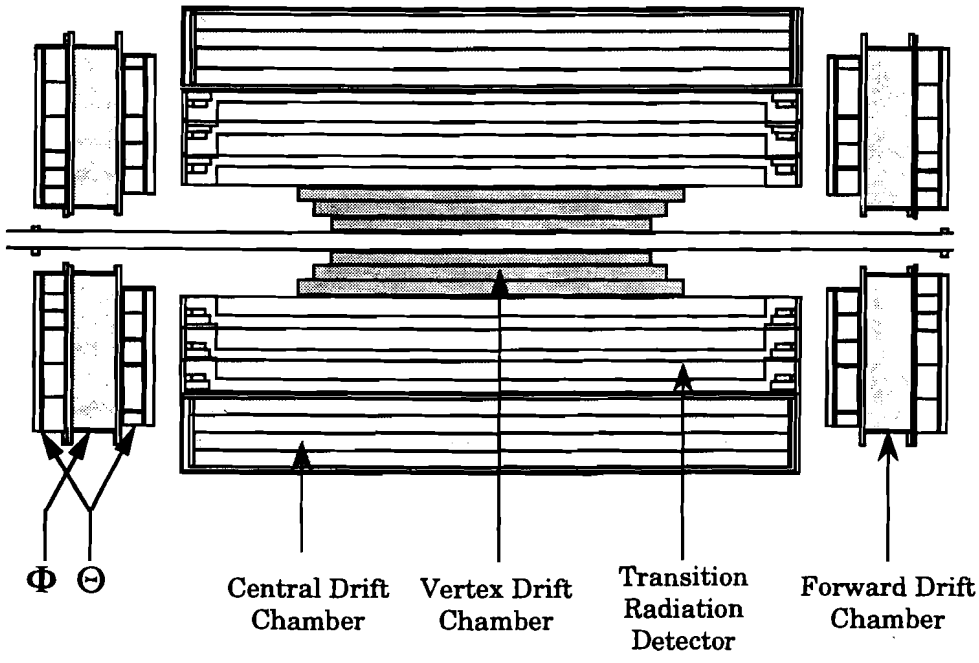

Figure 2-3: Layout of DØ central tracking system.

reduce the number of radiation lengths through which a particle must pass to reach the calorimeter. The central tracking system is divided into four separate detectors as shown in Fig. 2-3. The innermost detector is known as the vertex tracking chamber (VTX) and is primarily used to identify the position of an event vertex. The transition radiation detector (TRD) which is designed to help discriminate electrons from hadrons as described below occupies the space between the VTX and the outer tracking chambers. The outer drift chambers are located in both the central (CDC) and forward (FDC) regions of the central tracking volume. A more detailed description of each of these tracking elements is given below.

2.2.1 Vertex Tracking Chamber

The VTX occupies the radial space perpendicular to the beam pipe between 3.7 and 16.2 cm. The primary purpose of the VTX is the determination of the position of an event vertex or event vertices in the case of multiple interactions. In addition, tracking information from the VTX aids in the identification of photons which convert into electron pairs in the TRD and provide a fake prompt electron signal in the calorimeter. The VTX is divided into three concentric layers of cells. There are 16 cells surrounding the beampipe on the innermost layer and 32 cells in the outer two layers. Each cell contains eight sense wires strung parallel to the incident beam direction with readout of each wire provided for at both ends of the chamber to provide hit information along the wire direction. Sense wires within a cell are staggered by $\pm$ 100 μm to resolve left-right ambiguities and the cells on the three layers are also offset to further aid in track reconstruction. The coarse electric field in the drift cells is provided by aluminum traces which are etched on the carbon fiber support tubes which form the cells. Shaping wires within the cells are used to fabricate the fine details of the electric field. Fig. 2-4 shows the arrangement of wires within the cells of the VTX. The VTX utilizes a slow gas ($CO_2/C_2\ H_6$) in order to maximize the drift time resolution of the chamber. The operating parameters of the chamber produce an average electric field of 1 kV/cm and an average drift velocity of 7.3 μm/ns. The performance of the VTX has been measured using both test beam and collider data. The measured hit resolution in the radial direction is 35-65 μm depending on the drift distance associated with the hit. This leads to a two track resolving distance of 630 μm with 90% efficiency. The hit resolution in the direction along the beam direction has been measured to be approximately 1% of t he sense wire length which turns out to be about 1 cm.

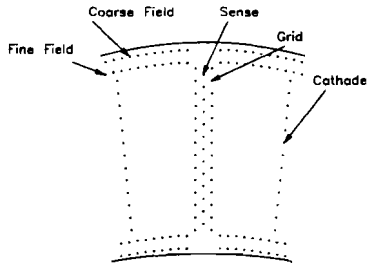

Figure 2-4: End view of VTX showing layout of the field, sense, and grid wires.

2.2.2 Transition Radiation Detector

The TRD is used to provide independent identification of electron candidates which are found in the calorimeter. When a particle passes from a medium with a low dielectric constant to a medium with a high dielectric constant it emits high energy radiation in the form of x-rays. The total energy which is emitted during the transition between mediums is proportional to $\gamma = p/m$. Since the electron mass is much lower than that of a hadronic particle, an electron will emit a significantly greater amount of transition radiation than a hadronic particle with a similar momentum. Therefore, a measurement of the transition radiation associated with an electron candidate in the calorimeter can provide an independent confirmation of the particle identification.

In practice the radiator section of a TRD must consist of a large series of dielectric transitions in order to produce a large enough sample of x-ray energy to be measured in the detection elements of the device. The DØ transition radiation detector consists of three sequential radial units each of which contains a series

of radiators followed with a proportional wire chamber to measure the resulting transition radiation. The radiator section of the detector is constructed from 393 polypropylene sheets with a thickness of 18 μm in nitrogen gas. The separation between the individual sheets is on the order of 150 μm. This arrangement produces an x-ray spectrum which peaks at 8 KeV and is contained almost entirely below 30 KeV. A plane of ground wires separates the gas volume in the detection unit into a drift region and a cylindrical proportional wire chamber at a larger radius. X-ray conversions which occur over the first several millimeters of the drift region produce charge clusters which are then detected at the far end of the detection unit where 256 sense wires are strung parallel to the beam direction.

Both the magnitude and the arrival time of the charge at the signal wires are used to help distinguish electrons from hadrons. The charge arrival time is important because ionization along the particle track will tend to arrive at the signal wires in the chamber earlier than the energy associated with the x-ray conversions in the most forward part of the drift region. A factor of rejection of ten for hadrons can be obtained using only the information regarding the total collected charge in the TRD while maintaining a 90% efficiency for electrons. If the information regarding the number of charge clusters measured and their relative positions in time are also included in the analysis, the rejection factor for hadrons can be increased to 50. The total number of radiation lengths in the TRD as seen by a particle with a perpendicular trajectory to the beam pipe is a minimal .036 which helps prevent photon conversions in this region.

2.2.3 Central Drift Chamber

The DØ central tracking chamber occupies the radial distance between 49.5 and 74.5 cm in the direction perpendicular to the beam pipe and has a total length of 184 cm parallel to the beam direction. The purpose of this particular chamber is

the tracking of charged particles in the region where $|\eta| < 1.0$.

The CDC consists of four rings each containing 32 azimuthal drift cells. Each cell has seven sense wires strung parallel to the incident beam direction with one end readout in addition to two delay lines embedded in the inner and outer cell support structure which propagate signals induced from the nearest neighboring anode wires. The delay lines are read out at both ends to provide a measurement of the hit position in the direction parallel to the incident beams. Adjacent sense wires in the cells are staggered by $\pm$ 200 μm in the azimuthal direction to resolve left-right ambiguity at the cell level, and the azimuthal cell position is offset between the four rings to further aid in track reconstruction.

The electric field in the drift cells is produced by pairs of potential wires strung between the sense wires, and a grounded potential wire is added to the innermost and outermost pairs to minimize the signal which is induced on the delay lines. The operating parameters of the CDC produce an average electric field of 0.620 kV/cm in the drift cells and an average drift velocity of 34 μm/ns. CDC performance has also been extensively tested using both test beam and collider data. In the radial direction the hit resolution of the chamber has been measured to be 150-200 μm depending on drift distance. A 90% efficiency for two hit resolution is obtained for 2 mm separations. The hit resolution obtained from delay line information for the direction parallel to the incident beam directions has been determined to be 4 mm. If information from each of the four rings of cells is used, this resolution can be reduced to 2 mm.

2.2.4 Forward Drift Chamber

DØ utilizes a set of forward particle tracking chambers at both ends of the central tracking volume to measure charged particle tracks at small angles (down to $\theta = 5°$) with respect to the incident beam direction. Each of the FDC elements consists of

three separate chambers. A Φ module strung with radial sense wires to measure the azimuthal coordinate of a particle track is sandwiched between two Θ modules each containing sense wires strung perpendicular to the radial direction to measure the angle of a particle track relative to the incident beam direction. The two Θ modules are rotated 45° with respect to each other to assist in track reconstruction. Each Φ module is a single drift chamber separated into 36 radial sectors over the full azimuth, while the Θ modules consist of four separate quadrants each of which contains six rectangular drift cells at increasing radii. A set of 16 signal wires is employed in each sector of the Φ module strung radially along the incident beam direction and staggered in the azimuthal direction to resolve left-right ambiguity. Each individual cell of the Θ modules contains eight signal wires. For the innermost three drift cells in each quadrant the signal wires are strung at one edge of the cell to completely remove the inherent left-right ambiguity. In the remaining cells the signal wires are staggered by $\pm$ 200 μm to account for this effect. Each cell in the Θ modules also contains one delay line of similar construction to those used in CDC to measure hit position along the wire direction. The operating parameters and performance characteristics of the FDC match closely with those already discussed for the CDC.

2.3 Calorimetry

The DØ calorimeter is assigned a substantial number of important functions within the framework of the detector design. The calorimeter is primarily responsible for making the sole energy measurement of electrons, photons, and jets. In addition, calorimeter information is used to reconstruct the missing transverse energy within events and to help in the identification of electrons, photons, and muons.

The calorimeter is separated into three individual sections which provide nearly hermetic coverage of the solid angle. The central calorimeter occupies the region

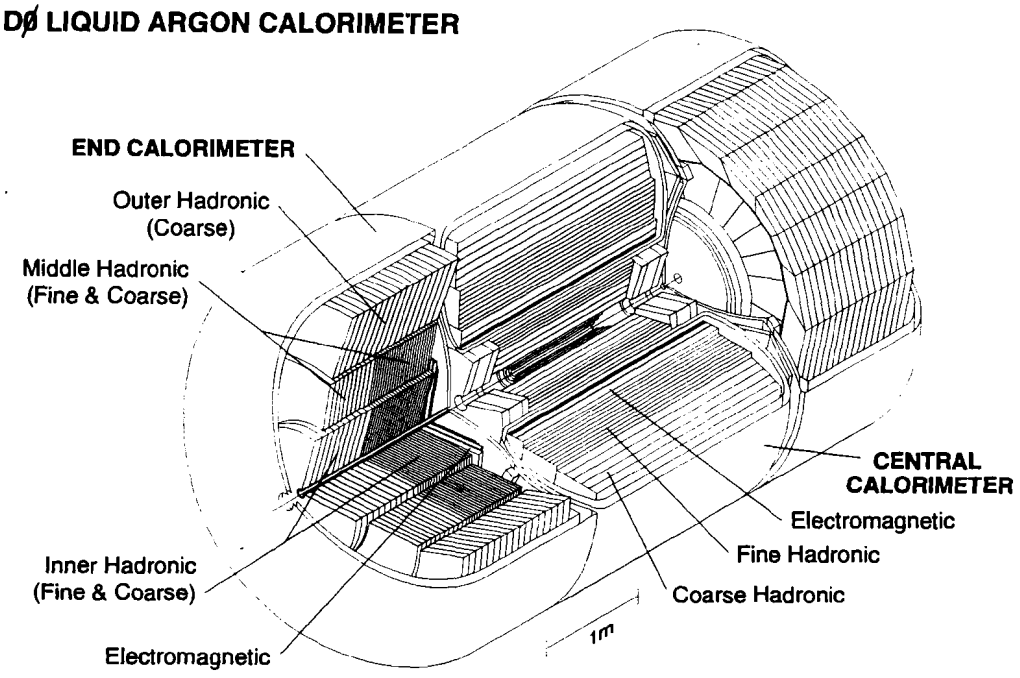

Figure 2-5: Cutaway view of the DØ calorimeter showing the separation of the central and end calorimeters in addition to the segmentation of the calorimeter into electromagnetic and hadronic sections.

directly outside the central tracking volume in the radial direction and roughly provides coverage for the region where $|\eta| < 1.0$. Calorimeter coverage is extended out to $|\eta| \sim 4.0$ without sacrificing access to the central tracking region using independent endcap calorimeter modules at both ends of the detector. This configuration is illustrated in Fig. 2-5. The boundary between the central and end calorimeter modules is chosen to be perpendicular to the incident beam direction in order to minimize degradation in the missing E_T measurement due to uninstrumented material in this region. Calorimetric measurements in the transition region are supplemented with information from scintillation counter arrays mounted on the inner walls of the endcap calorimeter modules in order to account for energy

deposition in the uninstrumented material. These scintillator arrays are referred to as the intercryostat detectors (ICD).

The DØ calorimeter is separated into three distinct layers with increasing radii each of which utilizes alternating sections of absorption material and liquid argon. The absorber material provides matter in which particle showering occurs through interactions between incident particles and the medium. The liquid argon serves as the active medium in which the resulting particle showers deposit energy via ionization. The energy deposition is proportional to the resulting charge accumulation in the active medium.

The innermost layer of the calorimeter is referred to as the electromagnetic layer. The absorption sections used in the electromagnetic layer are thin uranium sheets with a thickness of 3 mm in the central calorimeter and 4 mm in the endcap sections. The function of the electromagnetic layer is to contain and measure the particle showers of charged particles entering the calorimeter which predominantly interact electromagnetically with the absorber material. The relevant scale of electromagnetic interactions in a material is known as radiation length (X_0) and is defined to be the distance over which an energetic electron or photon will lose 63% of its incident energy through Bremsstrahlung radiation.

The electromagnetic layer of the DØ calorimeter is subdivided into four readout layers with relative spacings of 2,2,7, and 10 radiation lengths. The first two readout layers are primarily included to provide discrimination between showers resulting from photons and neutral pions which have different longitudinal shower development. The third layer contains the region of maximum electromagnetic shower deposition and is therefore segmented by a further factor of two in η-ϕ space in order to more accurately measure the location of shower centroids. The fourth layer ensures good containment of electromagnetic showers within the electromagnetic section of the calorimeter and completes the the 21 X_0 of absorber

material found in this section.

The outer two layers of the calorimeter are known as the fine hadronic and coarse hadronic sections. The dominant mechanisms for energy loss in particles which do not interact electromagnetically with the absorber material found in the calorimeter are the strong interactions between the incident particles and the atomic nuclei in the absorber material. Here the relevant interaction scale for a given material is nuclear interaction lengths (λ_I) which is a measure of the mean free path between particle collisions with absorber nuclei.

The absorber sections of the fine hadronic layer are constructed from 6 mm thick sheets of uranium and are subdivided into three 1.3 λ_I thick readout layers in the central calorimeter module and four layers of similar thickness in the end modules. The coarse hadronic layer in the central calorimeter module has one thick section of absorber material constructed from 46.5 mm thick sheets of copper. In the end modules there are three separate layers of absorber material constructed from stainless steel sheets of a similar thickness. The total thickness of the absorber found in the coarse hadronic sections is 4.0 λ_I in the central and 5.5 λ_I in the ends. The total number of nuclear interaction lengths which a particle must traverse to exit the calorimeter is 9.0 at $\eta = 0$ and increases to 12.9 at higher pseudorapidity.

The readout of the DØ calorimeter is arranged in 'pseudo-projective' towers with each tower further subdivided in depth. This term is indicative of the fact that the centers of the calorimeter cells in a particular tower lie along a line which points back to the center of the interaction region despite the fact that the cell boundaries do not lie perpendicular to these lines. This arrangement is shown in Fig. 2-6. The transverse size of the calorimeter cells was chosen to be comparable to the width of particle showers which are on the order of 1-2 cm for electromagnetic showers and 10 cm for hadronic showers. In terms of variables more directly useful for physics, the typical transverse size of the towers are $\Delta\eta \times \Delta\phi = 0.1 \times 0.1$.

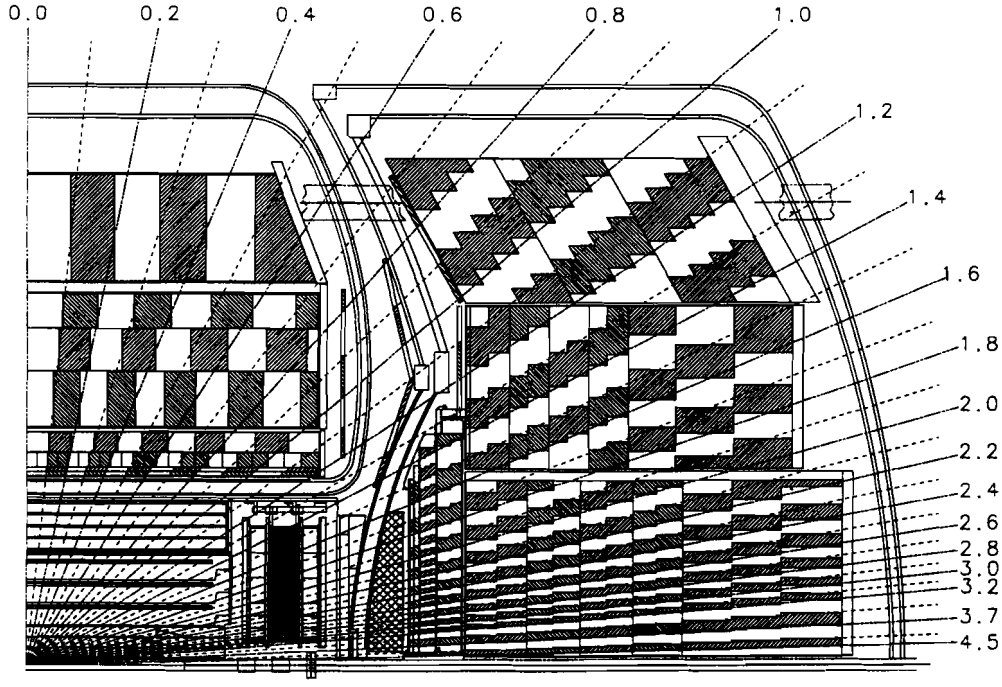

Figure 2-6: Cutaway view of the DØ central and end calorimeters showing the intercryostat detectors and massless gaps located between the central and endcap modules.

This segmentation represents a scale which is smaller than that of a typical parton jet where $\Delta R = \sqrt{\Delta\eta^2 + \Delta\phi^2} \sim 0.5$ and is therefore useful for probing the shape of jets. As previously mentioned the third readout layer of the electromagnetic section of the calorimeter has finer segmentation in $\eta - \phi$ space to isolate shower centers. In this particular layer the transverse size of the calorimeter cells are on order of $\Delta\eta \times \Delta\phi = 0.05 \times 0.05$.

The decision to use liquid argon as the active medium in the DØ calorimeter to sample the ionization produced in particle showering was made based on the stability of the material. Liquid argon has good radiation hardness and is readily flexible to any sort of segmentation scheme in the calorimeter. In addition, liquid argon exhibits unitary gain which results in a relatively simple energy calibration. Between consecutive sections of absorber material in the calorimeter is a 2.3 mm gap of liquid argon followed by a signal readout pad and an additional liquid argon gap. The signal readout board is two sided in order to collect accumulated charge in both the forward and rear liquid argon gaps. The electric field in the gaps is maintained by keeping the signal pads at high voltage with respect to the absorber material which is grounded. The operating parameters of the readout cells produce an electric field of 10,000 V/cm which results in a maximum drift time of 450 ns for electrons collected in the active medium.

The performance of the DØ calorimeter has been studied using test beam, cosmic ray, and collider data. The response of the calorimeter has been measured to be nearly identical for electrons and hadrons. The e/π response ratio of the calorimeter was found to drop from 1.11 at 10 GeV to 1.04 at 150 GeV. Furthermore, the response of both electrons and hadrons was found to be linear within 0.5% over a wide energy range. The energy resolution of the calorimeter can be parameterized as

$$(\frac{\sigma_E}{E})^2 = C^2 + \frac{S^2}{E} + \frac{N^2}{E^2} \qquad (2.1)$$

where the C^2 term comes from scaling effects such as gain variations and deviations from the measured e/π response ratio, the S^2/E term comes from fluctuations in the fraction of energy from a particle shower which is sampled in the calorimeter, and the N^2/E^2 term comes for energy independent noise fluctuations in the uranium and electronics. The energy resolution for electrons in the DØ calorimeter can be parameterized using $C = .003$, $S = .157$, and $N = .330$. The parameterization obtained for pions utilizes $C = .039$, $S = .446$, and $N = .975$. Due to the fact that the middle term in the calorimeter resolution function is the dominant term for both electrons and hadrons, σ_E/E is often quoted as $15\%/\sqrt{E}$ for electrons and $50\%/\sqrt{E}$ for hadrons.

The position resolution of electrons in the calorimeter has also been measured using test beam data. A 1.0 mm resolution is obtained for 100 GeV electrons, and the energy dependence of the resolution is seen to vary as $1/\sqrt{E}$. The ability of the DØ calorimeter to distinguish between electrons and hadrons using the longitudinal energy deposition information has also been checked. Using longitudinal correlation matrices, an e/π discrimination factor of nearly 700 can be obtained with minimal loss in electron efficiency.

2.4 Muon System

The DØ muon system consists of three layers of proportional drift tube chambers surrounding the calorimeter. A magnetized iron toroid is situated between the inner and middle layers of chambers to provide a bend in muon tracks from which a muon momentum measurement and sign determination can be made. A total of five iron toroids are employed to cover nearly the entire solid angle down to within five degrees of the beam pipe. Fig. 2-7 shows a side view of the DØ detector illustrating the position of the five toroids and their associated layers of proportional drift tubes. In the central region of the muon system which covers the angular region

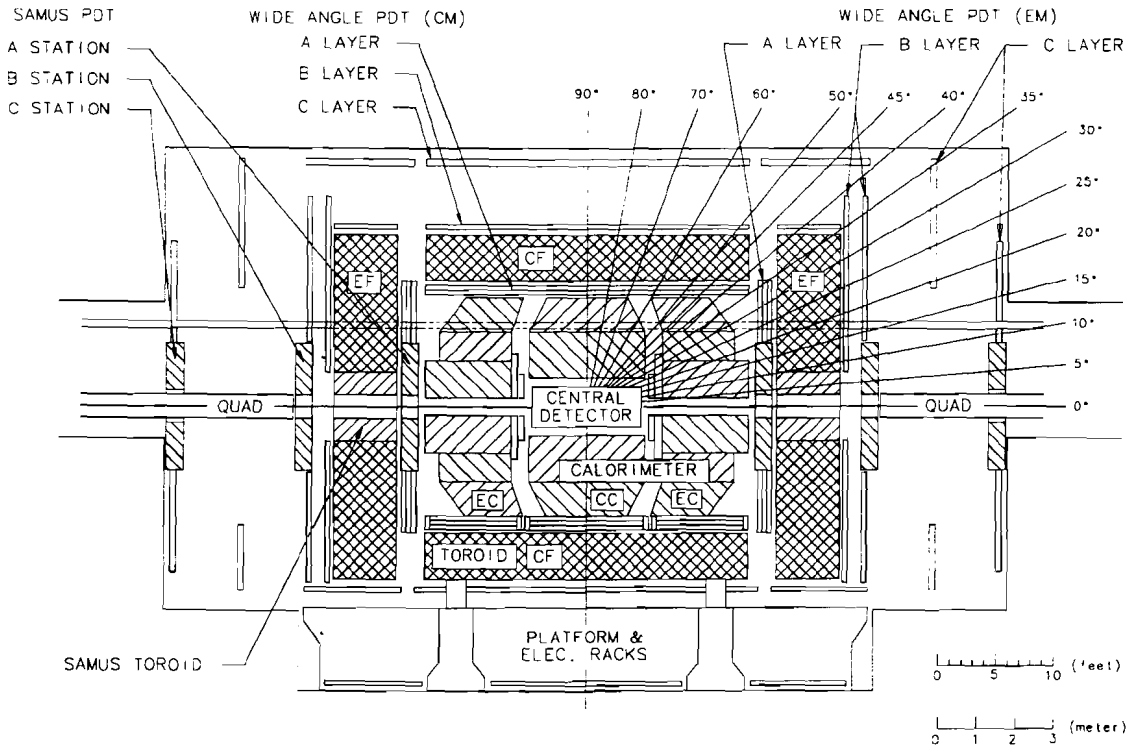

Figure 2-7: Elevation view of the DØ Detector showing the five muon toroids and the approximate arrangement of the A, B, and C layers of proportional drift tubes.

between 40° and 90° with respect to the beam pipe, the muon chambers are oriented in planes parallel to the incident beam direction. Since the magnetic field of the central toroid bends muon tracks primarily in the direction of the incident beams, the chamber wires are strung along the incident beam direction to provide maximum resolution in the bend view. The angular region between 10° and 40° is covered on both ends of the detector with additional chambers oriented in planes perpendicular to the incident beam direction. As in the case of the central region, the chamber wires are strung along the direction of maximum bend. The bend direction is rotated 90° between end chambers on the top and bottom compared with those on the sides due to a similar rotation in the magnetic field direction.

A separate proportional drift tube system is used to detect muon tracks at very small angles with respect to the incident beam direction. The small angle system utilizes three planes of drift tubes oriented at 45° with respect to each other on each of the three chamber layers. This arrangement allows for the reconstruction of a three dimensional tracking coordinate based on hit information alone. This method differs from that employed in the wide angle chambers where two sided wire readout and pad information is used to determine a hit coordinate along the wire direction.

The total number of nuclear interaction lengths seen by a particle passing through the calorimeter and muon toroid as a function of emission angle is shown in Fig. 2-8. The large amount of material between the interaction point and the outer two layers of muon chambers ensures that the background of reconstructed tracks in the muon system due to hadronic punchthrough is minimized. The estimated punchthrough probability for hadronic particles into the outer two layers of the DØ muon system is less than 10^{-4} per prompt muon. The lack of hadronic activity in the muon system also allows for excellent muon identification within jets which allows for the tagging of jets from heavy flavour decay.

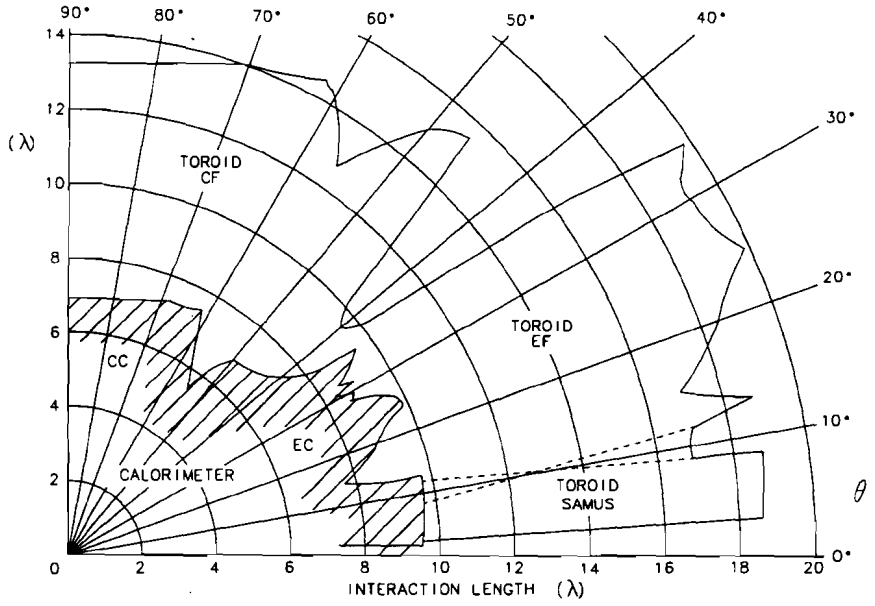

Figure 2-8: Thickness of the DØ calorimeter modules and muon toroids as a function of polar angle.

The direction of a muon track prior to entering the iron toroid is determined using hit information from the inner layer of chambers combined with the position measurement of the primary interaction point and central tracking information. Track direction outside the toroid is determined from hits on the outer two layers of chambers which are separated by 1.0-1.5 m. A comparison of the incident and exit direction of a track determines the bend angle of the muon in the magnetic field of the toroid from which the particle momentum can be calculated. The momentum resolution for muons is primarily limited by multiple Coulomb scattering of the muon tracks in the calorimeter and iron toroids. This effect places a lower limit on muon momentum resolution of $\delta p/p = 18\%$. The effect of chamber hit resolution on muon momentum resolution is not significant except for very high momentum tracks. The muon resolution in the central region of the detector can

be parameterized as

$$\delta(1/p)/(1/p) = [(0.18(p-2)/p)^2 + (0.008p)^2]^{1/2}. \quad (2.2)$$

The first term in (2.2) is due to multiple scattering effects and the second term is due to chamber resolution. Toroid width varies from 1.1 m in the central region to 1.5 and 1.6 m in the end and small angle regions respectively. The magnetic field strength in all toroids is on the order of 2.0 Tesla. The current required to produce these fields is 2500A in the central and end toroids and 1000A in the small angle toroids.

2.4.1 Wide Angle Muon Chambers

A total of 164 individual drift tube chambers are used to provide muon coverage in the wide angle region of the detector. The chambers in the outer two layers of coverage outside the muon toroid contain three planes of drift cells, and the chambers in the inner layer utilize a total of four planes. Chamber planes are offset from each other to resolve left-right drift time ambiguities at the individual cell level. The length and width of the chambers differs depending on their position within the muon system. Chamber cell length varies between 191 and 579 cm, and each chamber plane consists of 14 to 24 cells. Individual cells have a height of 5.5 cm and a width of 10.1 cm. The drift tube design utilizes cathode pads at the top and bottom of each cell and a 50 μm gold-plated tungsten anode wire at the cell center. The high voltage on the wire and pads is held at + 4.65 kV and + 2.30 kV respectively which creates an electric field within the drift cell as illustrated in Fig. 2-9. The gas mixture in the drift cells is $Ar(90\%)/CF_4(5\%)/CO_2(5\%)$ which produces a drift velocity on the order of 6.5 cm/μs.

The drift cell wires are jumpered together in sets of two at the back end of the chambers to allow for two sided wire readout using the front end electronics

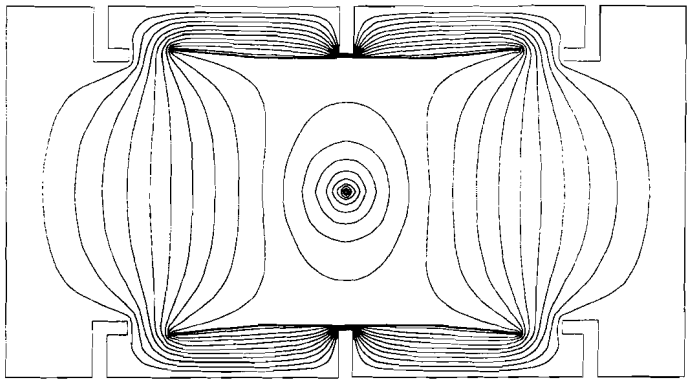

Fig. 4 ELECTROSTATIC EQUI-POTENTIAL LINES OF 4" PDT CELL SIGNAL WIRE AT +5 KV, AND VERNIER PADS AT +2 KV

Figure 2-9: Single cell depiction of a WAMUS PDT showing the equipotential surfaces surrounding the cathode pads and anode wire.

package. The relative arrival time of a signal at the front of the two cells provides a rough measure of the hit coordinate along the wire direction. The signal arrival time with respect to the $p\bar{p}$ bunch crossing is used to estimate the drift distance within the cell to obtain a hit position along the cell width. The chamber electronics are designed to accommodate two hits per wire to allow for the possibility of associated δ-rays. The charge collected on the cathode pads is readout independently for each cell. Both the top and bottom cathodes actually contain two pads separated by a repetitive diamond shaped insulating pattern as illustrated in Fig. 2-10. The signal from the inner and outer pads are readout separately, and the ratio of charge between the two is used to make a higher resolution determination of the hit coordinate along the cell length. The position ambiguity which results from the fact that the pad pattern in the cathodes repeats itself every 30 cm is resolved using the rough measurement obtained from the difference in signal arrival time at the two ends of the wire.

Wide angle muon chamber performance has been tested extensively with cosmic rays. Resolution in the drift direction was determined to be $\pm$ .53 mm using a completely linear relationship between drift time and distance. This resolution can

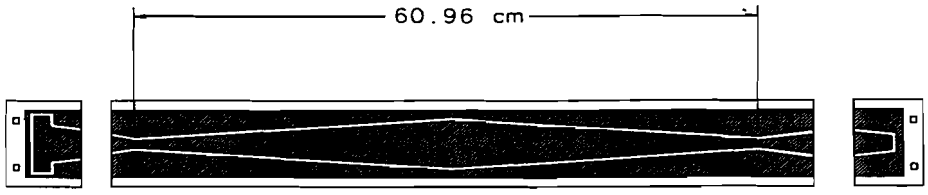

Figure 2-10: Layout of the two separate electrodes which make up the PDT cathodes. The signals from the outer and inner cathodes are readout independently.

be reduced to $\pm$ .30 mm using fits to measured drift time versus distance curves which do not assume complete linearity. The rough measurement of hit position along the wire direction using the difference in signal arrival time at each end of the wire was determined to have a resolution which varied between $\pm$ 9 cm for hits at the back end of the cells and $\pm$ 23 cm for hits near the edge of the cells closest to the electronics. This resolution was determined to be sufficient for resolving the ambiguity in the fine measurement made from pad information. The resolution of the hit coordinate along the wire direction was found to be $\pm$ 1.6 mm when pad information was included.

2.4.2 Small Angle Muon Chambers

As previously mentioned a separate configuration of proportional drift tubes is used to provide muon coverage at very small angles with respect to the incident beams. In the small angle region three planes of drift tubes oriented at 45° with respect to each other are utilized for each of the three required layers of muon

coverage. The basic design of the small angle drift tubes employs a 3 cm diameter stainless steel tube with a 50 μm gold-plated tungsten anode wire strung down the center. The high voltage on the anode wire is held at + 4.0 kV and the outer edge of the tubes are grounded. The $CF_4(90\%)/CH_4(10\%)$ gas mixture utilized in the drift tubes produces an average gas drift velocity of 9.7 cm/μs which gives a maximum drift time of 150 ns.

No position measurement along the wire direction is made in the small angle drift tubes. Instead, a three dimensional track position is determined for each layer of muon coverage using the hit information from each of the three rotated planes of tubes. The performance of the small angle chambers was tested using a 40 GeV muon test beam. Hit resolution in the drift direction was determined to be $\pm$ .35 *mm*. As in the case of the wide angle chambers, the relationship between drift time and distance was found to deviate slightly from linearity. Fits to measured drift time versus distance curves are required to achieve the resolution quoted above.

2.5 Trigger System

The DØ trigger framework is designed to reduce the 285.7 KHz rate of $p\bar{p}$ bunch crossings at the central interaction point of the detector into 3-4 Hz of interesting events which pass into the final data sample. The trigger is constructed from three increasingly sophisticated levels of event characterization. A Level 0 scintillator based trigger is used to identify inelastic collisions associated with the bunch crossings in the accelerator. The $p\bar{p}$ interaction cross section at DØ has been determined to be 46.7 $\pm$ 2.5 mb. At a typical luminosity obtained from the collider during the 1992-93 run ($\mathcal{L} = 5 \times 10^{30}$ cm^{-2} s^{-1}), Level 0 provides an approximate reduction factor of two in the incident beam crossing rate. Electron, jet, and muon candidates as well as events with large missing transverse energy are identified using the Level 1 hardware trigger. Level 1 triggering decisions are required to be made

within the 3.5 μs bunch crossing interval, but an additional triggering level (Level 1.5) can also be utilized in cases where improved triggering information can be made available within the time scale of several additional bunch crossings. The event rate which passes the trigger requirement at Level 1 is on the order of 200 Hz and can generally be reduced by an additional factor of two with further conditions at Level 1.5. Detector readout is reserved for the remaining 100 Hz event rate. Events are readout into Level 2 software nodes where event reconstruction routines are run to pick out the most interesting 3-4 Hz of events to be written to tape. A more detailed description of each triggering level can be found in the subsequent sections.

2.5.1 Level 0 Trigger

As previously mentioned the Level 0 trigger is used to register the presence of an inelastic collision at the interaction point. The trigger is formed using sets of scintillation counters mounted on the front surfaces of the end calorimeters. The scintillators provide nearly complete coverage in the pseudorapidity range where $2.3 < |\eta| < 4.3$ and partial coverage over a somewhat wider range. This coverage was chosen to provide a $\geq$ 99% efficiency for detecting non-diffractive inelastic collisions with a coincidence in the scintillators at both ends of the detector. The Level 0 trigger hardware also provides several other important functions. From the relative arrival time of particles at the Level 0 counters found at both ends of the detector, a position measurement of the primary interaction point along the incident beam direction is made for use in the subsequent triggering levels. This information is important since the large spread in vertex position along the beam direction (σ = 30 cm) influences E_T measurements of calorimeter objects at both subsequent trigger levels and E_T measurements of muon tracks at Level 2. The time resolution of the scintillators is on the order of 100-150 ps which

leads to fast vertex position resolution of 8 cm for utilization in Level 1 and a slow vertex position resolution of 3 cm for use in Level 2. The Level 0 hardware also has the ability to flag beam crossings with multiple interactions for which the timing information is more ambiguous. At the analysis level combined information obtained at Level 0 is used to measure the effective luminosity received from the accelerator.

2.5.2 Level 1 Trigger

Level 1 Framework

In order to avoid detector deadtime, a triggering decision must be made within the 3.5 μs interval between bunch crossings at the DØ interaction point. Each detector subsystem has specific Level 1 trigger hardware to construct candidates for physics objects from event information within the particular subsystem. This information is passed to the Level 1 framework within the required time interval where it is combined with other accelerator related information which can also be utilized in triggering decisions. The trigger framework then looks for preselected combinations of physics objects and other trigger information to select good events. The actual trigger selection is performed using a two dimensional AND-OR network with 256 latched bits to receive the disparate trigger information. A total of 32 specific Level 1 trigger conditions which are constructed from different combinations of the bits in the AND-OR network can be defined for a single period of data taking. The Level 1 framework is also responsible for prescaling specific trigger conditions with unacceptable event rates and controlling detector readout. If an event is found to pass any of the 32 specific Level 1 triggering conditions which do not require Level 1.5 confirmation, the trigger framework initiates immediate readout of the detector. In cases where Level 1.5 confirmation is required for each of the specific triggering conditions which pass at Level 1, the trigger framework holds

off the detector from further event collection over subsequent bunch crossings until confirmation of one trigger condition or rejection of all conditions is obtained. A small amount of detector deadtime is induced from this confirmation process, but it has been found to be insignificant when compared to other sources of detector deadtime.

Level 1 Calorimeter Trigger

The calorimeter trigger is designed for flexibility in triggering on several different types of physics objects which can be identified from energy deposition in the calorimeter. Individual objects such as electrons, photons, and jets can be identified from energy deposition in specific sets of calorimeter towers. Conversely, objects such as neutrinos which deposit only a minute fraction of their incident energy in the calorimeter can be identified from an unbalance in the total transverse energy deposition. New particles with large mass can often be identified less directly from the total transverse energy deposition in an event. The calorimeter trigger hardware is designed to provide information with regard to all these variables within the allotted time frame between beam crossings.

Calorimeter towers are summed in groups of four for triggering purposes at Level 1 which gives a trigger tower width of $\Delta\eta \times \Delta\phi = 0.2 \times 0.2$. Each tower provides independent analog signals to the trigger hardware for both electromagnetic and hadronic deposition. The signals are passed through a resistor network which weights the input signals by the sine of the angle between the particular trigger tower and the incident beam direction. This action has the effect of converting energy deposition into transverse energy deposition assuming a primary interaction vertex at the midpoint of the detector. Next, each analog signal is digitized into an eight bit word which is combined with three bits of vertex information from the Level 0 fast vertex determination. A lookup table is then utilized

to provide a transverse energy value for each electromagnetic and hadronic tower above some preset threshold. Finally, each value is compared to up to four programmable thresholds which provides a count of the number of towers found above each threshold. Good electromagnetic towers are defined to be those where the electromagnetic deposition resides above threshold, while hadronic deposition in the same tower resides below threshold.

A total of 32 bits in the Level 1 AND-OR network are utilized to make this information available for use in specific trigger definitions. Electromagnetic tower information is translated into 16 bits of trigger information each of which corresponds to a trigger tower count between 1-4 for one of four programmable thresholds. The remaining 16 bits are used in an identical construction for combined electromagnetic and hadronic tower information. Total transverse energy is determined through a separate circuit which passes the combined electromagnetic and hadronic deposition information from each tower into a 9 bit summation device. The sum is compared to eight programmable thresholds to form eight additional bits of information for the Level 1 AND-OR network.

The formation of the missing transverse energy variable follows a somewhat different path. In this case the electromagnetic and hadronic deposition information is combined for each individual tower prior to being inputed into the transverse energy lookup tables. The combined information is sent into two independent lookup tables which output the transverse momentum components P_x and P_y for each tower. The outputs from these lookups are then sent into circuits which produce a sum for each component over all trigger towers. Missing transverse energy is then constructed from the two individual components; and as in the case of total transverse energy, the final value is compared to eight programmable thresholds which provide eight additional bits of information for use in the Level 1 AND-OR network.

Level 1 Muon Trigger

The Level 1 muon trigger is designed to identify muon track candidates using single latch bit information from each of the $\sim$ 16700 drift cells in the muon system. The trigger hardware is separated into five distinct pseudorapidity regions corresponding to the areas of coverage for each of the muon toroids. Each muon chamber has a corresponding Module Address Card (MAC) which receives latch information from all drift cells within the chamber and forms centroids based on hit patterns within the chamber planes. Centroids are defined to be the most likely half cell along a muon track as projected to the middle plane in the case of the three tiered chambers found in the outer two layers and the plane closest to the toroid for the four tiered chambers found in the inner layer. Centroid width is 5 cm for wide angle chambers and 1.5 cm for small angle chambers.

The centroids are output from the MAC cards as bit patterns which in the case of Level 1 correspond to the logical OR for groups of 3(4) consecutive centroid patterns in wide (small) angle chambers. Level 1 trigger information is formed using Coarse Centroid Trigger Cards (CCTs) which receive centroid information from each of the three layers of chambers within a given region of η-ϕ space and search for combinations of centroids from those layers which are representative of muon tracks originating from the interaction region. In the case of wide angle chambers, the CCT cards perform an additional logical OR on the centroid patterns it receives prior to searching for triggers which further reduces the hit resolution by an additional factor of four. The net hit resolution utilized at Level 1, 60 cm in the wide angle chambers, is a direct consequence of the need to produce a triggering decision within the 3.5 μs interval between bunch crossings.

Three levels of CCT cards are used to sort out the large rate of hits in the small angle chambers for Level 1 triggering purposes. At the first level a search is performed for matching combinations of hits in the three rotated planes of tubes

found in each layer. These hit combinations are then input into a second layer of CCT cards where searches for track roads through the three chamber layers are performed along each of the three tube rotations. The final CCT layer identifies muon candidates by matching roads reconstructed along each of the three tube rotations. All CCT output is directed to master cards which count the number of muon candidates identified in each pseudorapidity region. The combined information is then mapped into 16 bits which are passed to the Level 1 trigger framework. The mapping is dependent on the different muon requirements found within the 32 specific Level 1 trigger conditions defined for a specific period of data taking. A special device known as the Trigger Monitor Card (TRGMON) creates a mapping between the final muon track candidate counts from each pseudorapidity region and individual bits of information corresponding to each of the individual muon requirements found within the 32 specific Level 1 trigger conditions. These individual bits of information are then passed into the AND-OR network of the trigger framework.

Level 1.5 Muon Trigger

When the muon system receives confirmation of a good Level 1 trigger from the framework, the MAC cards associated with each chamber in the system automatically strobe their full centroid lists to Octant Trigger Cards (OTC's) which are utilized in making Level 1.5 muon trigger decisions. Each OTC has three input layers to receive centroids from each of the chamber layers found within the region of η-ϕ space for which the OTC provides trigger coverage. The combination of centroids from each of the three input layers form two addresses to one bit readable memories on the cards. These memories are downloaded prior to data collection and incorporate information from offline track momentum calculations which were done for each potential centroid combination.

The calculation of track momentum was based on the potential bend angles of a muon track through the iron toroid consistent with the given centroid combinations and a point of origin within 3σ of the central interaction vertex. Since the Level 1.5 trigger makes use of the full centroid resolution, it is possible to restrict triggering to track candidates above a certain transverse momentum threshold with an upper limit of ~ 7 GeV. For centroid combinations which are consistent with tracks above the required P_T threshold both of the one bit memory locations derivable from the centroid patterns are preset to one. As the centroids are strobed into the OTC cards, each potential combination of centroid patterns from the three layers is checked against its corresponding memory locations for trigger confirmation.

Each OTC has the ability to check up to sixteen combinations in parallel which significantly decreases the processing time required to make a Level 1.5 trigger decision. Processing time in the wide angle regions of the muon system is typically less than 2 μs which is less than the interval between beam crossings. In the small angle regions, however, multiple stages of OTC lookups are required to sort through the large flux of hits which can increase processing time to over 100 μs. The scheme used in this region for Level 1.5 is very similar to that utilized in the Level 1 trigger. One set of OTC cards looks for consistent hits in each of the three rotated planes of cells found in the middle chamber layer to provide a three dimensional space point. Two additional sets of OTC cards look for track roads between chamber layers along two out of three possible cell rotations. These three sets of cards provide the input layers for a final set of OTC's which looks for matches between the roads and the three dimensional space point in the middle layer.

Good triggers from individual OTC cards are collected into OTC Manager (OTCMGR) Cards which are provided for each of the five pseudorapidity regions of the muon system. Each OTCMGR counts the number of good Level 1.5 track

candidates found in its region and reports this information to the TRGMON which, as in the case of Level 1, transcribes the combined information into bits for the trigger hardware corresponding to muon Level 1.5 requirements found in specific trigger definitions. The trigger framework is designed to ignore all Level 1.5 information it receives in cases where a specific trigger not requiring Level 1.5 confirmation passes at Level 1. However, in cases where Level 1.5 confirmation is required, the trigger framework will continue to poll the Level 1.5 bits sent from the TRGMON to the framework until confirmation is obtained or separate DONE lines indicate that Level 1.5 processing is complete. OTCMGR cards also provide the important function of passing muon trigger information into the data stream. The centroid information associated with each good Level 1.5 muon track candidate can be reconstructed offline which allows for hardware stability tests against software simulations utilizing cell hit information also available in the data stream.

2.5.3 Level 2 Trigger

Detector readout into 1 of 50 available Level 2 VAX workstations for software event-filtering is done for all events which satisfy one or more of the specific trigger definitions at Level 1/Level 1.5. Level 2 utilizes software filtering to reduce the $\sim$ 100 Hz event rate of detector readout into the $\sim$ 3-4 Hz rate of events which are written to tape. The Level 2 filters are constructed from specific software algorithms referred to as filter tools which identify specific types of particles or event characteristics. Examples of Level 2 filter tools are those used to identify jets, muons, electromagnetic calorimeter clusters, and missing transverse energy. In general, filter tools are modified versions of offline reconstruction algorithms which have been streamlined to execute within the time constraints of the trigger.

Detector modeling indicates that deadtime due to Level 2 processing will be less than 2% as long as the average event processing time is $\leq$ 70% of the average

time between events sent to a specific node. The processing time corresponding to this condition for a 100 Hz readout rate is on the order of 350 ms which is well above the 200 ms average processing time observed in the course of data collection.

Each of the thirty-two specific trigger definitions utilized at Level 1/Level 1.5 has one or more associated sets of Level 2 conditions which are referred to as scripts. Each script is constructed from some subset of the filter tools available in the Level 2 nodes where the requirement of a specific filter tool can also include criterion on the output parameters associated with the particular tool. For example, the muon filter tool has an output parameter for the transverse momentum associated with a reconstructed track which allows for variable minimum P_T requirements for good Level 2 muon tracks in different script definitions. The total number of script definitions allowed for in the trigger framework is 128 which can be sorted between the Level 1/Level 1.5 specific trigger definitions in any configuration. For events which pass one or more of the sets of Level 2 conditions associated with the particular specific trigger definitions through which the events were passed at Level 1, raw event data passes from the Level 2 node to hard disk storage from where it is written to tape through a separate utility.

Chapter 3

Data Selection

3.1 Data Collection and Processing

The data sample utilized in this analysis was collected during the 1992-93 collider run at the Fermi National Accelerator Laboratory. The data set was restricted to events obtained after the January 1993 shutdown when changes were made to the muon trigger hardware which enhanced the detector acceptance for dimuon events. As the collider run progressed known problems with detector hardware were recorded. This information was used to remove events from specific runs in which detector hardware relevant to this analysis was broken [26]. As previously mentioned in Section 2.5, the typical instantaneous luminosity obtained from the accelerator during the course of the 1992-93 collider run was on the order of $\mathcal{L} = 5 \times 10^{30}$ cm^{-2} s^{-1}. The total integrated luminosity received by the DØ detector during the 1992-93 collider run was 13.5 pb^{-1}. Approximately 58% of this total was accumulated during postshutdown running of the detector.

3.1.1 Event Reconstruction

The reconstruction of the momenta and trajectories of particles produced in $p\bar{p}$ collisions from the raw hit information output from each detector subsystem is performed with offline computer farms. All raw data events collected in the 1992-93

collider run were processed using versions 11.17-11.19 of the full DØ reconstruction package. Reconstructed events were assigned to different event streams based on their physics content. The dimuon event stream utilized in this particular analysis is discussed in Section 3.1.2. The existence of a software bug in the version 11 reconstruction package which assigned incorrect values to the fit quality parameters associated with global muon track reconstructions necessitated the subsequent processing of each event through an additional software routine which corrected these parameters. Additional calibration of jet, electron, and missing transverse energy scales was also performed subsequent to event reconstruction with the CAFIX [27] software package. A further description of this package is provided in Section 4.3.1.

3.1.2 Dimuon Event Stream

A dimuon event sample was separated from the global event stream using a loose set of cuts designed to have no impact on the overall efficiency for good beam produced dimuon events in the final data sample. Since more stringent versions of the cuts used in the streaming of these events were included in subsequent event selection criteria, the event streaming cuts had no independent net effect on the final event sample. A list of the cuts used at the event streaming level are listed below along with a reference to the section where a more stringent version of the particular muon selection criteria is discussed.

- Each event was required to have at least one pair of reconstructed muon tracks where the sum of the corresponding IFW4 track quality flags was two or less (see Section 3.2.1).

- Each muon candidate in the pair was required to have associated minimum ionizing energy in the calorimeter. The energy in the calorimeter cells along

the muon track plus the two nearest neighbor cells was required to be greater than 1 GeV for each muon candidate (see Section 3.2.2).

- The 3-D opening angle defined as the dot product of the direction cosines of the two muon track segments outside the iron toroid was required to be less than 160 degrees unless one of the muon tracks had an associated floating t_o parameter as described in Section 5.4.1 less than 100 ns (see Section 3.2.2).

The total number of events in the global event stream corresponding to the entire postshutdown data sample is on the order of 6×10^6. Approximately 6% of the total event sample was selected for the dimuon event stream based on the streaming cuts described here.

3.1.3 Trigger Requirements

Three different trigger conditions were used to select events for the mixing analysis. Each trigger condition required the presence of a good Level 0 trigger corresponding to the presence of an inelastic collision within the interaction region of the DØ detector as discussed in Section 2.5.1. In addition, each trigger condition included main ring veto conditions referred to as MRBS-LOSS and MICRO-BLANK. As discussed in Section 2.1, the main ring accelerator was used to produce antiprotons during the periods when $p\bar{p}$ collisions were taking place in the Tevatron. During the injection and transition phases of the 2.4 s antiproton production cycle, losses from the main ring which passes directly through the top half of the DØ detector appeared in both the innermost layer of the muon system and the coarse hadronic section of the central calorimeter module. These losses also caused a temporary high voltage sag in the muon chambers nearest to the main ring which lasted on the order of 400-500 ms after injection. In order to avoid collecting events during this period the accelerator clock was used to veto a 0.4 s interval starting at the point of

Name	L1 Muon	L1 Jet	L2 Muon	L2 Jet	Luminosity
Mu-2-High	2	None	2 3 GeV/c *	None	6.57 pb^{-1}
Mu-1-Jet	1	1 3 GeV	1 3 GeV/c	1 10 GeV	3.71 pb^{-1}
Mu-Jet-Low	1	2 3 GeV	1 3 GeV/c *	1 10 GeV	6.51 pb^{-1}
* At least one muon has perfect quality flag					

Table 3-1: Trigger conditions used in the mixing analysis.

injection. The veto of this interval was controlled with the MRBS-LOSS term and resulted in a 17% loss in integrated luminosity. Additional main ring losses were incurred during the remaining period of the antiproton production cycle whenever proton bunches in the main ring passed through the collision hall. The veto of events in which a proton bunch in the main ring passed through the collision hall within 800 ns of a $p\bar{p}$ bunch crossing in the Tevatron was controlled with the MICRO-BLANK term. The additional resulting loss in integrated luminosity associated with the inclusion of the MICRO-BLANK term was 9%.

The Level 1 and Level 2 requirements associated with each of the three trigger conditions utilized in this analysis are summarized in Table 3-1. As discussed in Section 2.5.2, a Level 1 muon track road in the central detector region ($|\eta_\mu| \leq 1.0$) was required to contain hits in at least two of the three layers of chambers in the wide angle system. The minimum momentum of a muon which is able to traverse the central iron toroid and leave hits in the outer two chamber layers is on the order of 3 GeV/c. Hence, the effective turn on of the muon Level 1 trigger was chosen at a muon transverse momentum value of 3 GeV/c which corresponds to the minimum possible transverse momentum of a muon track at $\eta_\mu = 0$. A similar transverse momentum threshold was chosen for the Level 1 muon trigger in the end regions of the detector. In order to combat higher combinatoric backgrounds, however, level 1 muon track roads in this region were required to contain hits on all three layers of the muon system. Level 2 muon track candidates were required to

have IFW4 track quality flags (see Section 3.2.1) which were less than or equal to one. The Mu-2-High and Mu-Jet-Low trigger conditions contained an additional restriction in that at least one level 2 muon track candidate within a given event had to have an IFW4 parameter equal to zero. Tracks which were identified as potential cosmic ray candidates using the MUCTAG cut described in Section 3.2.2 were also rejected as Level 2 track candidates. In order to satisfy the Mu-2-High and Mu-1-Jet trigger conditions, muon track candidates were required to lie within the pseudorapidity range where $|\eta_\mu| \leq 1.7$. The Mu-Jet-Low trigger condition, on the other hand, was satisfied by muon track candidates in the somewhat wider pseudorapidity region where $|\eta_\mu| \leq 2.4$.

As previously discussed in Section 2.5.2, pseudoprojective calorimeter towers were summed in groups of four for triggering purposes at level 1. The corresponding width of trigger towers in the DØ calorimeter was $\Delta\eta \times \Delta\phi = 0.2 \times 0.2$. Trigger towers with a combined energy (electromagnetic + hadronic) greater than 3 GeV satisfied the intrinsic Level 1 jet requirement associated with the Mu-1-Jet and Mu-Jet-Low trigger conditions. Level 2 jet reconstruction utilized an equivalent technique to that discussed for offline jet reconstruction in Section 3.3.1 with a jet cone size of $\Delta R = 0.7$. Both Level 1 and Level 2 jet trigger candidates were restricted to the pseudorapidity range where $|\eta_{jet}| \leq 3.2$.

The total integrated luminosity associated with each of the different trigger conditions used in this analysis is dependent on prescales which varied as a function of the instantaneous luminosity received from the accelerator. The luminosity of each trigger corresponding to the subset of detector runs utilized in this analysis was determined using an offline luminosity utility which accessed the DØ run information database and calculated the total integrated luminosity associated with a specific trigger condition over a specific subset of runs [28]. The utility accounted for the prescale associated with each of the different trigger conditions and corrected for

multiple interactions and detector dead time on a run by run basis. The resulting integrated luminosity corresponding to each of the three trigger conditions is shown in Table 3-1.

3.2 Offline Muon Identification

3.2.1 Muon Track Selection Criteria

A series of cuts was made on muon tracks in the dimuon data stream to select out events with two high quality muon candidates. The transverse momentum and pseudorapidity of both muon candidates were also restricted to limited ranges for reasons described in greater detail below.

- **Muon Pseudorapidity Cut**

  Reconstructed muon tracks utilized in this analysis were restricted to the pseudorapidity range where $|\eta_\mu| \leq 0.8$. As illustrated in Fig. 2-7 all of the hits along muon tracks in this pseudorapidity region are constrained to lie in the wide angle muon chambers which form the central section of the muon system. The pseudorapidity range from $0.8 \leq |\eta_\mu| \leq 1.1$ where the central and end toroids meet was specifically avoided due to the smaller amount of detector material found in this region. Muon tracks in this range have inferior momentum resolution due to the smaller integrated magnetic field traversed by the muon. In addition, the absence of material in this region increased the probability for the misidentification of punchthrough particles as prompt muons.

  Muon tracks in the pseudorapidity range from $1.1 \leq |\eta_\mu| \leq 2.4$ were eliminated due to aging problems with the wide angle muon chambers in that region. These chambers were subjected to large amounts of background radi-

ation associated with accelerator operation during the course of the collider run. The glasteel material on which the muon drift cell pads were etched was found to outgas over the course of run and coated the cell wires which greatly reduced the hit efficiencies in those chambers. Muon track reconstruction efficiencies were therefore greatly reduced and a negligible number of events were collected in this region.

The small angle muon chambers which exclusively cover the pseudorapidity range $|\eta_\mu| \geq 2.4$ were not subject to these aging problems, but the lack of an acceptable trigger in this region for the 1992-93 collider run prevented the collection of a substantial data set in this range.

- **Muon P_T Cut**

  Although a restriction on the transverse momentum range of muon candidates in the dimuon event sample was eventually utilized as a topological cut (see Section 5.2.4), a minimum and maximum cut on the transverse momentum of reconstructed muon tracks was also included in the initial identification of muon candidates. The transverse momentum of each muon track was restricted to lie in the region 3 GeV/c $\leq P_T^\mu \leq$ 25 GeV/c. The top half of Fig. 3-1 shows the reconstruction efficiency for Monte Carlo generated single muon events in the pseudorapidity range where $|\eta_\mu| \leq 0.8$. As illustrated in the figure, the reconstruction efficiency for muons with an intrinsic transverse momentum below 3 GeV/c approached zero. The vast majority of these low P_T muon candidates were found to range out in the large amount of detector material in the calorimeter and muon iron toroid along the muon path and could not be reconstructed due to a lack of hits in the outer two layers of the muon system. The few reconstructed muon tracks with $P_T \leq 3$ GeV/c were therefore in most cases the result of higher P_T muons with large multiple scattering or random hits in the detector and were therefore eliminated.

Since the correct sign determination of reconstructed muon candidates was of particular importance in this analysis, muon transverse momentum ranges with below average efficiencies for correct sign reconstruction were also excluded. The bottom half of Fig. 3-1 shows the correct sign reconstruction efficiency for Monte Carlo generated single muon events in the pseudorapidity range where $|\eta_\mu| \leq 0.8$. The correct sign reconstruction efficiency is plotted as a function of the reconstructed track P_T rather than the incident P_T of the muon candidate. Since high P_T muon tracks exhibit very little bend in the magnetic field of the muon toroid, the determination of the sign of these muon candidates was more difficult. The upper transverse momentum limit of 25 GeV was chosen to coincide with the initial decline in correct sign reconstruction efficiency for high P_T muon track candidates.

- **Muon Track Quality Cut**

Reconstructed muon tracks in events utilized in this analysis were required to pass a minimum standard for track quality. The muon track reconstruction program assigns a muon quality flag referred to as IFW4 based on a discrete set of four track attributes. These attributes are the quality of a track fit in the bend and non-bend directions and the calculated impact parameters of an extrapolated track with respect to the reconstructed event vertex in both views. Each track attribute has an associated minimum standard for a good muon track which in the case of the calculated impact parameters is dependent on both the angle and momentum of the reconstructed muon track. It is important to note that the reconstruction of two-layer muon tracks includes the event vertex as a point in the track fit which means that the impact parameters for this subset of tracks are zero by definition. Each track attribute which does not meet the minimum standard of a good track increments the value of the IFW4 parameter by one. Hence, a muon track

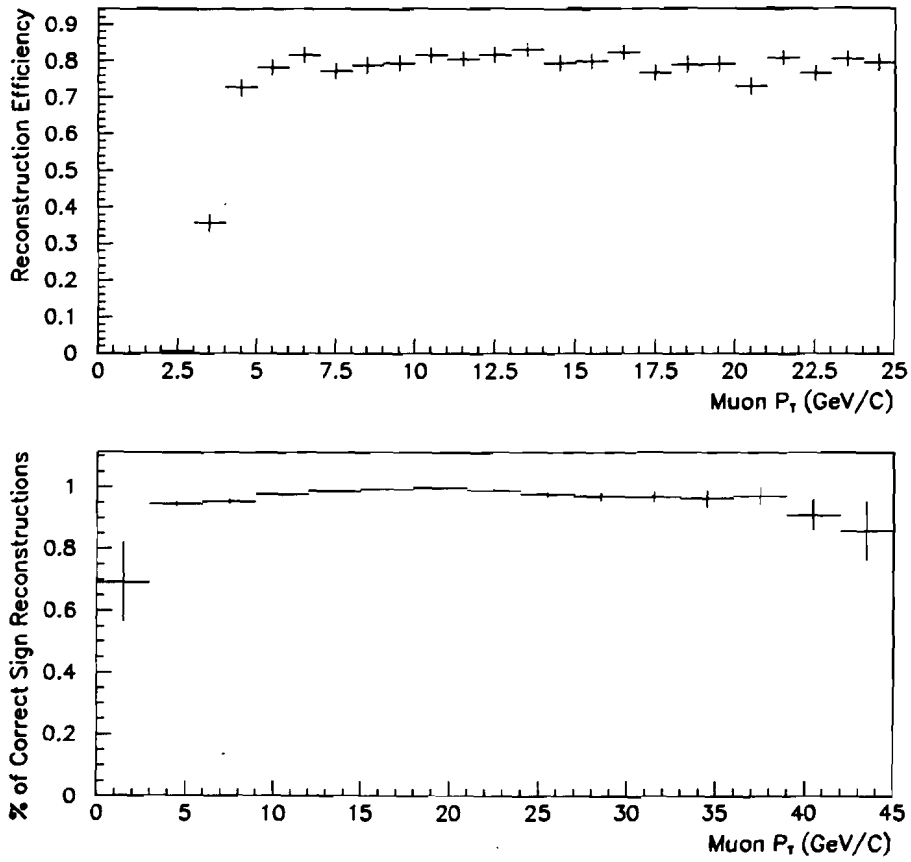

Figure 3-1: (Top) Monte Carlo track reconstruction efficiency of single muon candidates in the pseudorapidity range where $|\eta_\mu| \leq 0.8$ as a function of ISAJET P_T. (Bottom) Percentage of correct sign track reconstructions for single muon Monte Carlo candidates in the pseudorapidity range where $|\eta_\mu| \leq 0.8$ as a function of reconstructed track P_T.

which meets each of the four criteria for a good track has a corresponding IFW4 parameter of zero. An IFW4 track quality flag less than or equal to one was required for all muon candidates utilized in this analysis.

- **Muon Multiplicity**

The offline event selection required at least two muon tracks with IFW4 track quality flags less than or equal to one within the restricted pseudorapidity and transverse momentum range of this analysis. A small number of events which contained four or more reconstructed muon tracks meeting the above conditions were excluded from the final event sample since the event displays associated with this subset of events were very suggestive of particle blasts not related to beam-beam interactions. In addition, at least one of the two leading P_T muons in each event was required to have an IFW4 track quality flag of zero.

- **Magnetic Field Thickness Cut**

As discussed in Section 2.4 the momentum of a muon track candidate is determined from the track bend in the magnetic field of the iron toroid. The observed bend in a muon track is proportional to the integral of the magnetic field induction vector along the path of the muon track through the iron toroid. In order to ensure that all muon tracks in the final event sample met some minimum criterion for momentum resolution, the $\int Bdl$ along each of the two leading P_T muon tracks in the event was required to be greater than 1.7 Tm. A normalized distribution of $\int Bdl$ for muon tracks in the dimuon data stream for which $|\eta_\mu| \leq 0.8$ and 3 GeV/c $\leq P_T^\mu \leq$ 25 GeV/c is shown in Fig. 3-2. The resulting acceptance for good beam produced events in the final data sample based on the 1.7 Tm lower limit on magnetic field thickness was determined to be greater than 95%.

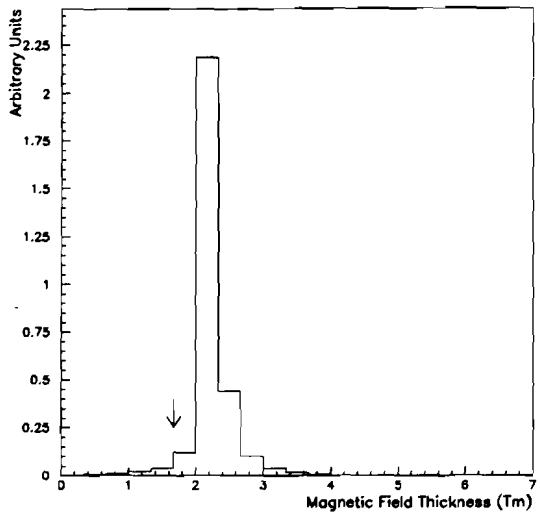

Figure 3-2: Normalized $\int Bdl$ distribution of reconstructed muon tracks in the dimuon data stream for which $|\eta_\mu| \leq 0.8$ and 3 GeV/c $\leq P_T^\mu \leq$ 25 GeV/c.

3.2.2 Cosmic Ray Rejection Cuts

Another set of muon selection criteria was used to help eliminate events in the dimuon data stream due to cosmic ray background. Most of these background events were passed into the data sample because of bias in the muon track reconstruction code towards tracking hits to point back in the direction of the interaction vertex of the event. This bias was most significant in the case of two-layer track fitting where the event vertex was generally included as a point in the track fit. However, even in cases where tracks were reconstructed from hits on all three layers of the muon system, the reconstruction code was inherently inclined towards track fits which pointed to the interaction region of the DØ detector. This bias frequently resulted in the mistracking of cosmic ray muons passing through two opposite sides of the detector giving the appearance of two beam produced muons. The lack of minimum ionizing energy in the calorimeter associated with these poorly reconstructed tracks as well as the lack of matching tracks in the

central tracking chambers made this class of events relatively easy to identify. In a smaller number of cases the track of a cosmic ray through the detector did in fact pass very near to the interaction vertex of a particular event. In general, these events were harder to identify as cosmic rays since the muon tracks identified by the muon reconstruction program were nearly identical to good muon tracks. In order to eliminate this class of events cuts were made on the opening angle between the two reconstructed tracks in each dimuon event. Cosmic ray events which were properly tracked through two opposite sides of the detector were identified as back to back tracks in the reconstruction. The cuts which were utilized to help remove cosmic ray events from the data sample are summarized in more detail below.

- **Minimum Ionizing Energy Confirmation**

  The lack of minimum ionizing energy deposition in the calorimeter was found to be useful in eliminating tracks from cosmic rays where the reconstructed muon track was incorrectly projected back towards the area surrounding the interaction vertex of the event. The parameter used to make this cut was the sum of the energy in the calorimeter cells crossed by the muon track plus their nearest neighbor cells (E_{cal}^{1NN}). Each of the two leading P_T^{μ} tracks in an event was required to have

  $$E_{cal}^{1NN} \geq 1.0 GeV \tag{3.1}$$

  in order to be consistent with the energy deposition associated with a minimum ionizing particle passing through the cells traversed by the muon track. In Fig. 3-3 the distribution of E_{cal}^{1NN} for muon tracks in cosmic ray events taken at the end of collider running is compared to the same distribution for muon tracks in data events which pass all cosmic cuts except for the cut on minimum ionizing energy deposition in the calorimeter. The requirement of a dimuon opening angle of less than 165° as described below was used to

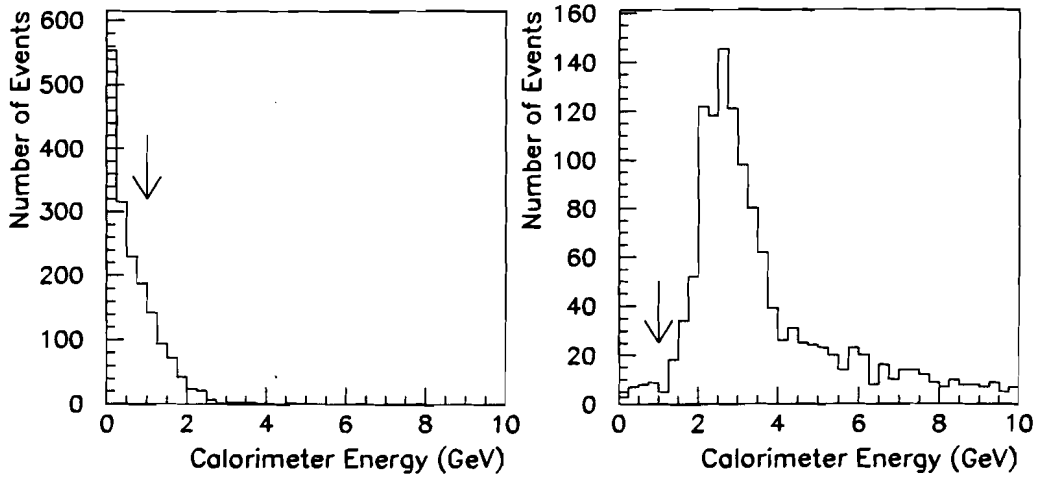

Figure 3-3: Calorimeter energy deposition in cells along the muon track plus their next nearest neighbor cells for (a) muon tracks in cosmic ray events which have a dimuon opening angle less than 165° and (b) muon tracks in data events which pass all cosmic cuts except for the cut on minimum ionizing energy deposition.

select a subset of the cosmic ray events where the reconstructed muon tracks were incorrectly constrained to the interaction vertex of the event. A cut on the invariant mass of the two leading P_T muons in the event such that $M_{\mu\mu} \geq 6$ GeV/c^2 was also made on both distributions to be consistent with topological cuts made later in the analysis.

- **Central Detector Track Match**

Another cut which was found to be useful in eliminating mistracked cosmic ray muons was the requirement that matching Central Detector (CD) tracks be found for each of the two leading P_T muon tracks in a given event. In the DØ reconstruction software a muon was considered to have a central detector track match if a CD track existed within $\Delta\theta \leq 0.45$ radians and $\Delta\varphi \leq 0.45$ radians of the reconstructed muon track. In general, reconstructed cosmic

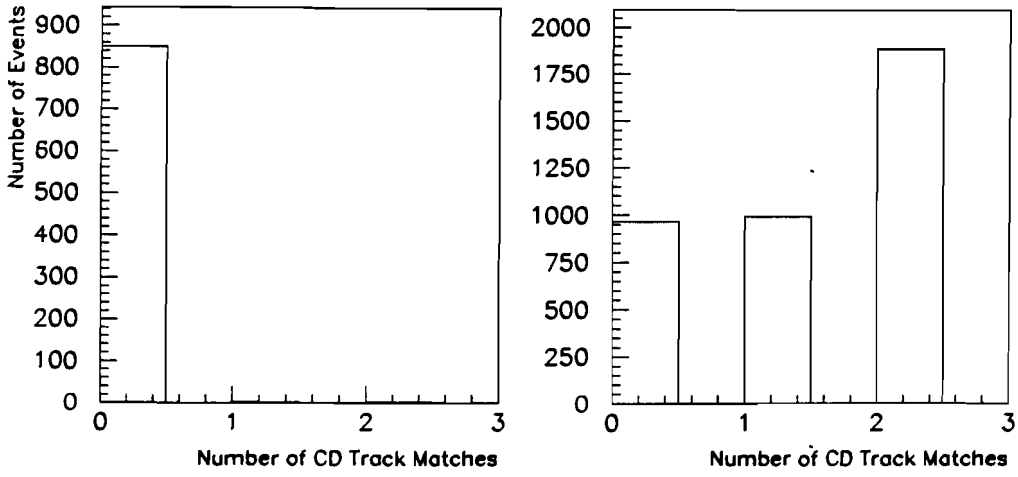

Figure 3-4: Number of CD track matches with the two leading P_T muon tracks in (a) cosmic ray events with a dimuon opening angle less than 165° and (b) data events which pass all cosmic cuts except for those which involve CD matches.

ray tracks which were improperly projected back to the interaction vertex of an event were unlikely to have a CD match in this range. A comparison of the number of CD track matches with the two leading P_T muon tracks per event between the subset of the cosmic ray data sample with a dimuon opening angle less than 165° and the dimuon data sample subjected to all cosmic cuts except for those which involve CD matches is shown in Fig. 3-4. A lower invariant mass cut on the two leading P_T muons of 6 GeV/c^2 was also included here to be consistent with later topological cuts.

Due to the fact that a large number of the cuts which were used to eliminate cosmic ray events in the data sample did in fact involve matching CD tracks, the distribution of CD matches per event shown for the dimuon data sample with all cosmic cuts except those involving CD matches should not be considered to be uncontaminated with respect to cosmic ray events. However,

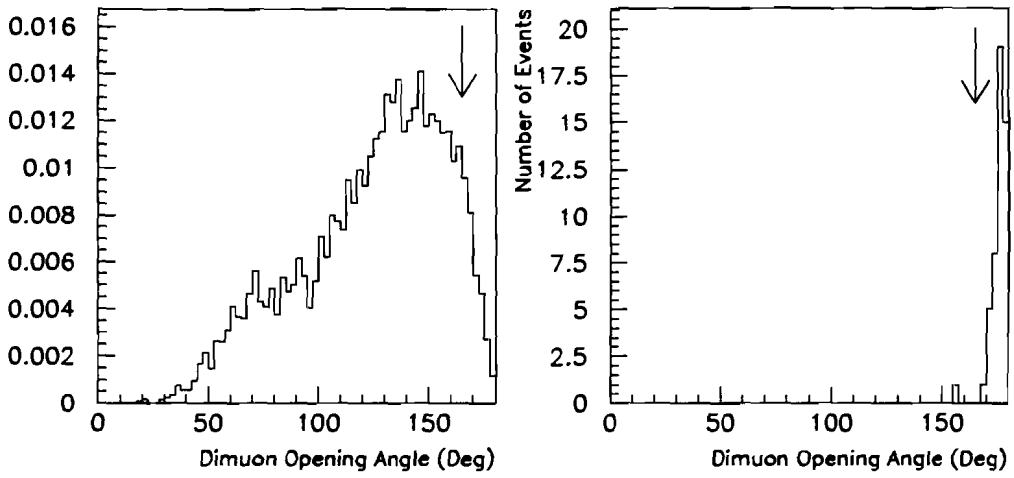

Figure 3-5: (a) Normalized dimuon opening angle distribution for $b\bar{b}$ Monte Carlo events with a calculated invariant mass greater than 6 GeV/c^2 and (b) dimuon opening angle spectrum for cosmic ray events in which both muons pass the cut on minimum ionizing energy and the CD track match requirement.

this distribution is also representative of an inefficiency associated with the reconstruction of CD tracks in the central detector which existed for good beam produced muon tracks. The actual efficiency for reconstructing a good CD track corresponding to a beam produced muon was determined to be on the order of 85%.

- **Dimuon Opening Angle Cut**

A dimuon opening angle cut was also employed to help eliminate cosmic ray events in which the path of a cosmic ray muon through the detector did in fact pass in close proximity to the interaction vertex of an event. The opening angle was calculated between the two leading P_T muons in the event and was based on track fits performed with momentum vectors which were determined exclusively from muon chamber hits. These fits were more

reliable for reconstructing cosmic ray tracks in the detector since no central tracking hits or event vertex information (in the case of three layer tracks) were included in the track reconstruction. The dimuon opening angle angle discussed here was based on the muon momentum vectors outside of the muon toroid which were less influenced by tracking bias towards the interaction region. The normalized dimuon opening angle distribution for $b\bar{b}$ dimuon Monte Carlo events is plotted in Fig. 3-5 for events in which the dimuon invariant mass was calculated to be greater than 6 GeV/c^2. An upper limit on the dimuon opening angle of 165° was chosen to reject a large fraction of cosmic events and minimize the corresponding loss in acceptance for beam produced $b\bar{b}$ events. The fraction of $b\bar{b}$ dimuon events which have an invariant mass above 6 GeV/c^2 and fall below the 165° upper limit on dimuon opening angle was determined from Monte Carlo to be 92%. The second distribution in Fig. 3-5 illustrates the effectiveness of the dimuon opening angle cut on a subset of the cosmic ray data sample in which both of the two leading P_T muons in each event survived the cut on minimum ionizing energy in the calorimeter and the CD track match requirement.

- **MUGTAG Cut**

A software subroutine referred to as MUCTAG [29] was utilized in the analysis to help reject events with muon tracks which were consistent with a cosmic ray muon passing through two opposite sides of the detector. The track reconstruction of each muon candidate determined solely from muon chamber hit information (and the event vertex in the case of two-layer tracks) was pointed into the opposite side of the muon detector in η-ϕ space where a search was performed for another track or hit pattern suggestive of the original track having passed into the opposite side of the detector. A pair of track candidates was considered back to back if $\Delta\phi > 160°$ and $\Delta\eta > 170°$.

In dimuon events which satisfied this condition, both reconstructed tracks were flagged as cosmic candidates. The search for opposite side hits was performed in a window of 60 cm in the bend view and 150 cm in the non-bend view with respect to an extension of the reconstructed muon track direction outside of the iron toroid into the opposite side of the detector. In general, at least three hits had to be found within the search window of a reconstructed track for a muon to be tagged as a cosmic ray candidate. In cases where the MUCTAG subroutine was utilized as an offline cut for cosmic ray rejection, the requirement was made that neither of the two leading P_T muon tracks had been tagged as a cosmic candidate via the subroutine. Since the MUCTAG subroutine was also utilized in the definition of good muon tracks at Level 2, this particular cut could in some cases be redundant offline. The offline MUCTAG requirement had little or no effect on events collected with trigger conditions which required two good tracks at Level 2 since each of these events was constrained to have two muon tracks which satisfied the MUCTAG requirement. In the case of trigger conditions which required only one good muon candidate at Level 2, on the other hand, the offline institution of the MUCTAG requirement proved useful in further reducing the cosmic ray background.

- **Tight Central Detector Track Match**

  A tighter constraint on the match between a muon track and its corresponding Central Detector track was utilized in some studies connected with this analysis to further reduce the relative fraction of background cosmic ray events in the data sample. In these cases the matching CD tracks were required to be within $\Delta\theta \leq 0.16$ radians and $\Delta\varphi \leq 0.12$ radians of the two leading P_T muon tracks.

- **Muon Global Fit**

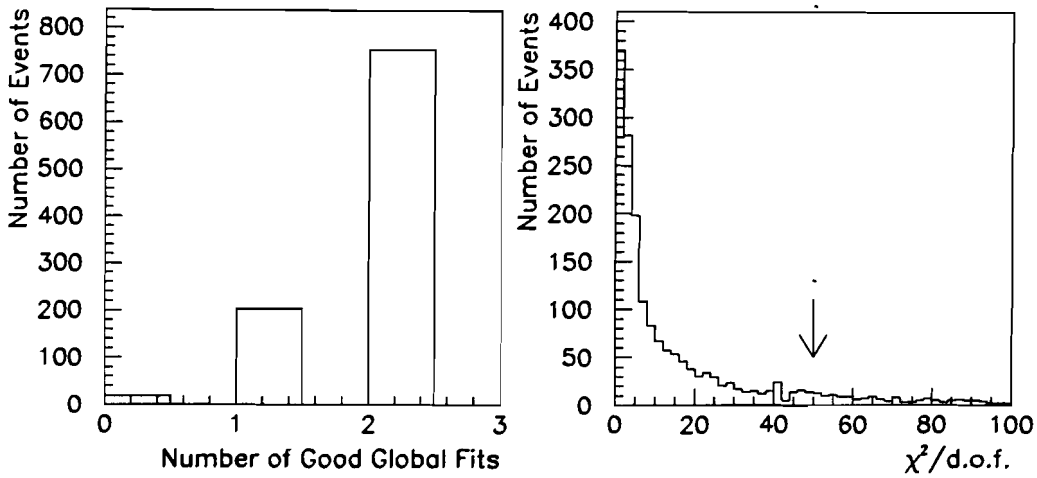

Figure 3-6: (a) Number of good global track fits for the two leading P_T muon tracks in data events which pass all cosmic cuts except for those which involve global track fits and (b) χ^2/d.o.f. of muon tracks in data events which have good global fits and pass all cosmic cuts except for the tight constraint on the global fit quality.

The muon track reconstruction code employed by this analysis included a global muon fit based on hit information from the muon and central tracking systems as well as the reconstructed event vertex. The χ^2/d.o.f. was calculated for each global track fit and utilized as a relative measure of the fit quality. A good global fit was required to contain hit information from both detector systems and include the reconstructed event vertex. The fit quality of a good global fit was required to lie in the range $0 \leq \chi^2/\text{d.o.f.} \leq 100$. The number of good global track fits for the two leading P_T muon tracks in events from the dimuon data stream which pass all cosmic cuts except for those which involve global track fits is shown in the left half of Fig. 3-6.

- **Tight Muon Global Fit**

Title	Loose	Medium	Tight
Minimum Ionizing Energy Confirmation	X	X	X
Central Detector Track Match		X	X
Dimuon Opening Angle Cut	X	X	X
MUGTAG Subroutine		X	X
Tight Central Detector Track Match			X
Muon Global Fit			X
Tight Muon Global Fit			X

Table 3-2: Combinations of cosmic ray cuts used in mixing analysis.

A tighter constraint on the quality of a muon global fit than the one chosen by the reconstruction code was found to be useful in further decreasing the contamination of cosmic ray events in the data sample. Each of the two leading P_T muon tracks was required to have a good global fit with a fit quality required to lie in the range $0 \leq \chi^2/\text{d.o.f.} \leq 50$. The $\chi^2/\text{d.o.f.}$ distribution of muon tracks with good global fits from events in the dimuon data stream which pass all cosmic cuts except for the tight constraint on the global fit quality is shown in the right half of Fig. 3-6.

Several different combinations of the muon selection criteria designed to help eliminate cosmic ray background in the data sample were used in the course of the mixing analysis. One reason for using different sets of cuts was to cross check the effectiveness of the methods which were used to estimate the remaining number of cosmics in the final event sample. Since the topological requirement of a jet or a jet associated with a muon candidate served to substantially reduce the relative fraction of cosmic ray background in an event sample, a smaller combination of the cosmic ray rejection cuts discussed here were required in portions of this analysis where jet cuts were utilized. The three combinations of cosmic ray rejection cuts utilized in this analysis are summarized in Table 3-2.

3.3 Offline Jet Identification

3.3.1 Jet Finding

Jet reconstruction for this analysis was done using a cone algorithm [30]. Jets are defined through the summation of the measured E_T found in calorimeter cells within a cone in η-ϕ space of radius $R = \sqrt{\Delta\eta^2 + \Delta\phi^2} = 0.7$. The jet finding algorithm starts with a list of the measured E_T found in each calorimeter tower. The width of calorimeter towers used in the jet reconstruction algorithms is $\Delta\eta \times \Delta\phi = 0.1 \times 0.1$ except for regions of the calorimeter at very small angles with respect to the beampipe where somewhat wider towers are utilized. Prior to jet reconstruction the measured E_T in each tower is corrected for the position of the interaction vertex as determined from central tracking information.

The initial stage of jet finding is the identification of localized energy deposits known as preclusters which can be used as starting points for the iterative cone algorithm. Each tower with $E_T > 1.0$ GeV forms a precluster in conjunction with any nearest neighbor towers that also lie above the 1.0 GeV E_T threshold. The E_T weighted center of each individual precluster is calculated, and the η-ϕ coordinate of each weighted center is utilized as a starting point for the axis of a $R = 0.7$ jet cone. Once this starting position has been determined, the weighted center of the transverse energy contained in all calorimeter towers within each jet cone is calculated. In cases where the E_T weighted center of all calorimeter towers within the jet cone is found to be identical to that of the original precluster, the jet position is considered stable. Otherwise, the jet axis is moved to the new E_T weighted center and the process continues in an iterative manner. Once a stable position for the jet axis is pinpointed, the total transverse energy within the $R = 0.7$ cone is required to be at least 8 GeV.

The final step in this process is to check for overlap between jets found with

different preclusters. If two jets are seen to overlap, a decision must be made whether to split the jets or merge them into one. The decision is based on the amount of shared E_T between the two jets. If over 50% of the energy in either jet is shared with the other jet, the two objects are merged into one. Otherwise, the shared energy is split between the two jets with the E_T in shared calorimeter towers being awarded to the jet with the closer axis. In cases where two different preclusters produce jets whose axes lie within $\Delta R = 0.1$ of each other, the two objects are assumed to be identical and the jet determined from the smaller precluster is deleted.

3.3.2 Standard Jet Definition

Since jet reconstruction is susceptible to non-beam related sources of noise in the calorimeter, a standardized set of cuts is utilized to eliminate fake jets from the data sample. Sources of noise in the calorimeter include main ring energy deposition, hot calorimeter cells, and cosmic ray bremmstrahlung. The standard set of cuts which describe a good jet consist of the following conditions.

- **.05 < EMfrac < .95** The fraction of jet E_T contained in the electromagnetic section of the calorimeter is constrained to be greater than .05 and less than .95. This cut has been shown to be over 90% effective at removing fake jets associated with hot calorimeter cells [31]. The efficiency of this cut on real jets has been studied using Monte Carlo [32] and shown to be over 99% efficient with the exception of a small region in the crack between the central and end calorimeters where no electromagnetic coverage is present. A slight dip in the cut efficiency is observed in this region which corresponds to $|\eta| \sim 1.4$.

- **CHfrac < 0.4** The fraction of jet E_T in the coarse hadronic section of the calorimeter is constrained to be less than 0.4. This cut is primarily designed

to reject jets which are formed from energy deposits associated with the main ring of the accelerator which is used to produce antiprotons while $p\overline{p}$ collisions are in progress. Since the main ring passes directly through the coarse hadronic section of the calorimeter, it is natural to expect that a large fraction of energy deposition from this source will be deposited in that region. This cut has been determined to be over 95% effective at removing fake jets associated with the main ring and over 99% effective at removing fake jets associated with hot cells in the coarse hadronic region [33]. Monte Carlo studies of this cut [33] have shown it to be over 99% efficient for real jets with the exception of the crack region where it drops to $\sim$ 95% due to missing electromagnetic and fine hadronic section of the calorimeter.

- **Hot Cell Ratio $<$ 10.** The hot cell ratio is defined as the ratio of the E_T associated with the highest E_T cell in a jet to that of the second highest E_T cell. Since real physics processes are unlikely to produce energy deposition in one calorimeter cell which is a factor of ten greater than that for all other cells within a given jet, this cut is very efficient at removing jets due to noisy cells within the calorimeter [31][32].

The net efficiency of these cuts has been studied extensively and found to range between 96% for jets with $E_T = 11$ GeV and 91% for jets with $E_T = 400$ GeV [32]. The overall rejection of "fake" jets from these cuts has been determined to be greater than 95% [31].

Chapter 4

Monte Carlo

4.1 Monte Carlo Samples

4.1.1 $b\bar{b}$ and $c\bar{c}$ Monte Carlo

The most significant production mechanism of dimuon events in the DØ data sample is the decay of heavy quark pairs into muons. Version 7.13 of the ISAJET event simulator [34] was used to model heavy quark pair production, fragmentation of the quark pairs into hadrons, and the subsequent decay of hadrons with lifetimes less than 10^{-12} seconds. A hard scatter from a $p\bar{p}$ collision was generated with the TWOJET utility within ISAJET which simulates all order α_s^2 QCD processes which give rise in lowest order to two high P_T jets. Examples of these processes include $gg \rightarrow gg$, $gq \rightarrow gq$, and $gg \rightarrow q\bar{q}$. The transverse momentum range of the objects resulting from the $2 \rightarrow 2$ scattering processes was chosen to be 4-80 GeV/c for this event generation. An accurate dimuon cross section can be obtained from events generated within this limited transverse range since quarks with $P_T^q < 4$ GeV/c do not produce muons with $P_T^\mu > 3$ GeV/c. CTEQ2L structure functions were utilized in the hard scatter simulation for the majority of events which were generated. Upon completion of the hard scatter, ISAJET makes QCD radiative corrections on the quarks and gluons in the hard scatter to simulate higher order

processes. These corrections include the modeling of $q \rightarrow q + g$, $g \rightarrow g + g$, and $g \rightarrow q + \bar{q}$.

The generation of a hard scatter process in conjunction with the QCD radiative corrections results in the simulation of both the leading and higher order production mechanisms of heavy quark pairs. The leading order processes which include quark and gluon fusion are often referred to as flavor creation processes. Next-to-leading order (α_s^3) processes are also expected to make a significant contribution to the production of heavy quark pairs at Tevatron energies. In fact, the inclusive b quark cross section at $\sqrt{s} = 1.8$ TeV is expected to have a next-to-leading order contribution which is a factor of two above the leading order contribution [35]. Due to the contrasting event structure associated with different types of next-to-leading order processes, the α_s^3 processes are usually artificially separated into two categories. The production of a heavy quark pair through the decay of a gluon produced in the hard scattering is referred to as a gluon splitting process. A flavor excitation process, on the other hand, results from the splitting of an intial state gluon into a heavy quark pair where one of the heavy quarks is subsequently scattered by another parton within the proton or antiproton. Examples of Feynman diagrams for both the leading and next-to-leading order processes are illustrated in Fig. 4-1.

That one expects a significant contribution to heavy quark cross sections from next-to-leading order processes can be demonstrated using $b\bar{b}$ pair production as an example. The cross section for $gg \rightarrow gg$ is on order of a hundred times greater than the cross section for $gg \rightarrow b\bar{b}$. Therefore, even though the fragmentation of a gluon into a $b\bar{b}$ pair has only about a 1% probability, the total cross section for the next-to-leading order processes is on the same order as those for the leading order processes.

In ISAJET the hadronization of heavy quarks is described by phenomenological

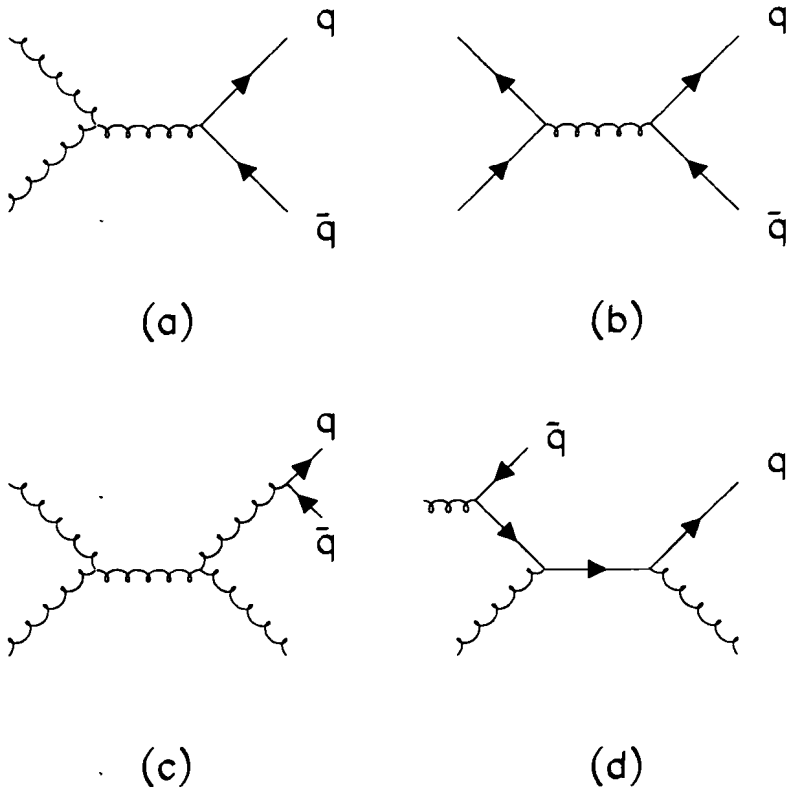

Figure 4-1: Examples of Feynman diagrams for heavy quark production in $p\overline{p}$ collisions. Leading order (α_s^2) processes are (a) gluon fusion and (b) quark fusion, collectively referred to as flavor creation. Next-to-leading order (α_s^3) processes are (c) gluon splitting and (d) flavor excitation.

fragmentation functions of the form

$$D_Q^H(z) = \frac{N}{z[1 - \frac{1}{z} - \frac{\epsilon}{1-z}]^2}. \tag{4.1}$$

$D_Q^H(z)$ is defined as the probability that a heavy quark Q will fragment to a hadron H with fractional momentum z. The variable z is defined as $(E^H + P_{||}^H)/(E^Q + P^Q)$ where $P_{||}^H$ is the momentum component of the hadron parallel to the quark momentum direction. The factor of N in (4.1) is utilized to normalize the total probability for hadronization to one. The Peterson parameter ϵ has a rough $1/M_Q^2$ dependence on quark mass. The event generation discussed here used the ISAJET default values of $\epsilon_b = 0.02$ and $\epsilon_c = 0.31$ for b and c quarks respectively. Smaller values of ϵ lead to larger values of $< z >$ which means that the resulting hadrons maintain a larger fraction of parent quark momentum. The relatively hard fragmentation of the b quark favors the detection of high P_T leptons resulting from subsequent semileptonic decay compared to similarly produced leptons from c quarks. The decay of hadrons in ISAJET is controlled using a table of potential decay modes for each hadron. A random number generator is utilized to select decay channels based on the relative branching fractions assigned to each specific mode.

The simulation process described above is extremely time consuming due to the fact that the fraction of hard scatters which results in the production of heavy quark flavor is small. A routine known as ISALEP was utilized to help speed up event generation. The first technique which ISALEP uses to speed event generation is multiple evolutions of the QCD radiative corrections for each hard scatter. Since the α_s^3 production of heavy quark pairs depends on relatively small probability radiative QCD processes, this method is especially useful for speeding up the production of next-to-leading order events. Additional event generation speed is obtained with multiple evolutions of the quark fragmentation and hadron decay

for events which are found to contain heavy quark pairs. Since the hadrons which result from heavy quark fragmentation have a probability for decaying into muons on order of 10-20%, the chance of a single evolution producing a dimuon event is less than 5%. Multiple evolutions of the quark fragmentation and subsequent decay make it much more likely that a dimuon event can be obtained from the original hard scatter. The parameters of the ISALEP routine which determine the number of event evolutions which are performed at each of the stages described above are referred to as NEVOLVE and NHADRON. These parameters were both set to ten in the event generation described here in order to increase event acceptance from the initial hard scatter without significantly increasing the probability for producing multiple events from one hard scatter.

In order to provide an accurate description of the kinematic properties associated with dimuon events produced in the decay of $b\bar{b}$ and $c\bar{c}$ quark pairs, a complete model of quark fragmentation and hadron decay such as that provided in the ISALEP routines was required. However, the inclusive b quark production cross section which was utilized in the ISALEP event simulation package was found to disagree in both magnitude and shape with recent measurements of the same cross section at $\sqrt{s} = 1.8$ TeV [36][37]. Therefore, the cross sectional weight assigned to each dimuon event generated with the ISALEP simulation package needed to be corrected based on the difference between the predicted and measured production cross sections for the heavy quark pairs in these events.

Since the shape of the b quark production cross section obtained from next-to-leading order perturbative QCD calculations of Nason, Dawson, and Ellis [38] was found to be in close agreement with the shape obtained from experimental measurements, the heavy quark cross sections obtained from these calculations were utilized to normalize the heavy quark production cross sections in ISALEP. In order to perform this normalization the shape of the inclusive b and c quark

cross sections in ISALEP had to be determined from heavy quark event samples generated without muon requirements. In the course of generating these samples, however, it was found that the shape of the inclusive heavy quark cross sections obtained from ISALEP varied as a function of the input values for NEVOLVE and NHADRON. Furthermore, the inclusive muon cross sections which were obtained from ISALEP events generated with muon requirements were also found to be dependent on these input values, but in a manner which was not consistent with that found for the inclusive heavy quark cross sections. In other words, the ratio of the differential heavy quark cross section underlying generated dimuon events to the total heavy quark cross section varied for given sets of NEVOLVE and NHADRON.

Therefore, in order to correct the cross sectional weights of ISALEP generated dimuon events such that the underlying heavy quark cross section section of these events was consistent with that from the NDE calculations, a two step correction was necessary. First, the underlying heavy quark cross section for single muon events generated with the ISALEP parameters NEVOLVE and NHADRON set equal to 10 was normalized to that for muon events generated with those parameters set equal to 1. This normalization resulted in identical inclusive muon cross sections for both samples. Next, the total heavy quark cross section for ISALEP generation of heavy quarks with NEVOLVE and NHADRON set equal to 1 was normalized to that from NDE. The correction factor applied to the dimuon ISALEP sample generated with NEVOLVE and NHADRON set equal to 10 was given as the product of the correction factors. The correction factor applied to each event is a function of the heavy quark P_T which was taken as the average value of the generated quark and antiquark in all cases. Note we have assumed here that the correction factor determined using the inclusive muon sample is identical to that for dimuons. Independent correction factors were determined for events produced

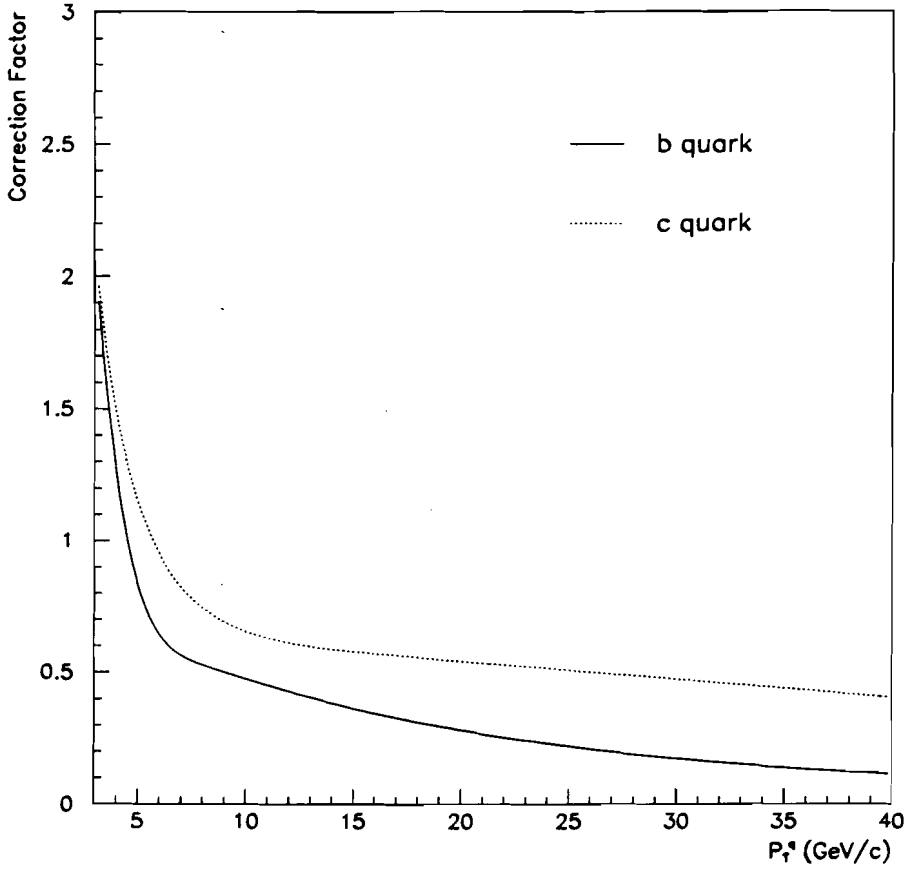

Figure 4-2: Correction factors for b and c quark production cross sections plotted as a function of the heavy quark P_T. The correction factors are applied to match the heavy quark cross sections obtained from ISALEP to the NLO calculations of Nason, Dawson, and Ellis.

in the decay of $b\bar{b}$ pairs and for those produced in the decay of $c\bar{c}$ pairs. The forms of these correction factors as a function of P_T^q are shown in Fig. 4-2.

4.1.2 Drell-Yan Monte Carlo

Drell-Yan production of dimuon events in the DØ detector was also modeled using the ISAJET event simulator. The DRELLYAN utility within ISAJET models the hard scattering process of $q\bar{q} \rightarrow \gamma^* \rightarrow \mu^+\mu^-$. The leading order process results in the production of dimuon pairs with zero transverse momentum excepting for the Fermi motion of the quarks. QCD radiative corrections applied to the original hard scatter result in the simulation of next-to-leading order processes in which the dimuon transverse momentum is non-zero. The resulting next-to-leading processes are of the form $q\bar{q} \rightarrow \gamma^* g \rightarrow \mu^+\mu^- g$ and $qg \rightarrow \gamma^* q \rightarrow \mu^+\mu^- q$. Since the next-to-leading order calculation of the Drell-Yan cross section has a $1/P_T^2$ dependence which results in the prediction of an infinite cross section as $P_T \rightarrow 0$, ISAJET replaces the $1/P_T^2$ term with a cutoff parameterization designed to produce the correct integrated cross section. This parameterization is

$$\frac{1}{P_T^2} \rightarrow \frac{1}{\sqrt{P_T^4 + P_0^4}} \tag{4.2}$$

where P_0^2 is defined as (0.2 GeV) M_{γ^*}.

The Drell-Yan Monte Carlo event sample utilized in this analysis was generated using EHLQ structure functions. In addition, the mass range of the γ^* was restricted to the region between 4-40 GeV/c^2. Since the inclusive Drell-Yan cross section has been measured at $\sqrt{s} = 1.8$ TeV using dimuon events collected with the DØ detector [39], the cross sectional weight of the events in the Drell-Yan Monte Carlo sample could be modified to match the measured cross section from the data. Independent correction factors were determined for five separate dimuon invariant mass bins corresponding to different mass bins of the γ^*. Since the orig-

inal ISAJET prediction for the Drell-Yan cross section was found to be in good agreement with the measured cross section from the data, within 35% in each of the invariant mass bins, the magnitude of these corrections was small.

4.1.3 Decay Background Monte Carlo

A significant muon background is expected from decays of charged pions and kaons in the central tracking region of the detector. The cross section for charged particle production in $p\bar{p}$ collisions at $\sqrt{s} = 1.8$ TeV has been measured and found to be substantial [40]. Since the decay length of charged particles is boosted in the lab frame by a factor which increases with particle momentum, the fraction of charged particles which decay in the 0.84 m radius of the DØ central tracking volume is small. Also, since the average transverse momentum of muons produced in the decays of charged pions and kaons is on the order of 0.5 GeV/c, an additional reduction in this fraction is obtained from the 3 GeV/c lower transverse momentum limit on the muon candidates utilized in this analysis. However, the branching fractions for the decay of charged pions and kaons into muons are large, and the resulting muon background from charged particle decay is non-negligible.

An important background to dimuon production from heavy quark pairs are dimuon events in which a single prompt muon is produced in the decay of a heavy quark and a second muon is produced in the decay of a charged pion or kaon. In addition, the decay of two charged pions or kaons within a single event can also result in the production of a dimuon pair.

A Monte Carlo event generator was written to determine the relative magnitude of these background processes. The cross sections which were obtained from this event simulation package for each of the dimuon production mechanisms in which at least one muon is produced in the decay of a charged pion or kaon are shown in Table 4-1. These cross sections are for dimuon events in which both muons are

Production Process	Dimuon Cross Section	Relative Magnitude
$b \rightarrow \mu^-$, $\pi/K \rightarrow \mu$	$2.85 \times 10^{-5} \mu$b	3.2
$c \rightarrow \mu^+$; $\pi/K \rightarrow \mu$	$1.94 \times 10^{-5} \mu$b	2.2
$\pi/K \rightarrow \mu$, $\pi/K \rightarrow \mu$	$9.02 \times 10^{-6} \mu$b	1.0

Table 4-1: Event generator level cross sections for dimuon events from background production mechanisms involving muons produced in the decay of charged pions and kaons. The dimuon cross sections are based on the following criteria: $|\eta_\mu| < 0.8$, 4 GeV/c $< P_T^\mu <$ 25 GeV/c, 6 GeV/c^2 $< M_{\mu\mu} <$ 35 GeV/c^2, and dimuon opening angle less than 165°.

found in the pseudorapidity range $|\eta_\mu| < 0.8$ and the transverse momentum range 4 GeV/c $< P_T^\mu <$ 25 GeV/c. The dimuon invariant mass and opening angle ranges represented in these cross sections are also limited. The dimuon invariant mass is restricted to the region 6 GeV/c^2 $< M_{\mu\mu} <$ 35 GeV/c^2 and the dimuon opening angle is required to be less than 165°.

Since the background contribution of dimuon events in which both muons are produced in the decay of charged pions or kaons (double decay events) was found to be more than a factor of two smaller than the individual contributions from each of the prompt plus decay processes, full Monte Carlo event simulation of dimuon background processes involving muons produced in the decay of charged pions and kaons was limited to prompt plus decay events. In order to determine the relative contribution of double decay events to the final data sample, the assumption was made that the relative contribution of double decay events to the final data sample was a factor of 2.2 lower than the contribution of events in which one muon is produced in the decay of a c quark and the other is produced in the decay of a charged pion or kaon. This assumption is based on the idea that the relative contribution of events associated with each of these processes at the event generator level can be expected to match the relative contribution after full simulation since the important kinematic cuts have been applied to both. In order for this assumption

to be valid, the detector and selection criteria acceptances for events from each of these production mechanisms must be roughly equivalent. Since the kinematic properties of muons produced in c quark decay are similar to those for muons produced in the decay of charged pions and kaons, this requirement is satisfied.

A special decay package was utilized to speed production of prompt plus decay Monte Carlo. A sample of single muon events resulting from heavy quark pair production was generated with ISAJET utilizing the ISALEP modifications discussed in Section 4.1.1. Each event in the sample was input into the decay simulator which compiled a list of all decay candidates ($\pi^{\pm}$,$K^{\pm}$, and K_L^0) in the event for which $P_T^{\pi/K} > 3.0$ GeV/c and $|\eta^{\pi/K}| < 0.9$. A single particle was randomly selected from this list and forced to decay into a muon within the radius of the central tracking volume. The probability for such a decay to occur can be expressed as

$$P = \left(1 - e^{-\frac{R_{CD}}{c\tau}\frac{m_{\pi/K}}{E^{\pi/K}}}\right) BR(\pi/K \rightarrow \mu) \tag{4.3}$$

where R_{CD} is the cylindrical radius of the central tracking volume, $c\tau$ is the particle decay length, and $BR(\pi/K \rightarrow \mu)$ is the appropriate branching fraction to muons. The specific decay modes which were included in the decay package are $\pi^+ \rightarrow \mu^+\nu_\mu$, $K^+ \rightarrow \mu^+\nu_\mu$, $K^+ \rightarrow \pi^0\mu^+\nu_\mu$, and $K_L \rightarrow \pi^{\pm}\mu^{\mp}\nu$ as well as the corresponding charge conjugate modes.

The cross sectional weight assigned to Monte Carlo events produced with the decay package was calculated as the product of the original cross section weight of the single muon event with the probability for producing a muon from a pion or kaon decay within the event. Even though the decay package selected only one particle to decay from the original candidate list, each of the candidates in the list had some probability for producing an additional muon in the event. Therefore, if there were N particles on the original decay list, the correct cross section can be

expressed as

$$W = W' \times \sum_{i=1}^{N} P_i \tag{4.4}$$

where W' is the cross section of the single muon event and the P_i are the individual decay probabilities associated with each candidate.

The decay package discussed here utilized a simple approximation of the above expression in assigning a cross sectional weight to individual events. If all of the particles on the decay candidate list are assumed to have equivalent decay probabilities, the event cross section becomes

$$W = W' N P_x \tag{4.5}$$

where P_x is defined to be the decay probability of the specific candidate which was picked to decay.

This assumption was not necessarily valid on a single event basis since different specific types of decay candidates have unique decay probabilities which also differ as a function of the candidate transverse momentum. However, the cross section for a large sample of events weighted with the above method would in fact be accurate since each of the different specific decay candidates will be chosen numerous times as the actual candidate for decay. Specific events which are assigned an excess cross section due to the selection of a decay candidate with a higher than average decay probability will be averaged against events in which decay candidates with lower than average decay probabilities were selected.

The decay package described above was checked against a calculation of the single muon cross section expected from π and K decays based on the charged particle cross section measured by CDF [41]. The input to the decay package for this test was unbiased ISAJET events generated with the TWOJET utility where the objects resulting from the hard scatter were restricted to a transverse

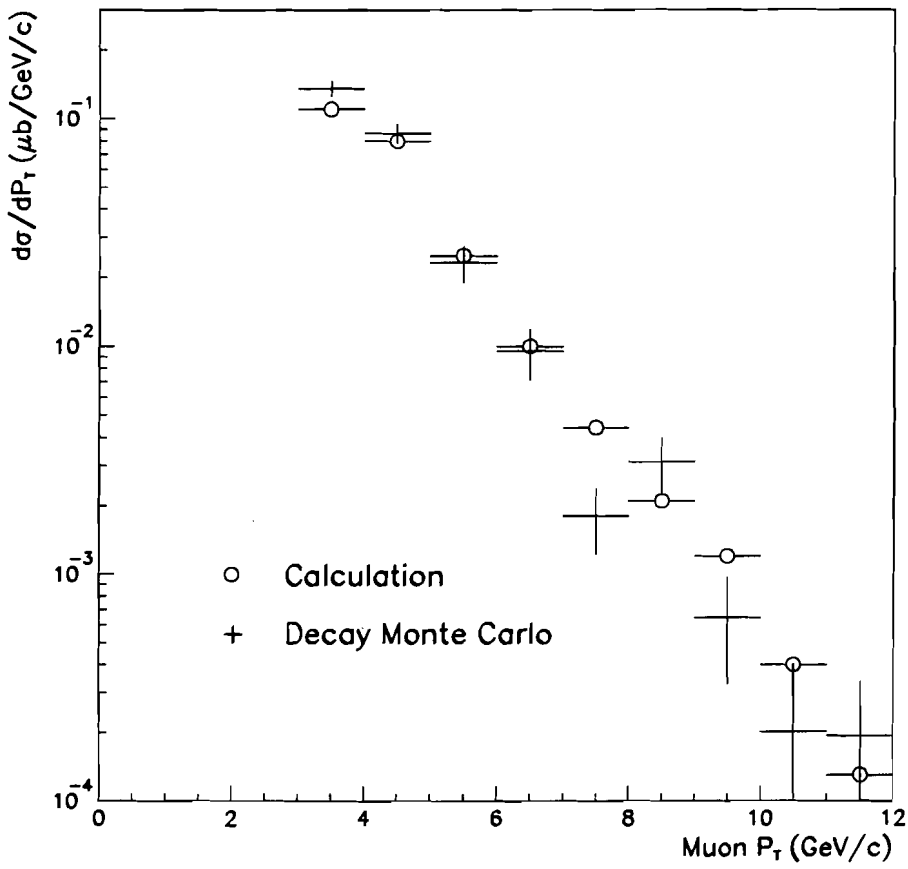

Figure 4-3: Comparison of inclusive single muon cross section from π and K decay obtained from decay package utilized in this analysis with calculation based on charged particle cross section measured by the CDF experiment.

momentum range of 3-100 GeV/c. One particle from the resulting candidate list was forced to decay into a muon within the tracking volume and an event weight was assigned in accordance with (4.5). A comparison of the single muon cross section from π and K decay as determined from the decay package used in this analysis with the calculation mentioned above is shown in Fig. 4-3. The illustrated agreement between the two methods suggests that the prompt plus decay cross sections which were obtained with the identical decay package are similarly valid.

4.2 Muons in Data and Monte Carlo

The reconstruction efficiency of muon tracks in the DØ detector can be determined from a knowledge of the geometry of the muon chambers and their efficiencies for producing usable hit information in the individual chamber cells which are traversed along a muon track. The muon track reconstruction program requires hit information in at least two out of the three layers of muon chambers in addition to a minimum number of combined hits along the muon track. The Monte Carlo can be relied upon to give an accurate description of the effects of detector geometry on muon reconstruction efficiency including the probability that low momentum muons range out in the 13-15 interaction lengths of detector material between the interaction region and the outer muon chambers. However, the standard DØ Monte Carlo has been found to be inadequate at describing the efficiencies for producing good hit information in each of the individual cells within the muon system which are observed in the data.

The discrepancy in muon chamber hit efficiency between data and Monte Carlo is thought to be due to several factors. One factor is the effect of several different sources of particle backgrounds in the DØ collision hall which are not included the Monte Carlo simulations. As discussed in Section 2.1 one particular source of background hits in the DØ muon system is the main ring which is used to produce

new batches of antiprotons while $p\bar{p}$ collisions are in progress. Since the main ring passes directly through the upper portion of the DØ detector, the background radiation from this ring had a significant effect on the efficiencies of the muon chambers in this region over the course of the run. In particular, the radiation associated with particles in the main ring caused high voltage sagging in the muon chambers in the upper region of the detector. The time required for the high voltage to recover from these particle blasts had a large effect on the efficiencies of the chambers in this region.

Additional particle backgrounds associated with showers initiated by particle collisions with beam line elements and detector edges also affected the muon chamber performance. Outgassing of the glasteel material on which the muon chamber pads were etched in conjunction with the large particle rates in the chambers caused the high voltage wires in the muon cells to become coated with a foreign substance during the course of the run. The decreased field around the wires led to additional inefficiency in the chambers associated with this radiation damage. This aging process affected some chambers more than others which meant that corrections for this effect had to be made for each individual chamber.

The DØ muon group did a large amount of work to measure the hit efficiencies and hit resolution of each muon chamber in the detector using a large sample of muon tracks collected from events in the data stream [42]. The method used to determine chamber efficiency was to count the number of muon cells along each track which did not register a hit. The measured fraction of cells which do produce hits also needed to be corrected for the bias in the number of good hits along muon tracks which produce triggers in order to extract the actual chamber efficiencies. The chamber hit resolutions were extracted by measuring the difference between the hit position in an individual cell and the position of the reconstructed track in that cell. The net result of these studies was the creation of the MUSMEAR

software package which can be run on Monte Carlo events to modify the muon hit banks in these events to match the real hit efficiencies and hit resolutions which were measured from the data.

In order to check the effectiveness of the MUSMEAR correction routine for reproducing tracks in our data sample, a comparison was made between the Level 1 trigger efficiency for muon tracks in our data sample and the same efficiency for tracks in a corrected Monte Carlo sample. The Monte Carlo sample was constructed from the three dimuon event samples discussed in Section 4.1 where the relative contribution of each event to the combined sample was based on its assigned cross sectional weight. The comparison was performed using dimuon events which passed either the Mu-1-Jet or Mu-Jet-Low trigger requirements. Since each of these triggering conditions required only one muon, it was possible to make an unbiased determination of the efficiency for triggering on the additional muon in the event. Three kinematic cuts were made on the dimuon events to be consistent with cuts utilized in the mixing analysis. The transverse momentum of each muon track was required to be above 4 GeV/c, the dimuon invariant mass was restricted to the region 6 GeV/c^2 $< M_{\mu\mu} <$ 35 GeV/c^2, and each muon was required to have an associated reconstructed jet with $E_T^{jet} > 12$ GeV. In addition, the loose set of cosmic cuts as defined in Table 3-2 were applied to the muon tracks in the data sample to reduce the background from cosmic ray events. A fit done to the floating t_o distribution for the muon tracks in the data sample (see Section 5.4.1) after these cuts were made indicated that less than 5% of the remaining events were due to cosmic background.

The central region of the DØ muon system is divided into octants for the purposes of triggering at the hardware level, and the trigger information from each of the eight octants is recorded in the data stream. For each of the reconstructed muons in our dimuon sample, the octant in which the muon track was found was

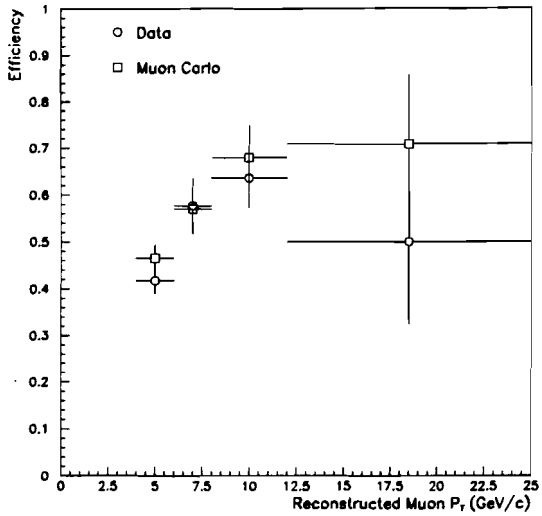

Figure 4-4: The efficiency for finding a Level 1 muon trigger associated with both reconstructed muon tracks in dimuon events which pass the requirements of at least one of the single muon plus jet triggers utilized in this analysis. The efficiency is plotted in terms of the reconstructed P_T of the trailing muon in the event.

checked for a corresponding Level 1 trigger. The measured efficiency was defined as the number of events where both of the reconstructed muons in the event had matching Level 1 information divided by the total number of events in the sample. A comparison of this efficiency for events in the data and Monte Carlo samples is shown in Fig. 4-4. The efficiency is plotted as a function of the reconstructed P_T of the trailing muon in the event since the leading P_T muon was assumed to have provided the necessary muon trigger requirement for events in the sample. The illustrated agreement in this efficiency between data and Monte Carlo suggests that the chamber efficiencies contained within the MUSMEAR package are an accurate representation of the actual detector efficiencies. Events with muons in the fiducial region where $80° < \phi < 110°$ were not included in this comparison due to the low chamber efficiencies in this region due to radiation damage from the main ring in the DØ collision hall.

4.3 Jets in Data and Monte Carlo

The method chosen to test the effectiveness of ISAJET at describing jets found in the data was to make a comparison of jets in the dimuon data sample collected with the Mu-2-High trigger bit with those from an equivalent Monte Carlo sample. Since there is no jet requirement in the Mu-2-High trigger bit, the reconstructed jets found in these events were unbiased with respect to the calorimeter trigger. The Monte Carlo sample was constructed from the three dimuon event samples discussed in Section 4.1 where the relative contribution of each event to the combined sample was based on its assigned cross sectional weight. In order to be consistent with kinematic cuts utilized in the mixing analysis the muon tracks within each event were required to have a transverse momentum above 4 GeV/c and the dimuon invariant mass of each event was restricted to the region where 6 GeV/c^2 $< M_{\mu\mu} <$ 35 GeV/c^2. Also, the medium set of cosmic cuts as defined in Table 3-2 were applied to the muon tracks in the data sample to reduce the background from cosmic ray events. A fit done to the floating t_o distribution of the muon tracks (see Section 5.4.1) in events which passed these cuts indicated that approximately 4% of the remaining events were due to cosmic rays.

As an initial check to see how well the Monte Carlo sample reproduces jet features seen in the data, a comparison was made between the distributions for the number of jets and the number of associated jets per event as seen in the data and Monte Carlo. A jet was defined to be associated with a muon track if the jet axis was found within a $\Delta R = 0.8$ search cone around the track. This comparison was made for jets in the pseudorapidity region $|\eta_{jet}| < 1.2$ in order to be consistent with the region utilized in this analysis since different regions of the DØ calorimeter have different characteristics. In addition, each event utilized in this comparison was required to have at least one muon track with an associated jet. This requirement served to significantly reduce the relative number of dimuon

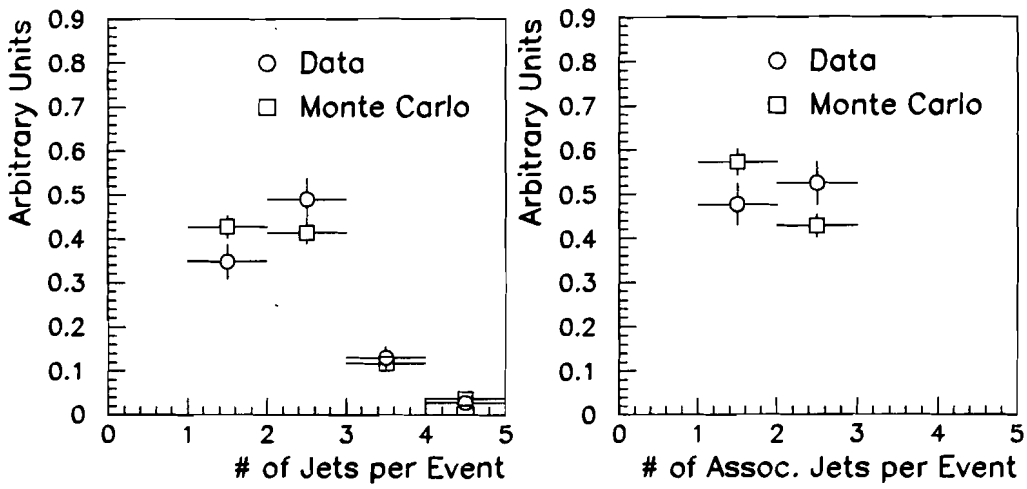

Figure 4-5: Comparison of (a) number of jets per event and (b) number of associated jets per event in dimuon data and Monte Carlo.

events from both Υ decays and Drell-Yan processes in the Monte Carlo and data samples used in this comparison. The resulting distributions for data and Monte Carlo are shown in Fig. 4-5 and demonstrate good agreement within the statistical errors of the samples. Since the number of jets in a given dimuon event is dependent on the production mechanism of the event, the demonstrated agreement in these distributions helps to corroborate the relative contributions of the different dimuon production processes in the Monte Carlo sample.

Another important check on the effectiveness of the Monte Carlo sample at describing jets seen in the data was the comparison of the pseudorapidity distribution of jets in the data and Monte Carlo. As mentioned the DØ calorimeter has unique characteristics in different pseudorapidity regions of the detector. In the region where $|\eta_{jet}| < 0.8$ the particles within a jet pass nearly exclusively through the central calorimeter which has very uniform coverage in three dimensions. However, in the pseudorapidity region $0.8 < |\eta_{jet}| < 1.2$ jet particles pass through the crack

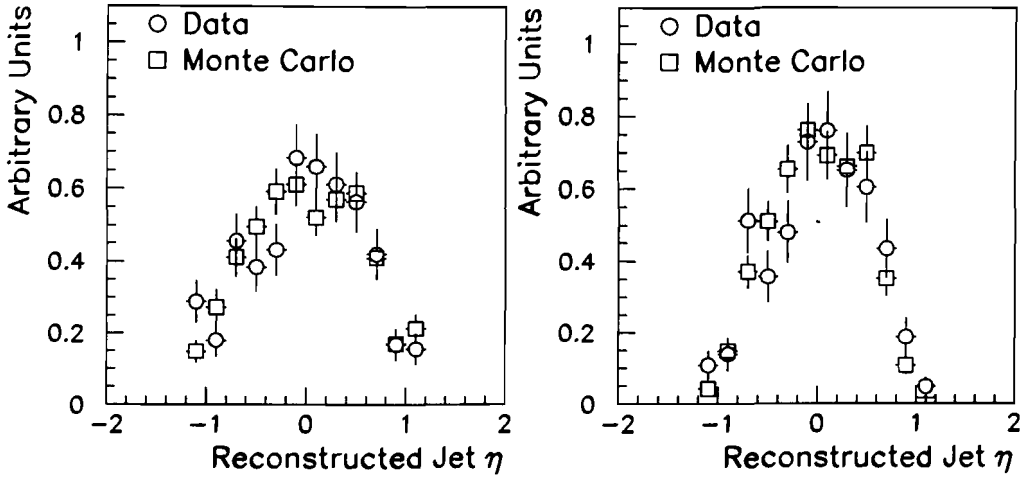

Figure 4-6: Comparison of pseudorapidity spectrum for (a) all jets and (b) jets associated with muons in dimuon data and Monte Carlo.

between the central and end calorimeter modules. As discussed in Section 2.3 scintillation detectors are utilized in this region to help measure the amount of jet energy lost in the crack which adds an additional level of complication to the Monte Carlo modeling of the detector in this region.

An excess or surplus of jets in a certain pseudorapidity region of the detector would suggest an inadequate Monte Carlo model for the jets in that region. As shown in Fig. 4-6, however, the pseudorapidity distributions for all jets and for jets associated with muons in the data and Monte Carlo event samples do in fact agree within the statistical errors of the samples. This agreement serves to further validate the Monte Carlo model of the calorimeter hardware in the different pseudorapidity regions of the detector, and it also helps to confirm the Monte Carlo modeling of the kinematic parameters associated with the jets in the dimuon event sample.

4.3.1 Jet E_T scale in Data and Monte Carlo

It is important to note that the comparisons made in the previous section depend critically on the equivalence of the jet E_T scales in the data and Monte Carlo. Since the definition of a jet used in this analysis includes a lower limit on the transverse energy of a jet ($E_T^{jet} > 12$ GeV), the agreement shown in the previous section would be invalid if the jet E_T scale in the Monte Carlo was not equivalent to that found in the data. A large amount of work has been done within the DØ calorimeter group to produce energy correction routines for reconstructed jets in both the data and Monte Carlo. The result of these efforts is the CAFIX software package [27] which is run on both data and Monte Carlo subsequent to event reconstruction to correct the energy scale of reconstructed jets. The jet energy correction routine for the data accounts for all known performance characteristics of the DØ calorimeter and incorporates information from a large series of test beam runs done on different components of the calorimeter. The energy correction routines for jets in the Monte Carlo, on the other hand, were developed to match the jet energy scale in the Monte Carlo with that found in the data, and several different correction schemes have been created for this purpose.

In the case of this analysis, a correction routine developed by the top quark analysis group for jets with a cone size of $\Delta R = 0.7$ was chosen. The effectiveness of these correction routines can be checked by comparing the distribution of jet E_T in the data and Monte Carlo utilizing the dimuon event sample discussed in the previous section. This comparison is shown in Fig. 4-7 for all jets found in these events and for those jets associated with muons. In general, the shape of the jet E_T spectrum exhibits good agreement between data and Monte Carlo. The jet spectrum obtained from the data sample does have a slight deficiency of jets in the lowest E_T bins which is most likely indicative of small differences in the jet reconstruction efficiency for low E_T jets in the data and Monte Carlo.

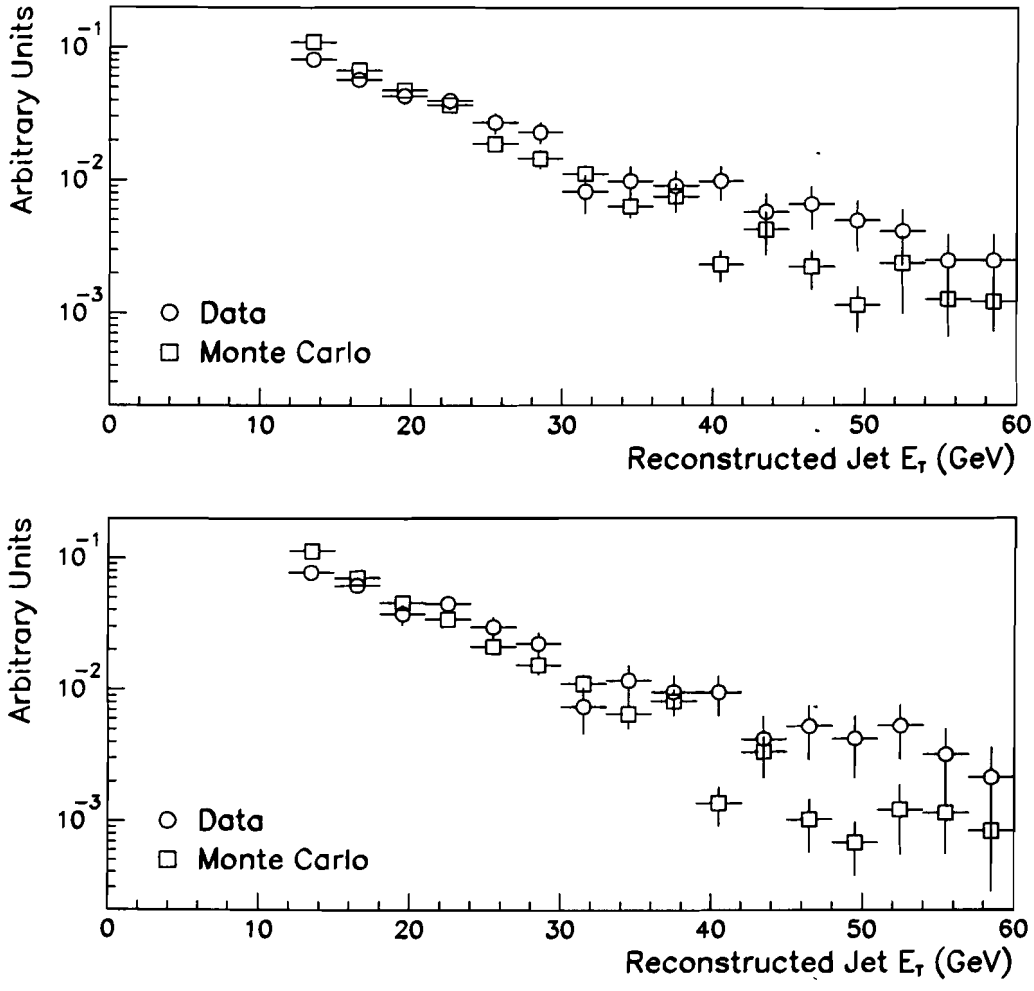

Figure 4-7: Comparison of jet E_T spectrum for (a) all jets and (b) jets associated with muons in dimuon data and Monte Carlo.

4.3.2 Level 1 Jet Trigger Efficiency

Once the correspondence of the jet E_T scale between the data and Monte Carlo had been established, the next step was to compare the jet trigger efficiency which results from running the full DØ trigger simulator on Monte Carlo with that seen in the data. As before the jets used to make this comparison were taken from the dimuon event sample obtained with the Mu-2-High trigger bit to ensure that the jets were completely unbiased with respect to the jet trigger. For each reconstructed jet found in this subset of events a search was performed in a $\Delta R = 0.5$ cone around the jet axis for associated calorimeter trigger towers. If an associated trigger tower was found within the search cone, the reconstructed jet was identified as having passed the Level 1 jet requirement. A threshold on the trigger tower of 3 GeV was chosen to match the Level 1 trigger requirement for jets in the triggering conditions used in the mixing analysis. The resulting Level 1 jet trigger efficiency curves as a function of reconstructed jet E_T are shown in Fig. 4-8 for all jets in the dimuon event sample and for those jets associated with muons. Since a large percentage of jets associated with muon tracks in the sample are produced in the decay of a b or c quark, the trigger efficiency curve shown for associated jets is most indicative of the trigger efficiency for jets which originate from the decay of a heavy quark. The trigger efficiency curve shown for all jets, on the other hand, is indicative of a more convoluted efficiency for heavy quark, light quark, and gluon jets.

The comparison of the Level 1 jet trigger efficiency curves shows that a definite discrepancy exists between the data and Monte Carlo in the structure of the turn on to full efficiency at low jet E_T. The jet trigger information associated with unbiased jets in the data indicates that the full trigger simulator overestimates the Level 1 trigger efficiency of low E_T jets. In particular, the minimum E_T^{jet} required for 100% trigger efficiency is substantially lower in the Monte Carlo than the data would

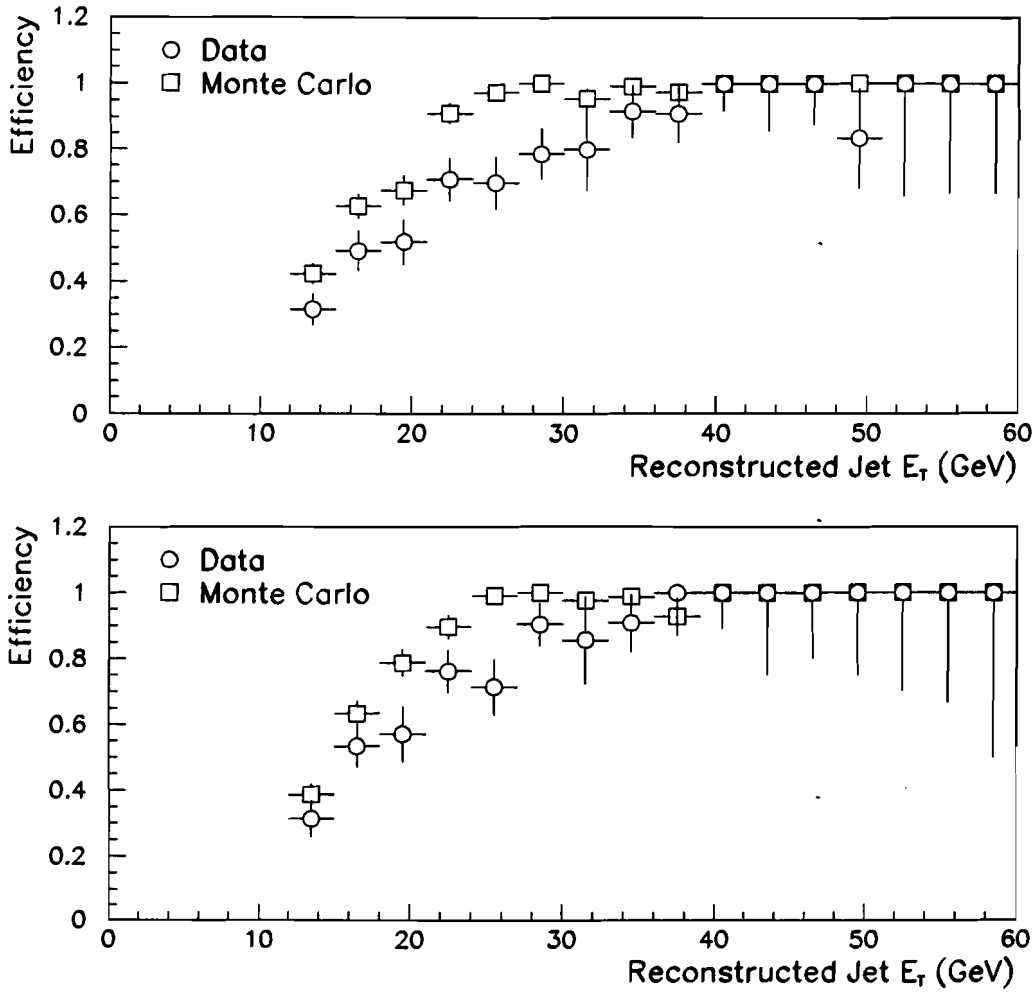

Figure 4-8: Comparison of Level 1 jet trigger efficiency as a function of reconstructed jet E_T for (a) all jets and (b) jets associated with muons in dimuon data and Monte Carlo.

indicate. Since the DØ trigger simulation package works at the level of energy in hit cells rather than with reconstructed jet energy, the correction of the jet energy scale via CAFIX has no net effect on the trigger simulation Monte Carlo events. The DØ trigger simulation package does make some energy scale modifications for its own purposes such as the addition of noise to the trigger input energies, but there is no direct correlation between these modifications and the modification of the jet energy scale via CAFIX. Therefore, the observed discrepancy in jet trigger efficiency between data and Monte Carlo necessitates an additional modification of the trigger simulation for Monte Carlo events at the analysis level.

In addition to the dimuon event sample in the data, an additional sample of unbiased jets in the data was available from special runs taken with a single muon trigger. Since the production mechanisms for single muon events are very similar to those for dimuon events, the jet structures found in these samples are expected to be roughly equivalent. It was therefore useful to check if the larger statistical sample of jets in this sample could be utilized in comparisons of jet trigger efficiency in data and Monte Carlo.

A comparison of the Level 1 trigger efficiency for jets in the single muon event sample and dimuon event sample is shown in Fig. 4-9 for all jets in these events and for those jets associated with muons. The single muon track in these events was required to have a transverse momentum above 4 GeV/c and pass each of the requirements associated with the medium set of cosmic cuts as defined in Table 3-2 which could be applied to a single muon track in order to reduce the cosmic ray background. Since the Level 1 trigger efficiency curves obtained from the single and dimuon data samples agreed within the statistical uncertainty of the two samples, a combined sample of jets from both data sets was utilized in the development of the correction scheme for the jet trigger information in Monte Carlo events. The agreement shown here also provides an important cross check of the jet trigger

efficiency obtained from the dimuon event sample utilized in this analysis against a completely independent data set.

As indicated in the comparison between data and Monte Carlo in Fig. 4-8, the Monte Carlo efficiency for producing a jet trigger at Level 1 was exaggerated with respect to the real efficiency as measured from the data. The direction of this discrepancy suggested that the Monte Carlo simulated energy deposition within calorimeter cells associated with a jet was too high compared to the actual energy deposition associated with an equivalent jet in the data. If this excess energy deposition in the Monte Carlo had been found to be constant with respect to the modeled energy within each cell or to scale as a constant factor of the modeled energy, a simple correction scheme for the Monte Carlo in which the energy deposition threshold for the individual calorimeter cells required to produce a good Level 1 trigger was similarly increased could have been utilized. However, it was discovered that a more complicated correction in which the Monte Carlo trigger tower threshold was allowed to vary as a function of the reconstructed jet E_T was necessary to obtain agreement with the data. A plot showing the Monte Carlo trigger tower energy deposition threshold required to match the trigger efficiency given by the 3.0 GeV threshold in the data is shown in Fig. 4-10 as a function of the reconstructed jet E_T.

The modification of the energy deposition thresholds for the Monte Carlo calorimeter trigger towers was done independently for each of the distinct pseudorapidity regions of the DØ calorimeter utilized in this analysis. As previously mentioned, scintillators are utilized in the pseudorapidity region where $0.8 < |\eta| < 1.2$ to help measure the amount of energy deposition in the crack region between the central and endcap calorimeter modules. Since differences existed in the modeling and detection of jets in each of the distinct pseudorapidity regions, it was necessary to apply separate modifications to the energy deposition thresholds of

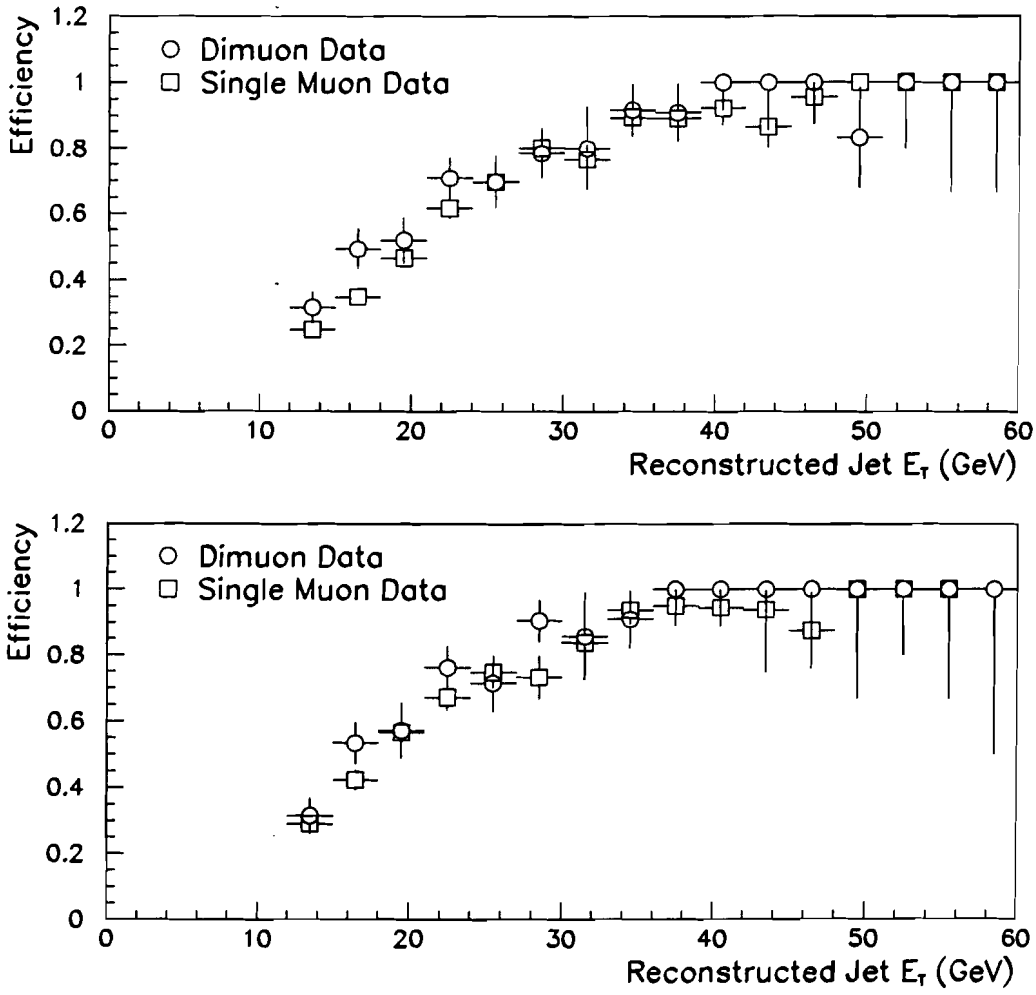

Figure 4-9: Comparison of Level 1 jet trigger efficiency as a function of reconstructed jet E_T for (a) all jets and (b) jets associated with muons in single muon and dimuon data.

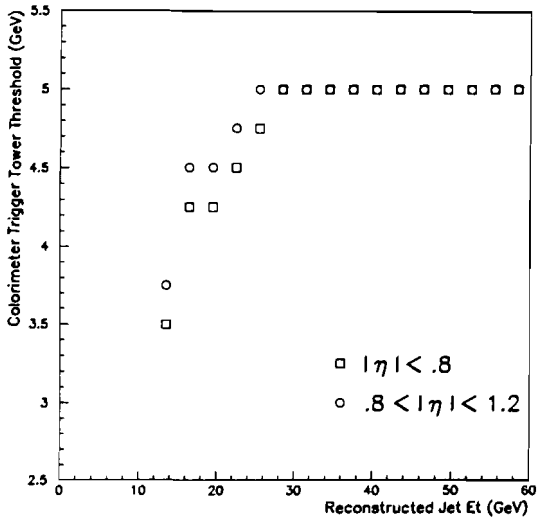

Figure 4-10: Monte Carlo calorimeter trigger tower energy threshold required to match the jet trigger efficiency given by the 3.0 GeV threshold in data as a function of the E_T of the jet reconstruction which contains the energy within the tower.

the trigger towers in each region.

The dependence of the Monte Carlo trigger tower thresholds on the reconstructed E_T of the jet which contains the energy within these towers suggests that the modeled energy depositions within individual calorimeter cells in the Monte Carlo require both additive and scaling corrections to accurately describe the energy depositions of an equivalent jet in the data. One source of additive corrections are sources of calorimeter noise which are not accounted for in the Monte Carlo. For example, the additional energy deposition associated with the subset of events in which more than one $p\bar{p}$ interaction occurred within the beam crossing associated with the event is not simulated in the Monte Carlo. An improper model for the fraction of the incident energy which is measured in the individual calorimeter cells contained within a jet reconstruction is one example of an effect which would require a scaling correction in the Monte Carlo model. An even more complicated correction would be required if the modeled width of jets in the Monte Carlo was

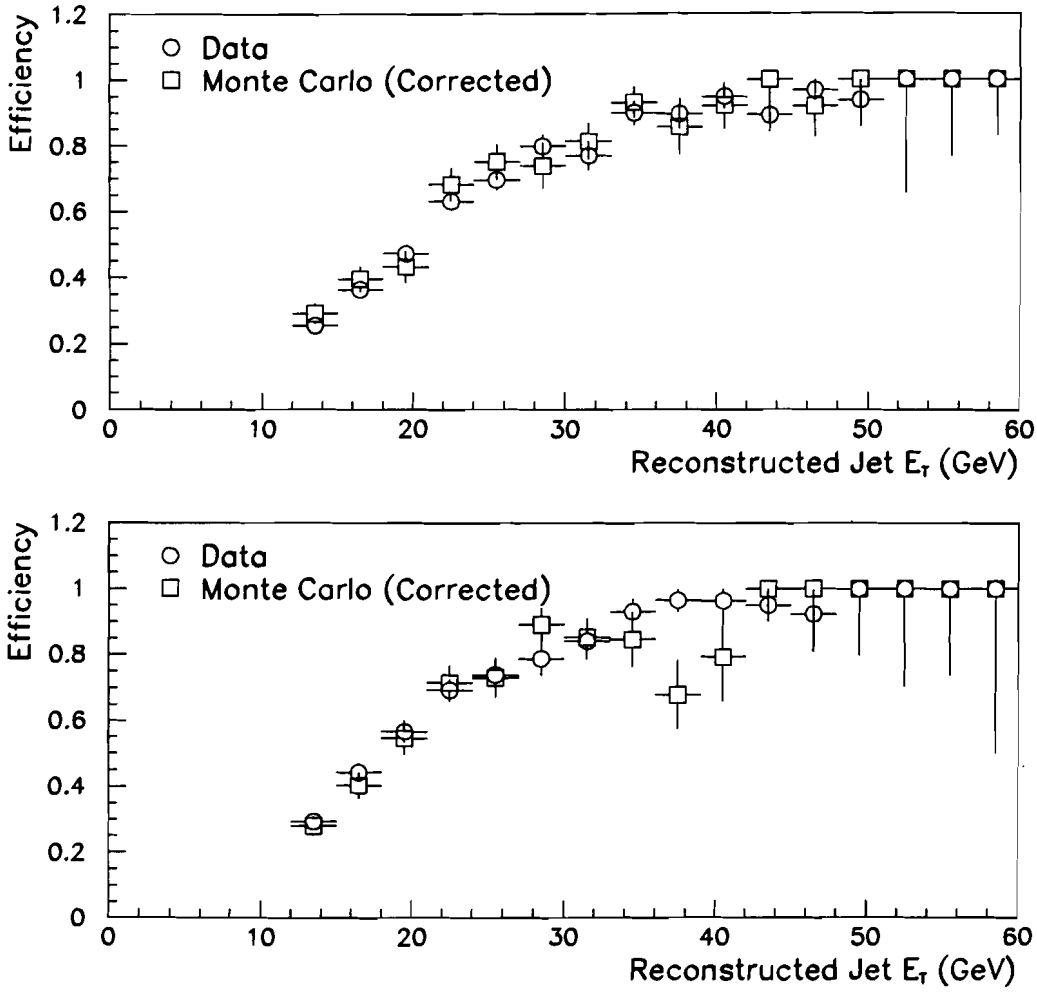

Figure 4-11: Comparison of Level 1 jet trigger efficiency as a function of reconstructed jet E_T for (a) all jets and (b) jets associated with muons between data and corrected Monte Carlo.

found to disagree with the actual width of jets in the data. Since the energy deposition associated with a given jet would be either more or less concentrated in the calorimeter cells in the vicinity of the jet axis, neither a scaling or additive correction could be made to the energy deposition within the individual calorimeter cells which could account for this effect. Therefore, in order to account for all the different potential sources of disagreement between the modeled calorimeter energy deposition in the Monte Carlo and that found in the data, the previously described correction scheme in which jet trigger tower thresholds were modified as a function of the reconstructed E_T of the jet which contains the energy within the tower was used.

Using the modified energy deposition thresholds for Monte Carlo trigger towers shown in Fig. 4-10, a comparison of the Level 1 jet trigger efficiency between data and corrected Monte Carlo is shown in Fig. 4-11. Based on the agreement shown here the Level 1 jet trigger bits in each Monte Carlo event were overwritten utilizing the modified energy deposition thresholds for the calorimeter trigger towers. The corrected trigger information was assumed to model the Level 1 jet trigger efficiency found in the data.

4.3.3 Level 2 Jet Trigger Efficiency

A comparison of the Level 2 jet trigger efficiency in data and Monte Carlo was also made using the sample of unbiased jets found in subset of the dimuon event sample which satisfied the Mu-2-High trigger requirement. The Level 2 jet trigger efficiency described here was defined as the fraction of reconstructed jets with associated Level 1 trigger towers above the 3 GeV energy threshold which also had a jet reconstructed in the Level 2 software trigger. For each reconstructed jet where an associated calorimeter trigger tower above the required energy threshold was found within a $\Delta R = 0.5$ search cone around the jet axis, a search was performed

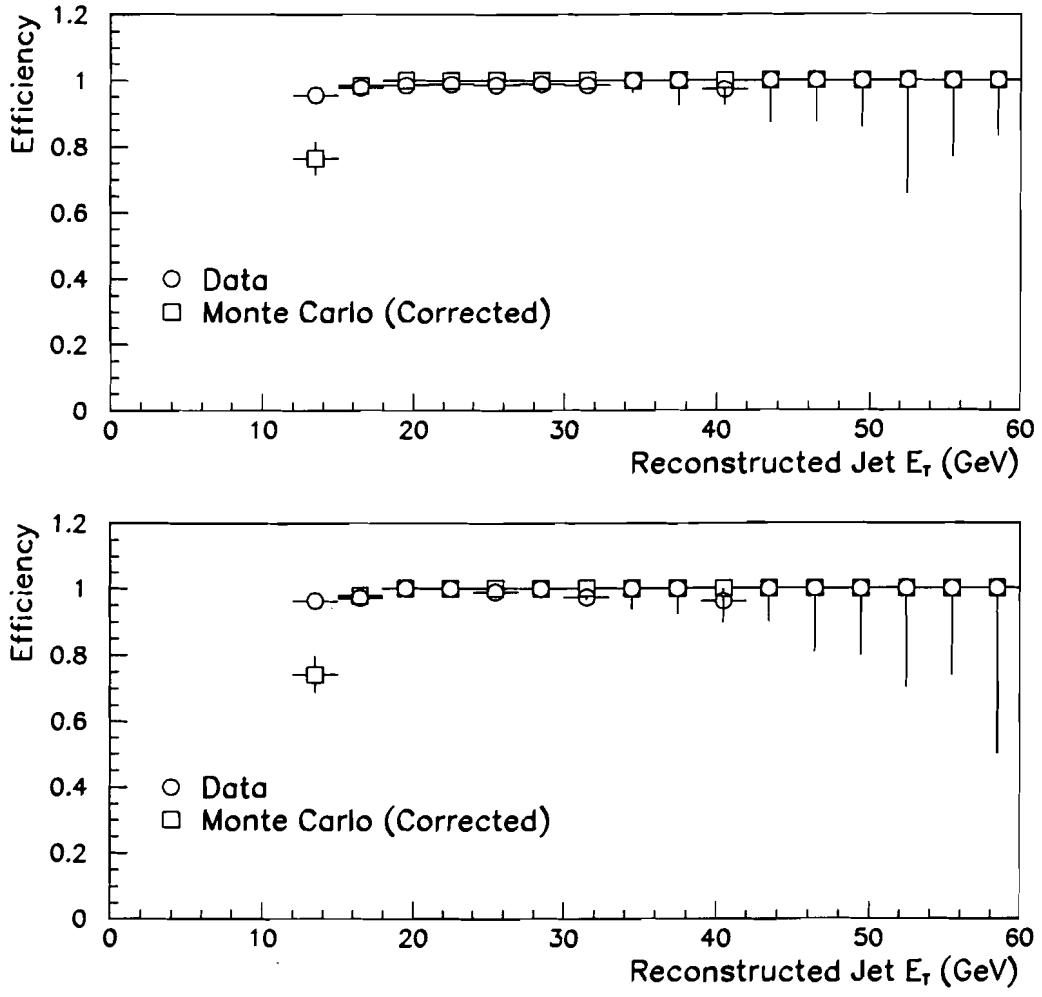

Figure 4-12: A comparison of Level 2 jet trigger efficiency between data and corrected Monte Carlo as a function of the E_T of the offline reconstruction of the jet for (a) all jets and (b) jets associated with muons.

in the same cone for an associated Level 2 jet with $E_T^{jet} > 10$ GeV. The 10 GeV threshold for Level 2 jets was chosen to match the Level 2 jet trigger condition found in the trigger requirements utilized in this analysis. The resulting Level 2 jet trigger efficiency as determined from data and Monte Carlo is shown in Fig. 4-12 for all jets in these events and for those jets associated with muons. The Level 1 requirement for Monte Carlo jets utilized in this comparison was based on the modified calorimeter trigger tower energy deposition thresholds.

The efficiency curve obtained from the data as shown in Fig. 4-12 suggests that the Level 2 jet trigger efficiency for reconstructed jets with an associated Level 1 trigger towers above the minimum energy deposition threshold is approximately 100% for all jets with $E_t > 12$ GeV. The inefficiency shown in the lowest E_T bin for the Monte Carlo can be attributed to the fact that the information regarding energy deposition in the calorimeter which was used at the trigger simulation level was not corrected based on the jet energy scale corrections provided by CAFIX. Even though the energy scale of reconstructed jets in the Monte Carlo was corrected upward, the energy scale of Level 2 jets remained unchanged. Therefore, a reconstructed jet in the Monte Carlo with $E_T^{jet} > 12$ GeV could be reconstructed in Level 2 below the 10 GeV threshold. The simple method used to correct for this discrepancy was to assume that all jets in the Monte Carlo which were found to have an associated Level 1 trigger tower above the required energy deposition threshold and a reconstructed energy such that $E_T^{jet} > 12$ GeV had a Level 2 jet trigger efficiency of 100%.

Chapter 5

Mixing Measurement

5.1 Extraction of χ from Data

As previously discussed in Section 1.4.2, high energy $p\bar{p}$ collisions result in the production of $b\bar{b}$ quark pairs. The sign of the lepton which is produced in the semileptonic decay of an individual bottom quark can be utilized as a direct tag of the quark flavor at the time of its decay. The semileptonic decay of a b quark produces a ℓ^-, while the same decay of a $\bar{b}$ produces a ℓ^+. Therefore, unlike sign lepton pairs are expected from events where both quarks in the $b\bar{b}$ pair decay semileptonically. If, however, one of the quarks hadronizes into a neutral meson (B_d^o or B_s^o), there is some probability that the meson will oscillate into the opposite flavor state prior to its decay. In this case, the semileptonic decay of both quarks will result in the production of like sign dilepton pairs which in principal provides a signature for the mixing process.

In practice, the relative number of like sign and unlike sign dilepton pairs which one observes in the data must be corrected for dilepton backgrounds which result from other production mechanisms. One significant background arises from cascade decays of the type $b \rightarrow c \rightarrow \ell^+$ which produce leptons that are oppositely charged with respect to those produced in the direct semileptonic decay $b \rightarrow \ell^-$. A $b\bar{b}$ quark pair can produce a like sign dilepton pair via the semileptonic decay

of one quark in combination with the cascade decay of the opposite quark and in the process replicate the signature for mixing described above. Other background sources of dilepton pairs include decays of J/ψ and Υ, semileptonic decay of $c\bar{c}$ quark pairs, Drell-Yan production, and in-flight decays of π and K mesons within the tracking volume of the detector in conjunction with the semileptonic decay of one heavy quark.

Since the inner tracking region of the DØ detector is not enclosed in a magnetic field, it is not possible to identify the charge of electron candidates which are observed in the calorimeter. The charge of muon candidates, on the other hand, can be determined from the observed bend of a muon track in the magnetized iron toroid between the inner and middle layers of the muon system. Since lepton charge information is required to tag the flavor of a particular b-hadron at the time of its decay, the mixing measurement performed at DØ is restricted to an analysis of dimuon pairs. The experimental parameter which one measures is simply the ratio of like sign dimuon pairs to unlike sign dimuon pairs as shown:

$$R \equiv \frac{N(\mu^+\mu^+) + N(\mu^-\mu^-)}{N(\mu^+\mu^-)}. \tag{5.1}$$

In order to extract a value for the mixing probability χ from a measured value of R, it was necessary to model the relative contributions of all the processes which contributed dimuon events to the data sample utilized in this analysis. As illustrated in Table 5-1, each dimuon production mechanism provided distinct fractions of like and unlike sign events to the sample. Since a b hadron which changes flavor via the mixing process decays into a muon with an opposite sign to that which is otherwise expected, the magnitude of the like and unlike sign fractions for processes in which both muons are produced in the decays of distinct b hadrons is dependent on the value of the mixing probability χ. For example, dimuon events which arise from the direct semileptonic decay of both quarks within a $b\bar{b}$ pair (P1) have an

unlike sign fraction equivalent to the sum of the probability for both b hadrons mixing prior to their decays (χ^2) with the probability that neither b hadron mixes prior to its decay ($(1-\chi)^2$). Conversely, the like sign fraction corresponds to the combined probabilities for either of the b hadrons undergoing mixing while the other does not.

It should also be noted that dimuon production mechanisms in which one muon is produced in the prompt decay of a b or c quark and the other arises from the in-flight decay of a pion or kaon (P5) provide only approximately equal numbers of like and unlike sign events to the data sample. The additional charged particles which result from the decay of a heavy quark into a muon have a combined charge which is opposite to that of the produced muon. Therefore, in cases where a second muon is produced in the in-flight decay of a charged particle which was an additional product of the original semileptonic decay, the sign of the second muon will have a slight preference for being opposite to that of the original muon. However, the cut on dimuon invariant mass which was utilized in this analysis (see Section 5.2.1) eliminated a large fraction of these events, and the resulting fractions of like and unlike sign events associated with these processes were found to be equal within the statistical errors of the Monte Carlo sample.

The relative contribution of each dimuon production mechanism to the final data sample was determined using Monte Carlo simulations, and this information was then used to extract a value of χ from the measured value of the experimental parameter R as the solution to a quadratic equation. The form of this quadratic equation is

$$A\chi^2 + B\chi + C = 0 \tag{5.2}$$

Label	Like Sign	Unlike Sign	Process
P1	$2\chi(1-\chi)$	$(1-\chi)^2+\chi^2$	$b \to \mu^-;\ \bar{b} \to \mu^+$
P2	$(1-\chi)^2+\chi^2$	$2\chi(1-\chi)$	$b \to \mu^-;\ \bar{b} \to \bar{c} \to \mu^-$
P3	$2\chi(1-\chi)$	$(1-\chi)^2+\chi^2$	$b \to c \to \mu^+;\ \bar{b} \to \bar{c} \to \mu^-$
P4	0%	100%	$b \to c\mu^-;\ c \to \mu^+$
			$c \to \mu^+;\ \bar{c} \to \mu^-$
			Drell-Yan
			$J/\psi,\ \Upsilon \to \mu^+\mu^-$
P5	50%	50%	$b \to \mu^-;\ \pi/K \to \mu$
			$c \to \mu^+;\ \pi/K \to \mu$
			$\pi/K \to \mu\ ;\ \pi/K \to \mu$
P6	100%	0%	No Physical Process

Table 5-1: Fraction of like and unlike sign dimuons from processes contributing to dimuon production.

where A, B, and C are defined as follows:

$$\begin{aligned} A &= 2(P_2 - P_1 - P_3)(1+R) \\ B &= 2(P_1 + P_3 - P_2)(1+R) \\ C &= .5(1-R)P_5 + (P_2 + P_6) + R(P_1 + P_3 + P_4). \end{aligned} \tag{5.3}$$

The P_i denote the fractional contributions to the final event sample from each of the six categories of dimuon production mechanisms as defined in Table 5-1.

5.2 Event Selection

The resolution in the measurement of the mixing probability χ which is obtained with method described above is related to both the number of collected dimuon events and the fraction of those events which result from the direct semileptonic decay of both quarks from a $b\bar{b}$ pair (P1). As shown in Table 5-1, events in which one or both quarks in a $b\bar{b}$ pair produce a muon through a cascade decay (P2 and P3) also provide a signature for mixing. However, since the mixing signature for

the class of events with one cascade decay (P2) is exactly opposite to that for events produced from the direct semileptonic decay of both quarks (P1), a data sample with an equal number of events from P1 and P2 will provide no net information with regard to mixing. Therefore, a set of selection cuts on the data is chosen to maximize the fraction of dimuon events from P1 while maintaining the largest possible statistical sample of events. The different cuts which are utilized in this analysis are summarized below.

5.2.1 Dimuon Invariant Mass

The invariant mass of dimuon pairs in this analysis is restricted to the region between 6 GeV/c^2 and 40 GeV/c^2. The lower cut on invariant mass is chosen to reduce the relative contribution of several background dimuon production mechanisms. One such background is the dimuon decay channel of the J/ψ meson which can be formed both in b quark decays and through direct production mechanisms. The resolution of dimuon pairs in the DØ muon system gives rise to a J/ψ mass peak which is well fitted by a Gaussian with a mean value of $M_{J/\psi} = 3.053 \pm 0.005$ GeV/c^2 and width $\sigma = 0.38$ GeV/c^2 [43]. The resulting cross section for reconstructed J/ψ decays with a dimuon invariant mass greater than 6 GeV/c^2 is found to be negligible with respect to other dimuon production processes based on the above resolution. Dimuon pairs from decays of lower mass mesons such as the η, ρ, ω, and ϕ have even smaller probabilities for being reconstructed above 6 GeV/c^2 and can also be ignored in the mixing analysis.

Another significant background to the subset of the dimuon data sample relevant to the mixing analysis is the class of events where both muons are produced in the decay chain of an individual bottom quark. In the semileptonic decay mode of the bottom quark, the resulting charm quark can also decay semileptonically resulting in the production of a dimuon pair. Since any flavor change in the b hadron

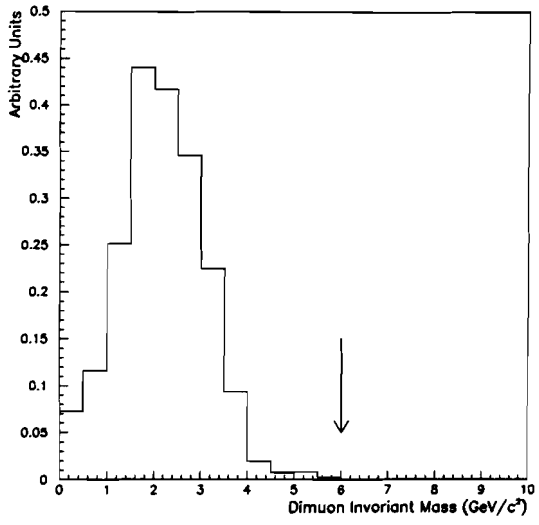

Figure 5-1: Normalized invariant mass spectrum of dimuon Monte Carlo events where the c quark produced in the semileptonic decay of a b quark also decays semileptonically to produce a second muon.

will occur prior to its decay, the dimuon events resulting from these decays will be 100% opposite signed as illustrated in Table 5-1. A normalized invariant dimuon mass spectrum for this particular class of bottom quark decays from the Monte Carlo is shown in Fig. 5-1. The lower invariant mass cut of 6 GeV/c^2 reduces the relative contribution of this production mechanism for dimuon events in the data sample to negligible levels.

An additional consequence of the imposition of a lower cut on dimuon invariant mass is that the relative contribution of leading order and next-to-leading order production of heavy quark pairs as represented in the data sample is substantially altered. The normalized invariant mass distributions for dimuon events in the Monte Carlo resulting from both leading order (solid lines) and next-to-leading order (dotted lines) heavy quark pair production are shown in Fig. 5-2. The previously described class of events in which both muons are produced in the decay chain of an individual bottom quark are not included in these distributions

since the invariant mass distribution associated with these events is independent of differences in leading and next-to-leading order production of the heavy quark pairs. The institution of a lower cut of 6 GeV/c^2 on the invariant mass of dimuons in the event sample serves to substantially enhance the relative fraction of events resulting from leading order heavy quark pair production. The enhancement of leading order processes in the higher dimuon invariant mass range is a result of the fact that leading order heavy quark pairs have a smaller net momentum than those produced in next-to-leading order processes. The dimuon pairs created in the decays of leading order heavy quark pairs are therefore more back-to-back in the frame of the detector and hence have a larger average invariant mass.

The upper cut on dimuon invariant mass is chosen to ensure that the acceptance for dimuon pairs from Z° decays into the final data sample is negligible. Since the muons produced in these decays are typically isolated with respect to energy in the calorimeter, this class of events is even further suppressed with the requirement of at least one reconstructed jet with $E_T^{jet} > 12$ GeV associated with either muon in the event as discussed in the following section.

5.2.2 Associated Jet Requirement

A reconstructed jet is considered to be associated with a muon candidate if the spacing between the jet axis and the reconstructed muon track defined as $\Delta R = \sqrt{(\Delta\eta)^2 + (\Delta\phi)^2}$ is found to be less than 0.8. If more than one reconstructed jet is found within $\Delta R = 0.8$ of a muon track candidate, the jet nearest to the muon track is defined to be the jet associated with that particular muon candidate. The associated jet requirement made in this analysis is that at least one of the two reconstructed muons in the event must have an associated jet with $E_T^{jet} > 12$ GeV. Reconstructed jets with transverse energy below 12 GeV were excluded from this analysis since large uncertainties were associated with the reconstruction and

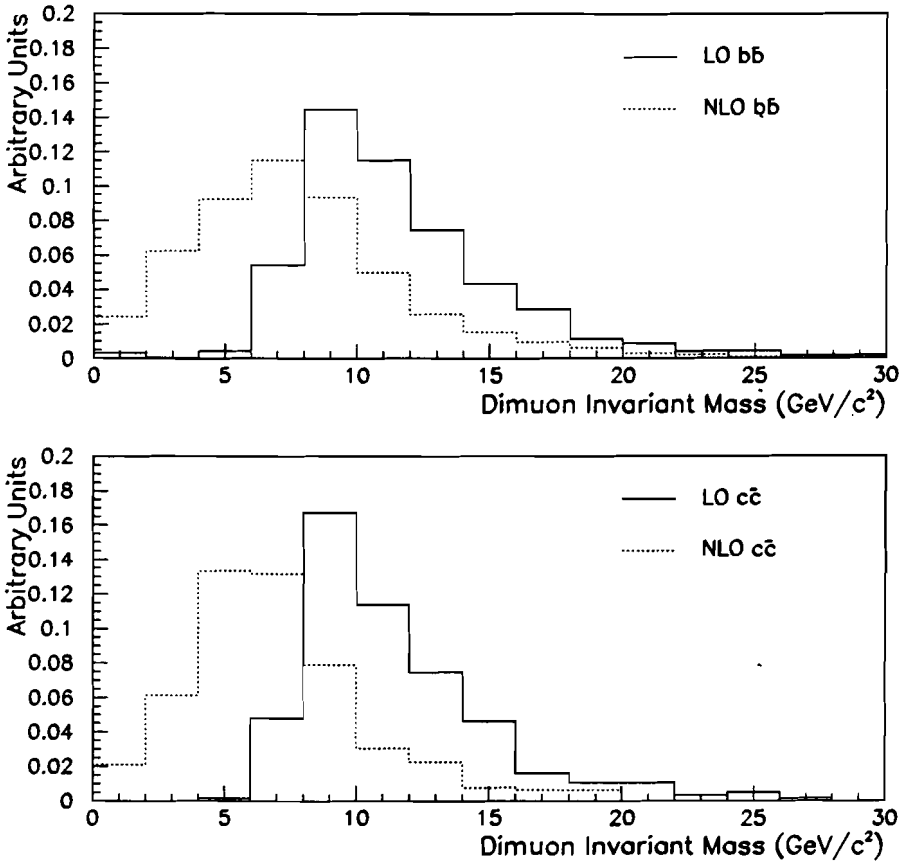

Figure 5-2: Normalized invariant mass spectrum of dimuon Monte Carlo events from leading order and next-to-leading order generated heavy quark pairs where one muon is produced in the decay of each quark for (a) $b\bar{b}$ quark pairs and (b) $c\bar{c}$ quark pairs.

trigger efficiencies for the jets in this kinematic region.

One function of this cut was to remove events from the data sample which resulted from dimuon production mechanisms in which the produced muons are isolated with respect to energy in the calorimeter. In the restricted invariant mass range of this dimuon analysis, the two background production processes which result in isolated dimuons are the decay of Υ mesons and Drell-Yan production. A study performed with Drell-Yan Monte Carlo events indicated that the acceptance for this class of events into the data sample was reduced by a factor of 75 when the associated jet requirement described above was added. The relative contribution of Drell-Yan events to the final data sample after all cuts was determined to be less than 1% of the total (see Table 5-5).

No complete Monte Carlo for bottomonium production at $\sqrt{s} = 1.8$ TeV was available for use in this analysis. An event generator written by Mangano [44] was available for performing the hard scattering to produce the nine known Υ and χ_b states. The software package to perform subsequent decays of these states and create a ZEBRA data structure compatible with the DØ standard was written internally within the DØ Collaboration [39]. Since the Monte Carlo did not include a package to fragment quarks and gluons within the events, only the direct products of the bottomonium decays appeared within the simulated events. This deficiency made it impossible to directly study the effect of an associated jet requirement on the acceptance for dimuon events from Υ decays. Therefore, in order to obtain a rough estimate of the relative contribution of Υ decays to the final dimuon data sample, it was necessary to make the assumption that the isolation of muon candidates with respect to energy deposition in the calorimeter was nearly identical in dimuon events originating from Drell-Yan production and Υ decays.

The cross section for the sample of Υ events produced with the Monte Carlo simulator described above was normalized to the DØ measurement of the Υ cross

section [39]. The cross sectional weight assigned to individual Monte Carlo events was determined independently for events in each of five separate P_T^{Υ} bins encompassing the region between 0 GeV/c and 25 GeV/c. The individual event weight was determined by dividing the measured cross section in each of the bins by the number of generated Monte Carlo events in the bin. After all of the cuts utilized in this analysis which did not involve energy deposition in the calorimeter were made on both the Drell-Yan and Υ Monte Carlo samples, the resulting cross section for dimuons from Υ decays was found to be a factor of 2.9 higher than that for Drell-Yan produced dimuons. Utilizing the assumption that cuts involving calorimeter energy have the same net effect on both samples, the relative contribution of dimuon events from Υ decays in the final event sample after all cuts was determined to be on the order of 2.5%.

The requirement of at least one associated jet per event is also important in that subsequent cuts involving variables which describe the relationship between a muon and its associated jet are important in separating muons produced in b quark decays with those from decays from lighter particles. These cuts are only effective if a substantial fraction of muons in the sample do in fact have associated jet activity reconstructed in the calorimeter. In the following section one such cut utilized in this analysis is discussed in greater detail.

5.2.3 Muon P_T Relative to Associated Jet Axis

The transverse momentum of a muon track relative to the axis of an associated jet (P_T^{rel}) is one example of a muon-jet variable which is useful in separating muons from b quark decays from those associated with other sources. The jet axis used in the calculation of this particular variable is constructed through the vector addition of the three momenta of the reconstructed associated jet with the three momenta of the reconstructed muon track. The expected minimum ionizing energy

deposition along the muon track is subtracted from this result as a three vector along the muon track direction with a magnitude equal to the expected energy loss. Since this definition of the jet axis properly accounts for the muon momentum and energy, it represents the best possible reconstruction of the original direction of the incident quark whose decay products are the muon and the additional particles which form the energy deposition in the calorimeter.

Once the combined muon-jet momentum has been determined the muon transverse momentum relative to the combined jet axis is calculated as

$$P_T^{rel} = |\vec{P}_\mu| sin\theta \tag{5.4}$$

where

$$cos\theta = \frac{\vec{P_{jet}} \cdot \vec{P}_\mu}{|\vec{P_{jet}}||\vec{P}_\mu|} \tag{5.5}$$

The products associated with the decay of an incident hadron have kinematic properties which are directly related to the mass of the decaying particle. If the mass difference between the incident hadron and a particular decay product is small, the direction of the decay product will be nearly identical to the direction of the incident hadron. If the mass difference is larger, however, the potential trajectories of the decay product will encompass a wider spatial region in which the path of the decay product is allowed to be further separated from the incident hadron direction. The P_T^{rel} variable is representative of this "kick" away from the original direction of the decaying particle which is imparted to the muon produced in the decay.

Since the b quark has a mass which is on order of four times greater than that of the c quark, the mass difference between a muon decay product and a parent b hadron will be much greater than the mass difference between the same muon and a parent c hadron. The additional mass difference between a muon and b hadron

parent means that the P_T^{rel} spectrum for muons produced in the direct semileptonic decay of these hadrons will be much broader than the same spectrum for muons produced in the decay of lighter hadrons. Normalized P_T^{rel} spectra constructed from ISAJET Monte Carlo events are illustrated in Fig. 5-3. The upper half of the figure shows the different shapes of the P_T^{rel} spectrum for muons produced in the decay of b hadrons and c hadrons in addition to those produced in the in-flight decays of lighter mesons.

In the case of light meson decays into muons, it is important to note that the mesons are themselves likely to be decay products of the incident quark or gluon. Therefore, the associated jet represents a reconstruction of the incident quark or gluon rather than the light meson parent itself. Consequently, the P_T^{rel} spectrum for these decays can not be directly related to the mass difference between the light meson and its muon decay product. In fact, the P_T^{rel} spectrum for muons produced in light meson decays turns out be nearly identical to that for those produced in c hadron decays.

The lower half of Fig. 5-3 illustrates the difference between the P_T^{rel} spectra for b hadron decays in which the muon is produced in the direct semileptonic decay of the b hadron and those which are produced in cascade decays where the actual muon parent is a c hadron produced in the decay of the original hadron. As in the case of light meson decays, jets associated with the muons produced in b hadron cascade decays are not reconstructions of the c hadron, the direct parent of the muon. Therefore, the P_T^{rel} spectrum for muons with c hadron parents that are produced in cascade decays of b hadrons is not equivalent to that for muons in which the c hadron parent is created in the direct fragmentation of an incident c quark.

Each muon in the dimuon data sample which has an associated jet with $E_T >$ 12 GeV is required to have a calculated $P_T^{rel} > 1.2$ GeV. As the arrows in Fig. 5-3

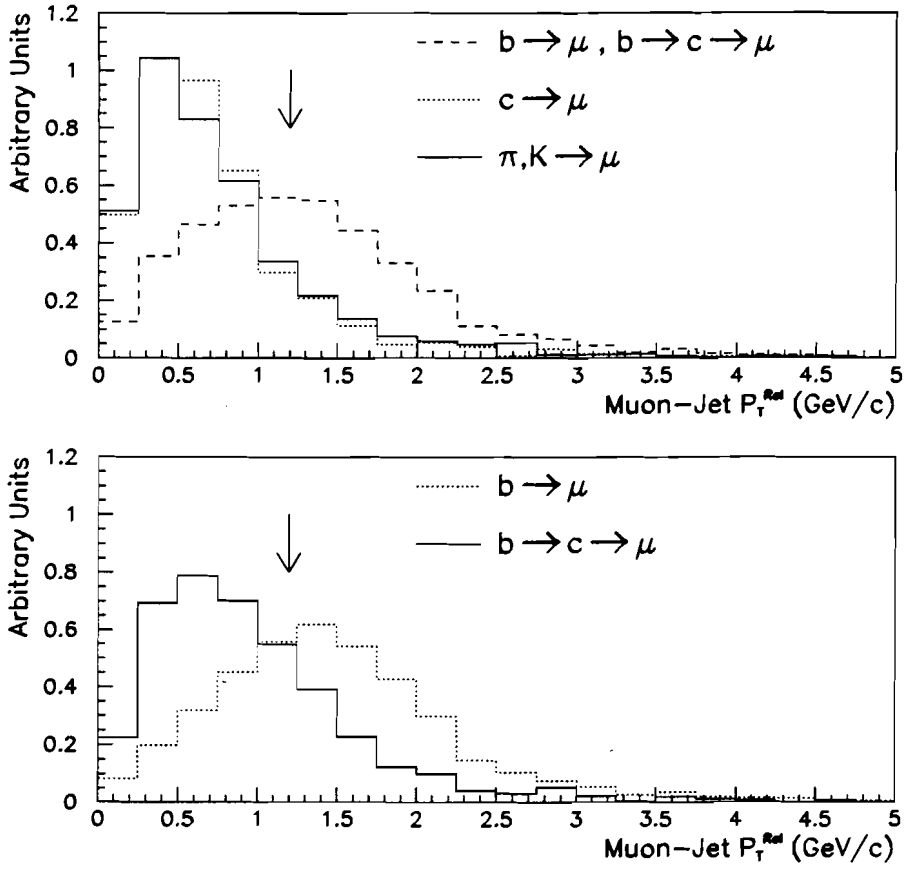

Figure 5-3: Comparison of the normalized P_T^{rel} spectra from Monte Carlo for different sources of muon production. An invariant mass cut equivalent to the one used in this analysis is made on the dimuon Monte Carlo prior to selecting candidates for these distributions. Each muon in the selected events which has an associated jet with $E_T > 12$ GeV is included in constructing the distributions.

illustrate, the effect of this cut is to eliminate a large fraction of events in which the source of either muon in the event is something other than the direct semileptonic decay of a b hadron. The effect of this cut is somewhat diminished, however, due to the fact that only one muon per event is required to have an associated jet. Even though the additional requirement that associated reconstructed jets be found for both muons in each event would help to raise the percentage of events from P1, the drop in statistics due to the additional loss in event acceptance would negate the beneficial effect of the additional requirement on the mixing result.

5.2.4 Muon P_T

One criteria used in the definition of a good muon as described in Section 3.2.1 is the requirement that the reconstructed P_T of the muon track candidate must lie in the range 3 GeV/c $\leq P_T^{\mu} \leq$ 25 GeV/c. A further restriction on this range at the event selection stage is found to be useful in further reducing the relative percentage of muons in the data sample which are not produced in the direct semileptonic decays of b hadrons.

The normalized P_T spectra for the trailing muons in dimuon Monte Carlo events are shown for the different potential production mechanisms of the muon in Fig. 5-4. The invariant mass cut and associated jet requirement described previously are made on the dimuon Monte Carlo prior to selecting candidates for these distributions in order to illustrate the effect of an additional requirement on muon P_T subsequent to other cuts performed in this analysis.

The upper half of Fig. 5-4 illustrates the somewhat broader P_T spectrum associated with muons resulting from the hadronization and subsequent decay of b quarks as compared to those arising either from incident c quarks or in the decays of light mesons. As discussed in Section 4.1.1 the momentum loss which is sustained by an incident quark in the process of hadronization is dependent on the

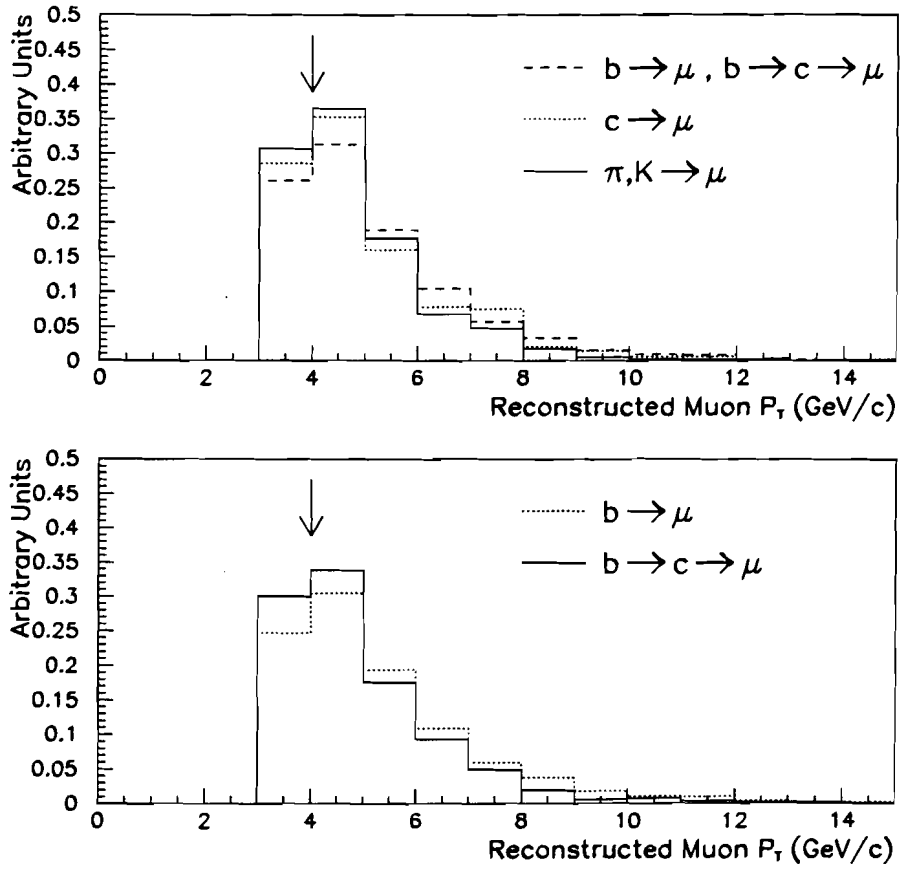

Figure 5-4: Comparison of the normalized P_T spectra from trailing muons in dimuon Monte Carlo events for the different production mechanisms of the trailing muon. An invariant mass cut consistent with the one used in this analysis and the requirement of at least one reconstructed jet associated with either muon are made on the dimuon Monte Carlo prior to selecting candidates for these distributions.

mass of the quark. The loss of momentum which is suffered in the hadronization of a b quark is on average smaller than that for an incident c quark with an equivalent momentum. Since the b hadron maintains a larger fraction of the incident quark momentum, a higher average momentum value is associated with the muons produced in the decays of those hadrons.

The difference in the muon P_T spectra for the different production mechanisms is also dependent on the kinematic properties of the respective decays. Since the average momentum of the heavy quark hadrons which are produced in $p\bar{p}$ collisions at $\sqrt{s} = 1.8$ TeV is on the same order as the mass of the hadrons, the particle mass is an important contribution to the total energy of the hadron. Therefore, the energy which is available in the decay of a b hadron will be greater than that in the decay of a c hadron with an equivalent momentum, and the resulting muons produced in the decays of the heavier hadrons will have a higher average P_T. The lower half of Fig. 5-4 shows a comparison between normalized P_T spectra for muons produced in the direct semileptonic decays and cascade decays of b hadrons. In cascade decays the c hadron direct parent of the muon is produced in the original decay of the incident b hadron and therefore possesses only some fraction of the original b hadron momentum. The relative higher average P_T of muons resulting from direct semileptonic decays with respect to those produced in cascade decays is a consequence of both the higher mass of direct parent hadron and the resulting momentum difference between an incident b hadron and its c hadron decay product which becomes the parent particle for muons produced in cascade decays.

In the case of this analysis, the lower cut on muon P_T is raised to 4 GeV/c for both muons in the event. As illustrated in Fig. 5-4 this requirement serves to further increase the percentage of muons from the direct semileptonic decays of b hadrons in the final data sample.

5.3 Determination of R from Data

The dimuon data sample which is utilized in the determination of the experimental parameter R was restricted to events collected with either the Mu-2-High or Mu-1-Jet trigger conditions as defined in Table 3-1. The increase in the statistical sample which was obtained from including events collected exclusively with the Mu-Jet-Low trigger condition was found to be less than 20%, a gain which was offset by the additional complications inherent to the inclusion of an additional trigger bit in the analysis. Events in which two or three reconstructed muon track candidates were found which passed the fiducial and quality cuts described in Section 3.2.1 were collected and subjected to further analysis. The event sample was further pared with the requirement that the two leading P_T muons in each event pass the medium set of cosmic cuts as defined in Table 3-2.

The resulting set of events was then subjected to each of the event selection criteria described in Section 5.2 in order to maximize the relative percentage of events in the data sample in which both muons were produced in the direct semileptonic decays of b hadrons (P1). The number of events which survived each stage of the selection process is illustrated in Table 5-2. About 37% of the events in the final data sample had multiple interaction vertices reconstructed within collision region of the detector, but all dimuon pairs in these events were determined to be consistent with a single interaction vertex. In order to make this determination, the event displays associated with each of events in the final data sample which were found to contain multiple interaction vertices were scanned to distinguish events which could be consistent with muons produced in separate interaction vertices. The conclusion of this study was that none of the dimuon events in this sample were consistent with production from multiple interaction vertices.

Out of the 183 events which passed all the cuts, 121 were found to have opposite sign muons and 62 were found to have same sign muons. The corresponding value

Event Requirements	Number of Events
Fiducial and Quality Cuts on Muon Tracks	33956
Cosmic Cuts on Two Leading P_T Muons	3730
Invariant Mass Cut	1312
Associated Jet Requirement	754
Muon P_T Cut	544
Muon-Jet P_T^{rel} Cut	183

Table 5-2: Number of events in data passing each stage of the event selection.

for the experimental parameter R is

$$R = \frac{62}{121} = 0.51 \pm 0.08(stat). \tag{5.6}$$

5.4 Determination of Cosmic Background

Although the majority of cosmic ray events were removed from the data sample via the cosmic cuts on the two leading P_T muons and the imposition of an associated jet requirement, the value for the experimental parameter R still needed to be corrected for the small cosmic ray background which existed in the final event sample. This background was determined using two independent methods. The first technique utilized maximum likelihood fits to the floating t_o parameter for muon tracks as described in the following section to determine the number of background events from cosmic rays in both the like and opposite sign subsets of the final event sample. As a consistency check, the event displays associated with each of the 183 events in the final sample were scanned by eye to make an independent determination of the number of cosmic ray events in the sample.

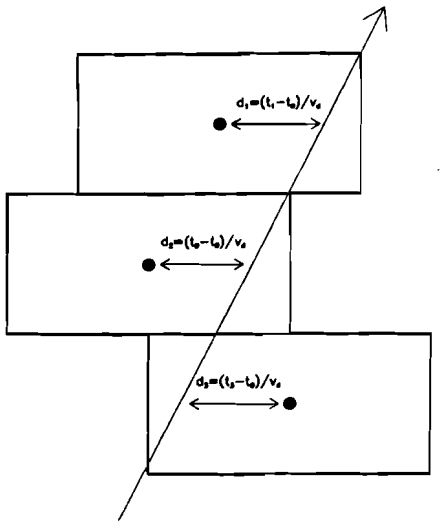

Figure 5-5: Calculation of the bend view position of a muon track within three adjacent drift cells traversed by the muon.

5.4.1 Floating t_o Parameter

The bend view position of a muon track within an individual drift cell in the muon system is proportional to the elapsed time between the corresponding bunch crossing in which the muon is created and the arrival time of charge at the anode wire in the cell. As illustrated in Fig. 5-5, the distance between an observed muon track and the anode wire within a particular cell is calculated via the subtraction of the beam crossing time (t_o) from the charge arrival time at the wire (t_i) and the subsequent division of the result by the drift velocity within the cell (v_d).

In the standard muon reconstruction code the value of the t_o parameter used in these calculations is constrained to the actual crossing time of the proton and antiproton bunches at the interaction point of the detector. In the case of cosmic ray events, however, the time associated with a muon track passing through the detector is random with respect to the bunch crossing times. If a refit of the muon track is performed in which the t_o parameter is allowed to remain a free parameter

in the fit, the value of t_o which gives the best track fit is representative of the arrival time of the muon in the detector. The distribution of this muon track parameter (floating t_o) is expected to be sharply peaked at the bunch crossing time for beam produced muons and spread out over a wider range for cosmic ray muons. The calculation of the floating t_o parameter can sometimes result in a null result if for example there are not enough hits along the track to tightly constrain the reconstruction. These tracks are assigned a floating t_o value of -599. Since the relative number of muon tracks for which the floating t_o calculation fails is different for beam produced and cosmic ray muons, muons in the data sample for which the floating t_o parameter is set to -599 are included in the maximum likelihood fits used to constrain the cosmic background.

5.4.2 Determination of Floating t_o Distributions

In order to determine the magnitude of the cosmic ray background in the final event sample using a maximum likelihood fit to the floating t_o distribution for the muon tracks in those events, it was first necessary to construct distributions of the floating t_o parameter for muon tracks in both signal and cosmic ray events. The floating t_o distribution for beam produced muon tracks was determined from two distinct dimuon data samples. Both data samples were constructed from events in which the two leading P_T muons in the event passed the tight cosmic cuts as defined in Table 3-2. In addition, the P_T of both muons was required to be greater than 4 GeV/c to be consistent with the cut on this parameter made in the mixing analysis.

Events in the first sample were constrained to the invariant mass range between 6 GeV/c^2 and 40 GeV/c^2, while events in the second sample were restricted to the J/ψ invariant mass region between 2 GeV/c^2 and 4 GeV/c^2. The requirement of one reconstructed jet with $E_T > 12$ GeV associated with either muon in the event

was made exclusively on the first sample to help eliminate cosmic ray background. Since the invariant mass range of sample one was consistent with that for dimuon events reconstructed from cosmic ray muons passing through two sides of the detector, this additional requirement served to further reduce the small percentage of cosmic ray muons which remained in sample one subsequent to the imposition of tight cosmic cuts. The figure in the upper left corner of Fig. 5-6 shows a comparison of normalized floating t_o distributions for muon tracks in sample one (solid line) and sample two (dashed line). The agreement in the floating t_o distributions constructed from the two independent data samples provided confidence that the distributions were representative of those for pure beam-produced muons. The figure in the upper right corner of Fig. 5-6 shows the functional fit which was obtained on the average of the normalized distributions from both samples superimposed against that average.

The floating t_o distribution for muon tracks produced in cosmic ray events was also determined from two distinct dimuon data samples. The first sample consisted of events which were collected in special cosmic ray runs taken at the end of the 1992-93 collider run. The events in this sample were subjected to a minimal subset of the cuts which were utilized in the mixing analysis including those involving invariant mass, opening angle, and muon P_T. The second event sample was constructed from events in the standard dimuon data stream. Cosmic ray events in this sample were identified using a reverse set of cosmic cuts on the muon tracks in the events. The first inverted cosmic requirement was that neither muon in the event had a matching central detector track. The second prerequisite was that the sum of the energy in the calorimeter cells traversed by each muon track plus their nearest neighbor cells had to be less than 0.4 GeV. As discussed in Section 3.2.2, the requirements of matching central detector tracks and minimum ionizing energy in the calorimeter along a muon track were efficient methods for

distinguishing beam produced muons from cosmic ray muons. Therefore, an event in which neither muon track met either of these conditions had a high probability of originating from a cosmic ray muon. In order to be consistent the events in the second sample were also subjected to the standard mixing requirements involving invariant mass, opening angle, and muon P_T.

The normalized floating t_o distributions from muon tracks in cosmic ray sample one (solid line) and sample two (dotted line) are shown in the lower left plot of Fig. 5-6. The distributions from the two independent data samples exhibited good agreement which suggested that both were representative of the correct floating t_o distribution for muon tracks in cosmic ray events. The plot in the lower right hand corner of Fig. 5-6 shows the functional fit to the normalized distribution obtained from sample one.

5.4.3 Cosmic Background from Maximum Likelihood Fit

The number of events due to cosmic ray background in the final event sample was determined with a simultaneous maximum likelihood fit to the floating t_o distributions from the leading and trailing P_T muon tracks in the events. A detailed description of the maximum likelihood fit method is given in Appendix A. Since the fitted fractions of events from signal and background must add to one, the maximum likelihood fit used to determine the cosmic background was constrained with a single independent parameter. The input probability distributions for the floating t_o parameter in beam produced and cosmic ray events which were utilized in this particular fit were those obtained from the functional fits to the normalized distributions described in the previous section.

The result of the maximum likelihood fit to the 183 events in the final data sample is shown in Fig. 5-7. The combined floating t_o distribution for leading and trailing P_T muons in the sample is plotted with the indicated DØ data points.

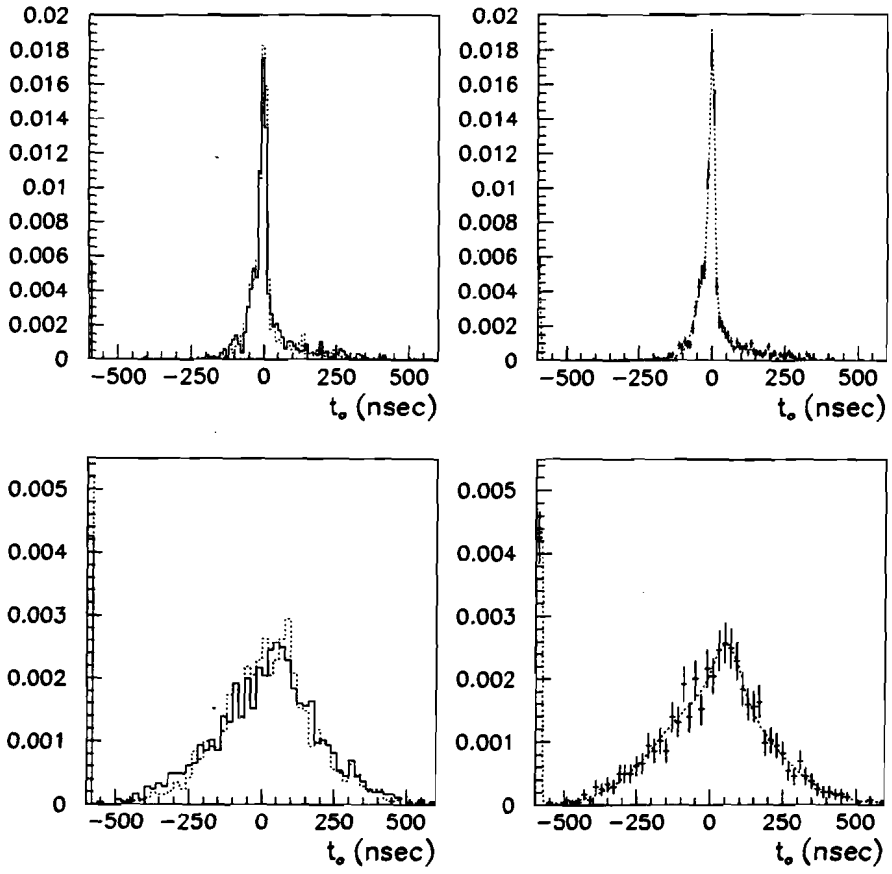

Figure 5-6: (Upper Left) Normalized t_o distributions from muons in good beam events determined from tight cuts on high mass QCD dimuon data [solid line] and J/ψ data [dotted line]. (Upper Right) Best fit to average of both normalized t_o distributions for good beam events determined from data. (Lower Left) Normalized t_o distributions from muons in cosmic ray events determined from cosmic ray data [solid line] and reversed cosmic cuts on high mass dimuon data [dotted line]. (Lower Right) Best fit to normalized t_o distribution for cosmic ray events determined from cosmic ray data.

Event Sample	Number of Events	Cosmic Ray Events
All Events	183	$13.4^{+8.2}_{-7.3}$
Like Sign Events	62	$13.1^{+5.5}_{-5.1}$
Unlike Sign Events	121	$1.7^{+5.4}_{-1.7}$

Table 5-3: Numerical results of maximum likelihood fits used to determine cosmic ray background in event sample.

The best fit to this distribution utilizing the input distributions for beam produced and cosmic ray events normalized to the relative contribution of each process as determined with maximum likelihood method is shown in solid. The individual contribution from beam produced and cosmic ray events are shown with the dotted and dashed lines respectively.

The numerical results of the maximum likelihood fit described in this section are shown in Table 5-3. The maximum likelihood fit method was performed on the inclusive final event sample as well as the like and opposite sign subsets of the sample. Once the number of cosmic ray background events in each of these samples was determined an explicit correction to the experimental parameter R could be made.

5.4.4 Cosmic Background from Event Scanning

A second method for determining the number of cosmic ray events in the final data sample was to scan the event displays of each event by eye and pick out those that had characteristics corresponding to cosmic ray background. This method was utilized as an independent consistency check to the more precise determination provided by the maximum likelihood fit method. Some examples of the criteria which were used to distinguish cosmic background events from signal events were the presence of extra hits in the central tracking and/or muon system which were

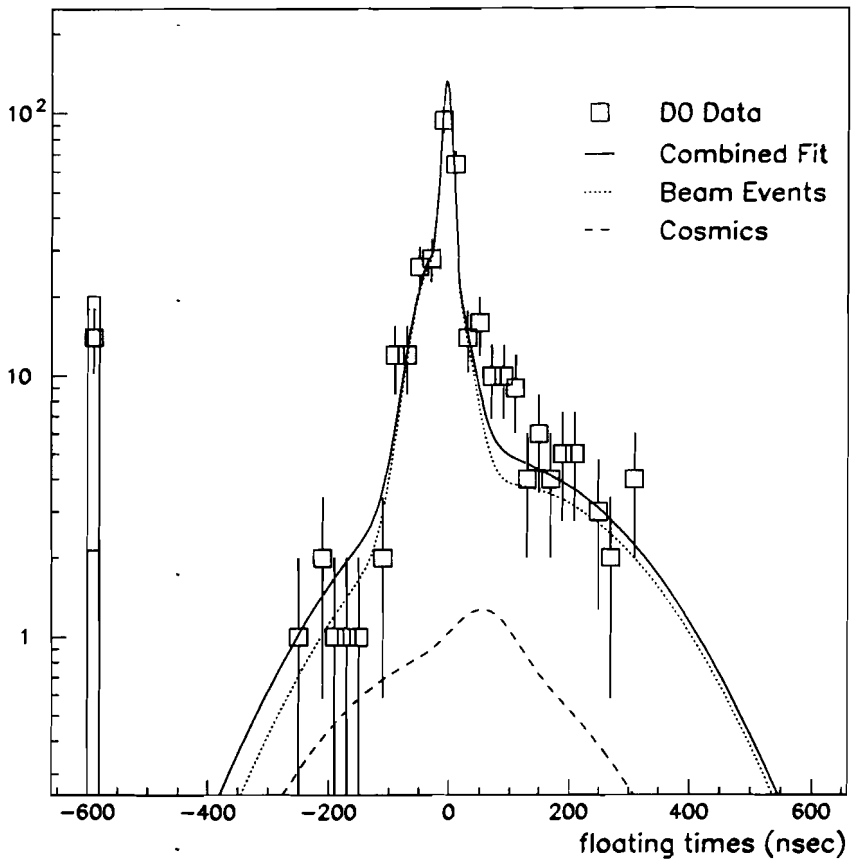

Figure 5-7: Result of simultaneous maximum likelihood fit to floating t_o distributions of leading and trailing P_T muons in final event sample.

Event Sample	Number of Events	Cosmic Ray Events
All Events	183	17 ± 10
Like Sign Events	62	10^{+2}_{-6}
Unlike Sign Events	121	7^{+8}_{-4}

Table 5-4: Numerical results of event scanning method used to determine cosmic ray background in event sample.

not consistent with a track reconstruction pointing to the event vertex, minimum energy deposition in a direction through the calorimeter which was not consistent with an associated reconstructed track, and the existence of hits and/or minimum ionizing energy in a region of the detector opposite to that of a reconstructed track which was suggestive of a continuation of that track through the detector.

Each event in the sample was separated into one of four different event categories based on the characteristics of the associated event displays. Two groupings were for clear-cut beam produced and cosmic ray events and the remaining two were reserved for less certain events of both types. The total number of good beam and cosmic ray events were determined by combining the number of events in the clear-cut and less certain categories of the particular event type. The errors associated with the total number of beam produced and cosmic ray events determined from this method were dependent on the number of events in the less certain categories of each event type. The results of the event scanning method are given in Table 5-4. The illustrated agreement in the cosmic ray background determination within the errors of the two methods provided an additional confirmation of the maximum likelihood fit method result.

5.4.5 Cosmic Background Correction to R

The dependence of the experimental parameter R on the amount of cosmic ray background in the final event sample was removed using the results of the maximum likelihood fits to the floating t_o distributions of muon tracks in the like and unlike sign subsets of the dimuon data sample. The removal of the cosmic ray background modified the value of the experimental parameter R given in Section 5.3 as shown:

$$R = \frac{49}{119} = 0.41 \pm 0.07(stat) \pm 0.05(sys). \tag{5.7}$$

The systematic error arises from the uncertainties associated with the maximum likelihood fits used to estimate the cosmic ray background as given in Table 5-3. In order to determine the combined statistical and systematic error in the value obtained for the experimental parameter R, the total error associated with the number of events in both the like and unlike samples was determined through the addition of statistical and cosmic ray background uncertainties in quadrature. The combined errors associated with the number of like and unlike sign muon events in the sample were then propagated through the calculation of R in the normal manner to determine the total error in R. The systematic error in R was chosen so that the addition of the systematic and statistical errors in quadrature matched the total error determined from this method.

Although the two methods utilized to determine the cosmic background were shown to agree within the associated uncertainties, the central values for the number of like and unlike sign events obtained from the two methods did in fact disagree significantly. The value of the experimental parameter R which was obtained using the results of the event scanning method to correct for cosmic ray background is $R = 0.46 \pm 0.08$ (stat) $\pm$ 0.04 (sys). Although the value for R shown here agrees well with that shown in (5.7) within the uncertainties of the two results, the central value obtained for mixing probability χ was found to have a corresponding

Production Mechanism	Fractional Contribution	Statistical Error
$b\bar{b} \rightarrow \mu\mu$	0.827	0.044
$c\bar{c} \rightarrow \mu\mu$	0.031	0.012
$b\bar{b} \rightarrow \mu$, $c\bar{c} \rightarrow \mu$	0.037	0.011
$b\bar{b} \rightarrow \mu$, $\pi/K \rightarrow \mu$	0.048	0.006
$c\bar{c} \rightarrow \mu$, $\pi/K \rightarrow \mu$	0.017	0.005
$\pi/K \rightarrow \mu$, $\pi/K \rightarrow \mu$	0.008	0.002
Drell-Yan ($\gamma^* \rightarrow \mu^+\mu^-$)	0.008	0.004
$\Upsilon \rightarrow \mu^+\mu^-$	0.024	0.011

Table 5-5: Monte Carlo predictions for the relative contribution of each dimuon production mechanism to the final event sample.

upward shift if the cosmic ray background corrections to R were based on the event scanning method.

5.5 Determination of χ

After correcting the experimental parameter R for the measured cosmic ray background, an extraction of the mixing probability χ was made using Monte Carlo predictions for the relative contribution of each dimuon production mechanism to the final event sample. The predicted fractional contribution of each production mechanism is shown in Table 5-5. A direct consequence of the event selection criteria is that over 80% of events in the final event sample are predicted to result from the decay of single $b\bar{b}$ quark pairs. Since the mixing signal is contained within this subset of events, the error in the measurement of the mixing probability χ was found to be significantly reduced through the minimization of the background contribution from production mechanisms other than the direct decays of $b\bar{b}$ quark pairs.

The further division of the fractional contributions from each production mech-

anism into the six categories (P1-P6) which affect the ratio of like to unlike sign events in the data sample was also required before an extraction of the mixing probability χ could be made. As detailed in Table 5-1, dimuon events produced in the decay of single $b\bar{b}$ quark pairs are separated into three categories (P1-P3) based on the number of muons in the pair which are produced in cascade decays of the individual b quarks. Since the sign of a muon produced in the cascade decay of a b quark is opposite to that of a muon produced in the direct semileptonic decay of the same quark, each of these three event categories has a different effect on the actual ratio of like to unlike sign events found in the final event sample.

The Monte Carlo prediction for the fractional contribution from each of the six event categories to the data sample was also dependent on the relative fraction of events associated with each of the different production mechanisms in which one muon track was reconstructed with an incorrect sign. Since the like to unlike sign ratios of these events are inverted with respect to the ratios of correctly reconstructed events, a separate classification of the predicted fractional contributions of these events to the final event sample was required. The Monte Carlo prediction for the relative percentage of events in the final data sample which arise from each of the six event categories which effect the ratio of like to unlike sign events in the sample is shown in Table 5-6.

A detailed description of the method utilized to determine the fractional contributions of the six event categories (P1-P6) to the final data sample as given in Table 5-6 from the different Monte Carlo samples discussed in Section 4.1 is presented here. In order to achieve the best possible model for events in the DØ detector, each Monte Carlo event was processed through the full DØ detector and trigger simulation packages. Version 11.19 of the full DØ event reconstruction package was used to provide the subsequent reconstruction of the simulated detector output in these events to be consistent with event reconstruction in the

Label	Primary Process	Fractional Contribution	Statistical Error
P1	$b \rightarrow \mu^-, \bar{b} \rightarrow \mu^+$	0.66	0.04
P2	$b \rightarrow c \rightarrow \mu^+, \bar{b} \rightarrow \mu^+$	0.14	0.02
P3	$b \rightarrow c \rightarrow \mu^+, \bar{b} \rightarrow \bar{c} \rightarrow \mu^-$	0.01	0.01
P4	$c \rightarrow \mu^+, \bar{c} \rightarrow \mu^-$	0.06	0.02
P5	$\pi/K \rightarrow \mu$ background	0.13	0.02
P6	-	0.00	0.00

Table 5-6: The relative fraction of events in the final event sample from each of the six event categories which effect the measured ratio of like to unlike sign events in the sample as determined from Monte Carlo.

data. As previously discussed the individual Monte Carlo events in each of the samples were assigned cross sectional weights which were chosen to normalize the total cross section associated with each of the Monte Carlo samples to the best possible measurement or calculation of the cross section for the modeled process. In order to determine the fractional contributions listed in Table 5-6, the cross sectional weight associated with each individual reconstructed Monte Carlo event which passed each of the event selection criteria utilized in this analysis was assigned to one of the six event categories. In order to account for the different integrated luminosities associated with the two trigger conditions utilized in this analysis, Monte Carlo events which were found to satisfy the requirements of the the Mu-1-Jet trigger but not those of the Mu-2-High trigger had their corresponding cross sectional weight reduced by a factor of 0.565. Since a prescale of one was utilized for the Mu-2-High trigger bit during the vast majority of data collection, each event which passed the criteria of this trigger was assumed to be collected into the sample. An average prescale of 1.77 was then assumed for events which only satisfied the criteria of the Mu-1-Jet to be consistent with the difference in integrated luminosity between the two trigger conditions as shown in Table 3-1. The combined cross sectional weight of all events assigned to a particular category

divided by the total weight of all Monte Carlo events which passed the event selection criteria of this analysis determined the fractional contribution of each category to the final data sample.

In order to assign individual reconstructed Monte Carlo events to one of the six specific event categories, the two leading P_T reconstructed muon candidates in each event were first matched to individual muons at the ISAJET event generation level. Once this correspondence was established, it was possible to identify the source of each reconstructed muon within an event using the parent particle information available at the event generation level. Muon sources were broken into five separate groups. Group A contained muons produced in the decay of b hadrons. Muons produced in the decay of c hadrons were subdivided into two separate groups. In cases where the c hadron was originally produced in the decay of a b hadron, the muon was placed in group B. Otherwise, the muon was placed in group C. In addition, muons produced in the in-flight decays of pions and kaons were placed in group D, and muons produced in Drell-Yan processes were placed in group E. A classification of each Monte Carlo event could then be made based on the sources of the two reconstructed muons within the event. For example, events with one group A muon and one group B muon were candidates for inclusion in P2.

It was also important to check, however, that the combination of the reconstructed muon signs in each event was consistent with the sign combination expected for each muon pair based on the muon sources. Since the mixing process is not modeled in the ISAJET event simulation, an event consistent with the above example was expected to produce a like sign event. However, a small fraction of these events were in fact found to contain reconstructed muon tracks with opposite signs. A significant percentage of these opposite sign events were due to an incorrect sign reconstruction of one muon track within the event. However, events of this type were also found to result from the production of multiple $b\bar{b}$ quark pairs

Muon Sources	Expected Sign Combination	Category (Correct Sign)	Category (Incorrect Sign)
A,A	Unlike	P1	P2
A,B	Like	P2	P1
B,B	Unlike	P3	P2
A,C	50/50	P5	P5
B,C	50/50	P5	P5
C,C	Unlike	P4	P6
A,D	50/50	P5	P5
B,D	50/50	P5	P5
C,D	50/50	P5	P5
E,E	Unlike	P4	P6

Table 5-7: A guide to the prescription followed for assigning the cross sectional weight of individual Monte Carlo events to the six different events categories utilized in this analysis.

within a single $p\bar{p}$ interaction. In cases where both a group A muon and a group B muon were produced in the decays of identical flavor bottom quarks originating from different $b\bar{b}$ pairs, opposite sign events were also obtained. Events of this type were classified as P1 rather than P2 since the like and unlike sign fractions of these events in the final data sample were consistent the fractions defined for this category.

A more complete guide to the classification of Monte Carlo events into the six event categories (P1-P6) which were utilized in this analysis is presented in Table 5-7. Since each combination of muon sources corresponds to a specific dimuon production mechanism, an event in which the expected sign combination was obtained from the reconstructed muon pair within the event were categorized into P1-P6 as illustrated in Table 5-1. However, in cases where the reconstructed sign combination was inconsistent with that expected for the particular production mechanism associated with a given combination of muon sources, a classification of the event was chosen in which the fractions of like and unlike events in the

chosen category were opposite to those associated with the original production mechanism.

The value of the mixing probability χ which was extracted from the corrected value of the experimental parameter R given in (5.7) using the Monte Carlo results for the fractional contributions of P1-P6 as given in Table 5-6 is

$$\chi = 0.09 \pm 0.04(stat) \pm 0.03(sys). \tag{5.8}$$

The systematic error in this result is restricted to the combination of the uncertainties in the determination of the cosmic ray background and the statistical errors associated with the Monte Carlo sample. The statistical error associated with the combined cross sectional weight of all events assigned to a particular category was calculated as the square root of a sum over the squares of the individual event cross sectional weights. A simple determination of the corresponding errors in the predicted fractional contributions of the six event categories to the final data sample could then be made simply by dividing the calculated uncertainty in the total cross sectional weight of each category by the combined cross sectional weight of all Monte Carlo events which pass the selection criteria of this analysis.

5.6 Stability of Result

Since the Monte Carlo model for the relative contributions of the different dimuon production mechanisms to the final event sample completely determined the value which was obtained for the mixing probability χ, a large number of consistency checks between the data and Monte Carlo were required to validate this model. Studies of the potential range of disagreement between Monte Carlo and data which were utilized to assign systematic errors to the result for the mixing probability χ are discussed in the following chapter.

An important consistency check of the Monte Carlo model can also be made by

varying the parameters of the event selection criteria which define the final event sample and checking for stability in the values obtained for the mixing probability χ. Although both the Monte Carlo predictions for the relative contributions of the six dimuon event categories to the final data sample and the value which is obtained for the experimental parameter R are found to fluctuate as a function of the event selection criteria, the value of the mixing probability χ which is obtained from these parameters should be independent of these changes. Therefore, an important test of the Monte Carlo model utilized in this analysis was to check the magnitude of the variations in the value obtained for χ as a function of the different selection criteria used to define the event sample.

The plots in Fig. 5-8 illustrate the stability in the obtained result for the mixing probability χ as a function of the imposed lower limit on different kinematic cuts utilized in this analysis. As discussed in Section 5.2 lower cuts on the transverse momentum of muons relative to their associated jet axes or on the actual transverse momentum of reconstructed muon tracks increase the fraction of muons in the sample which are produced in the decay of c quarks and π/K decays. The modification of these event selection parameters has a substantial effect on both the value of the experimental parameter R and the Monte Carlo predictions for the relative fractions of the contributing processes. However, as shown in Fig. 5-8 the values which were obtained for χ as a function of variable lower limits on both the muon-jet P_T^{rel} cut and the muon P_T cut were consistent within the errors of the measurements.

The variation in the value obtained for the mixing probability χ was also studied as a function of the lower limit imposed on reconstructed jet E_T. Since a large fraction of the jets associated with muons produced in the decay of heavy quarks are found in a transverse energy range consistent with the turn on region for jet reconstruction efficiency, the utilization of low cuts on reconstructed jet E_T

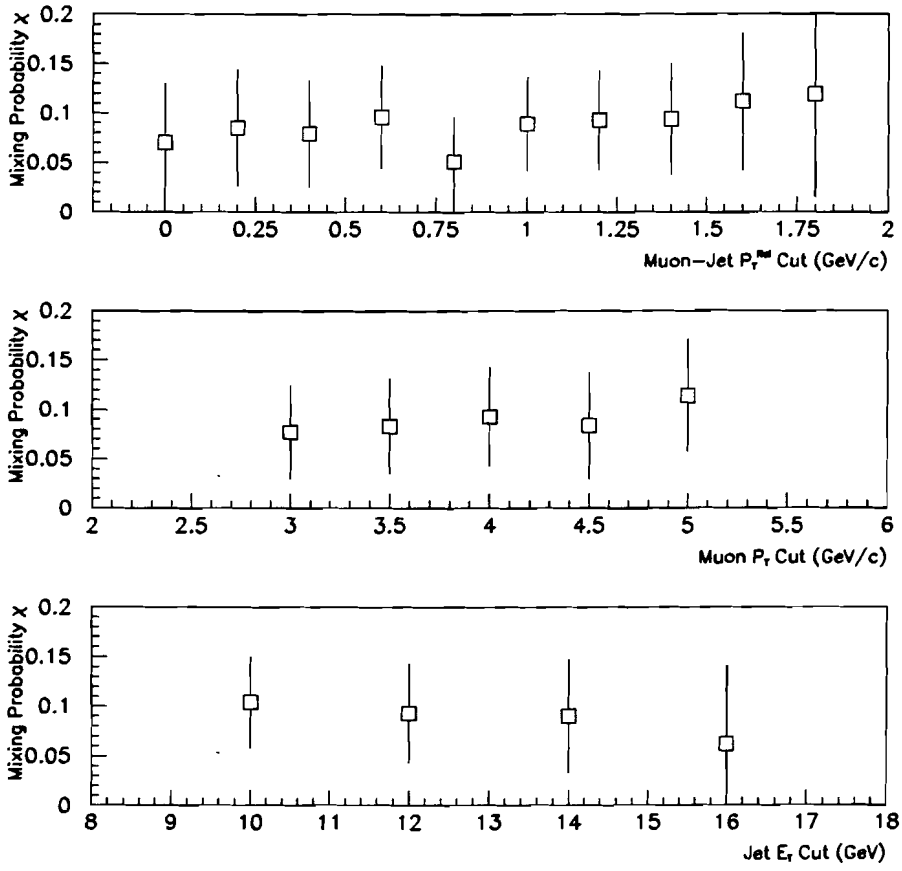

Figure 5-8: Obtained values for the mixing probability χ as a function of the imposed lower limit on different kinematic cuts utilized in this analysis.

Cosmic Cuts	R	R (Cosmic Background Subtracted)	χ
Loose	$.64 \pm .07$	$.39 \pm .08$	$.09 \pm .05$
Medium	$.51 \pm .08$	$.41 \pm .08$	$.09 \pm .05$
Tight	$.32 \pm .09$	$.32 \pm .10$	$.07 \pm .06$

Table 5-8: Obtained values for the mixing probability χ utilizing the different sets of cuts for rejecting cosmic ray events as defined in table 3-2.

required an effective Monte Carlo model of this region in order to extract the correct relative fractions of the different dimuon production mechanisms. As shown in Fig. 5-8 the result obtained for χ was in fact consistent over a range of lower limits on reconstructed jet E_T which provided further confirmation of the Monte Carlo model.

The value obtained for the mixing probability χ was also cross checked using each of the different combinations of cosmic cuts defined in Table 3-2. The resulting values of χ which were obtained for each set of cuts are shown in Table 5-8. The consistency of the final result between the three sets of cuts provides further confirmation of the maximum likelihood fit method which was utilized to extract the cosmic ray backgrounds.

Chapter 6

Error Analysis

Since a measured value of the mixing probability χ is directly dependent on a Monte Carlo determination of the relative contributions of the different dimuon production processes to the final event sample, the parameters of the Monte Carlo which effect these fractions had to be crossed checked against the data. In general, the parameters of the Monte Carlo utilized in this analysis were modified to provide the best possible match to experimental data. The uncertainties associated with the experimental results which were used to set the parameters of the Monte Carlo determined the systematic errors in the relative fractions of the different processes contributing to dimuon production. In the following sections descriptions of the uncertainties associated with each of the different Monte Carlo parameters are presented. The calculation of the specific systematic errors which were assigned to the Monte Carlo predictions for the relative contributions of the six different categories of dimuon events which define the ratio of like to unlike sign events in the sample is discussed in the later part of the chapter.

6.1 Fraction of Muons from b,c, and π/K Decays

In order to extract an accurate value of the mixing probability χ from a measured value of the experimental parameter R, the Monte Carlo prediction for the relative

fractions of contributing processes to dimuon production with our selection cuts must be in good agreement with the actual fraction of these processes in the data. This is true not only for the fractions of dimuon events from $b\bar{b}$ production (P1-P3) but also for the fractions of background events as well. As shown in Table 5-5 the two most significant background processes to dimuon production from $b\bar{b}$ pairs are production from $c\bar{c}$ pairs and events in which at least one muon is produced from an in-flight π/K decay. Since the fractions of like and unlike sign events associated with these background processes are significantly different, the relative contributions of these production mechanisms to the dimuon event sample must also be correctly modeled in order to obtain an accurate result for the mixing probability χ.

An inclusive single muon data sample was utilized to provide a cross check between a Monte Carlo prediction for the relative fractions of muons in the event sample from b quark, c quark, and π/K decays and the observed fractions in the data [36]. The comparison between data and Monte Carlo was restricted to muon tracks in the rapidity range where $|y_\mu| < 0.8$ which is consistent with the region utilized in this analysis. The fraction of single muon events in the data sample which were the result of b quark decays (f_b) was determined using a maximum likelihood fit to the P_T^{rel} spectrum of muon tracks in those events as defined in Section 5.2.3. Since the P_T^{rel} variable is only defined for muon candidates with an associated jet, the fits were further restricted to the 60% of events in the sample which were found to have a reconstructed jet with $E_T > 8$ GeV within $\Delta R^{\mu-jet} = 1.0$ of the reconstructed muon track. The fraction f_b which was extracted from this subset of events was in fact assumed to be valid for the entire sample since the kinematic distributions for muons with and without associated jets were found to be nearly equivalent.

The different P_T^{rel} distributions for muons produced in the decay of b quarks,

c quarks, and π/K decays were modeled using single muon Monte Carlo events generated with version 7.0 of the ISAJET event simulation package and CTEQ2L parton distributions. In addition, both leading and higher order heavy quark production processes were included in the simulation of these single muon events. The P_T^{rel} distribution for muons produced in b quark decays included both direct semileptonic decays ($b \rightarrow \mu$) and cascade decays ($b \rightarrow c \rightarrow \mu$) where the relative contribution of each decay chain was chosen to be consistent with the most recent measurements of the branching ratios [45]. The resulting P_T^{rel} spectrum for muons produced in b quark decays was additionally checked against an equivalent distribution for leptons measured by the OPAL collaboration [46] at LEP and found to be in good agreement. Although the P_T^{rel} spectra for muons produced in the decay of b quarks were not expected to be identical in event samples obtained at LEP and the Tevatron due to differences in the hadron mixtures produced at the two colliders, the magnitude of the discrepancy in the shapes of the two curves was thought to be small enough that the comparison described above did in fact provide a valuable test of the Monte Carlo model.

The single muon data was separated into six P_T^{μ} bins, and f_b was independently determined for each bin by fitting the b quark, c quark, and π/K P_T^{rel} spectra to the data. As an example, the result of the maximum likelihood fit to the P_T^{rel} distribution of single muon candidates in the P_T^{μ} range between 8-30 GeV/c is illustrated in Fig. 6-1. The dotted line shows the P_T^{rel} spectrum associated with the fitted contribution of muons produced in the decay of b quarks, and the dashed line shows the P_T^{rel} spectrum which results from the sum of the fitted contributions from muons produced in c quark and π/K decays. The P_T^{rel} spectrum which represents the sum of all fitted contributions is shown with the solid line and is in good agreement with the measured spectrum from the data.

A comparison between the values of f_b obtained from the fits to the data sample

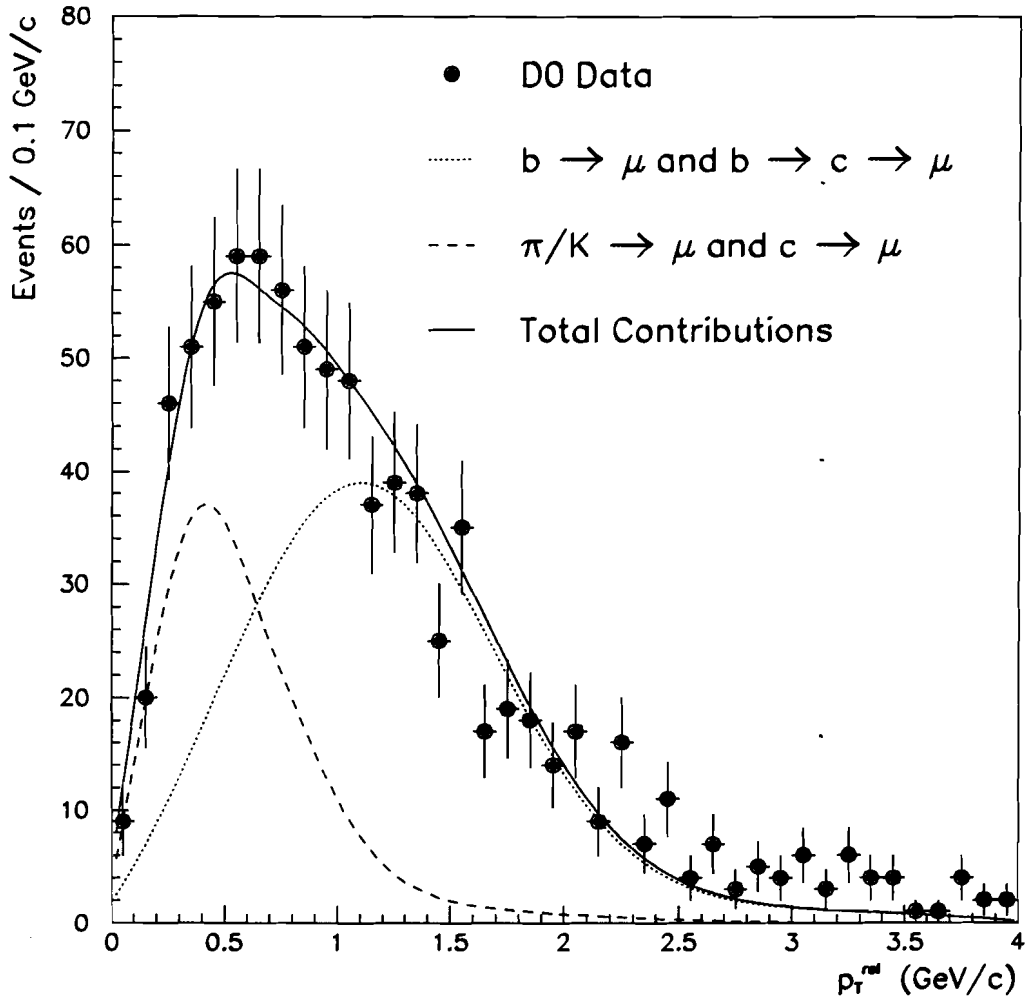

Figure 6-1: Graphical illustration showing the fitted contributions of muons from b quark, c quark, and π/K decays determined from a maximum likelihood fit to the P_T^{rel} spectrum of single muon events. The single muon data sample is restricted to the subset of events with reconstructed associated jets where 8 GeV/c $< P_T^{\mu} <$ 30 GeV/c and $|y^{\mu}| < 0.8$ [36].

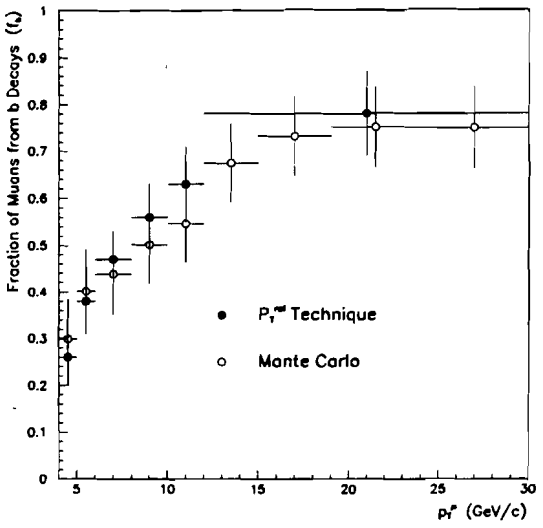

Figure 6-2: f_b plotted as a function of P_T^μ where the solid points were obtained from maximum likelihood fits to the P_T^{rel} distribution from single muon events in the data and the open circles were obtained from ISAJET Monte Carlo as described in the text [36].

and the Monte Carlo predictions for these values is shown in Fig. 6-2. The Monte Carlo predictions for f_b demonstrate good agreement with the measured values within both the errors of the fit method and the Monte Carlo uncertainty. The heavy quark cross sections associated with the event samples used to determine the Monte Carlo predictions for the relative contributions of the different muon sources to the single muon sample were normalized to the previously discussed NLO perturbative QCD calculations of Nason, Dawson, and Ellis [38] in a manner consistent with that utilized for the dimuon Monte Carlo event samples used in the mixing analysis. The errors in the values of f_b obtained from the data were estimated by varying the input P_T^{rel} distributions from the different muon sources within their errors and repeating the fits to determine the resulting spread in the f_b parameter. The resulting errors on f_b from the data were estimated to be on the order of 12%.

Since the P_T^{rel} distribution for muons produced in the decay of c quarks is nearly identical to that for muons produced in π/K decays, it is not possible to extract the relative contributions of muons from these sources in the data sample using the fit method described here. In fact, no kinematic event variable which could help to separate muons from these two sources was found. Therefore, it was necessary to estimate the uncertainties associated with the relative contributions of muons from these sources using other information. As described below the uncertainty in the Monte Carlo prediction for the relative contribution of muons from in-flight decays of pions and kaons was well constrained by experimental measurements of the inclusive charged hadron spectrum at the Tevatron [40] in conjunction with measurements of the relative fractions of pions and kaons in the charged particle spectrum obtained from experiments at lower collision energies [23]. Once the uncertainties associated with the relative contributions of muons from b quark decay and π/K decays were determined, the remaining fraction of muons was constrained to c quark production within the combined uncertainties of the other muon sources.

The transverse momentum spectrum of charged particles in ISAJET Monte Carlo events generated using CTEQ2L parton distributions was compared to a measurement of the inclusive charged hadron spectrum made by the CDF collaboration at the Tevatron [41]. The level of agreement between the two distributions was found to lie within an uncertainty range of 20%. Since the muon branching ratios for decays of pions and kaons are well determined, the only additional source of error in the Monte Carlo prediction of the in-flight muon decay spectrum is due to uncertainties in the relative fractions of pions and kaons in the inclusive charged hadron spectrum. The charged pion and kaon fractions inherent to the ISAJET event simulation were determined to be 0.73 ± 0.05 and 0.18 ± 0.05 [41]. A comparison of these predictions with experimental results from the $Sp\bar{p}S$ collider at

CERN and Fermilab E605 was used to establish the uncertainty range associated with these parameters [41]. However, since the predicted rate of muons from π/K decays was found to be relatively insensitive to these fractions, the added uncertainty in the total rate was found to be only 8%. The combined uncertainty in the rate of muons from in-flight decays of pions and kaons was determined to be 22%.

6.2 Muon Branching Ratios

In the previous section it was shown that the Monte Carlo prediction for the relative fraction of single muon events from the decay of $b\bar{b}$ quark pairs was in good agreement with a measurement of the same fraction from the data. However, as discussed in Section 5.1 and Section 5.5 dimuon events which are produced in the decay of single $b\bar{b}$ quark pairs can be further subdivided into three separate event categories (P1-P3) with distinct fractions of like and unlike sign events which depend on the exact value of the mixing probability χ. Therefore, the relative contribution of events from each of these categories to the data sample must also be well determined in order to extract an accurate value of χ from a measurement of the experimental parameter R.

Since the three classifications for dimuon events produced in the decay of $b\bar{b}$ quark pairs are distinguished by the number (zero to two) of muons which are produced in cascade decays of the individual b quarks rather than in the direct semileptonic decay of the quarks, the relative contribution of events from each of these categories is directly related to the branching ratios of the two decay modes. The b quark direct semileptonic branching ratio utilized in the Monte Carlo was matched to experimental results from the LEP experiments [47] which also observe $b\bar{b}$ quark pairs produced above the b production threshold energy. Since the b quark semileptonic branching ratio is weakly dependent on the relative populations of the different hadrons which are produced in b quark fragmentation, the LEP results

provide the best possible match to the true semileptonic branching ratio for the mixture of b hadrons produced at Tevatron energies. The most recent average of the experimental results from LEP [45] is

$$BR(X_b \rightarrow X\ell^+\nu_\ell)\% = 11.0 \pm 0.3 \pm 0.4. \tag{6.1}$$

Since the b quark semileptonic branching ratio in the ISAJET simulation package used to generate the Monte Carlo samples utilized in this analysis was set to 12.1%, the cross sectional weight of each dimuon Monte Carlo event was reduced by a factor of 0.909 for each of the muons within the event which was found to result from the direct semileptonic decay of a b quark. The net result of applying these correction factors was to match the b quark direct semileptonic branching ratio in the Monte Carlo to the value obtained from the LEP measurements as given in (6.1). The 5% uncertainty assigned to the result in (6.1) was then used to calculate the corresponding systematic errors in the Monte Carlo predictions for the relative contributions of the six dimuon event categories to the final data sample.

Since a c hadron is produced in nearly 100% of b hadron decays, the production of a muon through the cascade decay of b quark has a branching ratio which is roughly equivalent to the c quark direct semileptonic branching ratio. The most recent measurements of this branching ratio were made by the Argus collaboration [48]. The branching ratio was determined from the excess of correct sign over incorrect sign muons observed in an event sample tagged by fully reconstructed $D^*(2010)^+ \rightarrow D^\circ\pi^+$ decays. Since the mixture of charmed particle decay parents for the observed muons in this event sample was undetermined, the actual c quark semileptonic branching ratio for the mixture of charmed hadrons produced at Tevatron energies may differ slightly. The average value of this branching ratio based

on the combination of the Argus result with several similar measurements [45] is

$$\frac{\Gamma(c/\bar{c} \rightarrow \mu^+ X)}{\Gamma(c/\bar{c} \rightarrow X)} = 0.081^{+0.010}_{-0.009}. \tag{6.2}$$

Since the c quark semileptonic branching ratio in the ISALEP simulation package used to generate the Monte Carlo events utilized in this analysis was initially set to the value in (6.2), no additional correction to the cross sectional weights of these events based on the value of this parameter was required. The 12% error associated with this measurement was used to calculate the corresponding systematic errors in the Monte Carlo predictions for the relative contributions of the six dimuon event categories to the final data sample.

6.3 Multiple Heavy Quark Pairs

Multiple heavy quark pairs can be created in a small fraction of the interactions in which heavy flavor is produced. An example of a process in which multiple heavy quark pairs are produced is shown in Fig. 6-3. Both of the final state gluons in this event fragment into heavy quark pairs. Dimuon events which are produced from this type of interaction present an additional complication in the determination of the mixing probability χ since the parent quarks of the two reconstructed muon candidates are uncertain. In the case of the interaction shown in Fig. 6-3, a pair of muon candidates would have six potential combinations of quark parents ($b\bar{b}$, $c\bar{c}$, bc , $b\bar{c}$, $\bar{b}c$, and $\bar{b}\bar{c}$). As discussed in Section 5.5 interactions such as the one illustrated in Fig. 6-3 can also produce multiple heavy quark pairs of identical flavor. Unlike dimuon events which result from interactions in which both bottom and charm quark pairs are produced, however, events associated with these processes were found to make only a minimal contribution to the final dimuon sample. Therefore, the discussion in this section is restricted to those dimuon events in which the two muons result from the decay of both $b\bar{b}$ and $c\bar{c}$

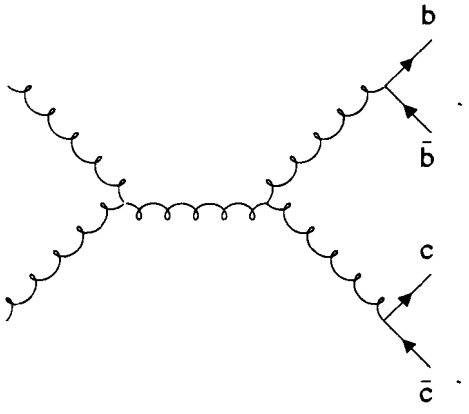

Figure 6-3: Feynman diagram of a gluon splitting event in which multiple heavy quark pairs are produced.

quark pairs within a single interaction. Since the quark parent combinations which contain one charmed quark and one bottom quark produce dimuon events with a like sign to opposite sign ratio different from that of those produced in the decays of single heavy quark pairs, the relative fraction of these events in the data must also be understood in order to extract an accurate value of χ from the experimental parameter R.

Unfortunately, the identification of events which result from this type of interaction is very difficult experimentally. Since both muons are produced in the decays of heavy quarks, the kinematic properties of the resulting muons are the same as those of muons which are produced in decays of single heavy quark pairs. However, interactions which produce multiple heavy quark pairs are just one of a small number of sources of three muon events. Therefore, the number of events in the dimuon data sample in which a third muon candidate was reconstructed could potentially be used to help constrain the maximum potential contribution

of multiple heavy quark pair events to the final data sample. Out of the combined total of 183 events in the data sample, two events were found with an additional reconstructed muon in the pseudorapidity range $|\eta_\mu| < 0.8$. Since the event displays associated with each of these events were consistent with beam produced events, the resulting fraction of three muon events in the final data sample was determined to be $2/169 = 0.012 \pm 0.008$.

The production of three muon events is not limited to interactions in which multiple heavy quark pairs are produced, however. Since each individual bottom quark has the ability to produce two muons through either the production and subsequent decay of a J/ψ or the formation of single muons in both the direct semileptonic and subsequent cascade decays of the quark, three muon events can also be produced in the decays of single $b\bar{b}$ pairs. Although no three muon events resulting from interactions containing multiple heavy quark pairs were found in the Monte Carlo sample, the Monte Carlo prediction for the fraction of three muon events in the final data sample (0.017 ± 0.006) did in fact agree with the measured fraction in the data. Since the fraction of three muon events in the data sample was consistent with both the model for multiple heavy quark pair production in the ISAJET simulation package and a model including no heavy quark pair production, no limits could be placed on the magnitude of these processes using a comparison of three muon events in data and Monte Carlo.

An additional study was performed to check whether the Monte Carlo prediction for the relative contribution of dimuon events to the final data sample from interactions containing multiple heavy quark pairs was consistent with a simple model of the probabilities for observing two muons in both single and multiple quark pair events. As discussed in Section 4.1.1 the dimuon Monte Carlo event sample utilized in this analysis was generated using a modified form of the ISAJET simulation package referred to as ISALEP. Since these modified routines were uti-

lized, it was at least possible that the generated dimuon Monte Carlo events in which the two muons were found to result from the decay of different heavy quark pairs were the result of a bias in the modified routine. In order to confirm the validity of these events, a set of quark level Monte Carlo events unbiased with respect to muon production were generated using the basic ISAJET package. These events were then utilized to determine the ISAJET prediction for the fraction of Monte Carlo heavy flavor events which contain multiple heavy quark pairs. In addition, a simple model of the efficiencies for producing dimuon events from both single and multiple heavy quark pairs was then utilized to check if the predicted contribution of multiple heavy quark pair events to the final data sample as determined from the dimuon Monte Carlo sample was consistent with the ISAJET prediction described above. The numerical results of this study which is described in greater detail below are summarized in Table 6-1.

As indicated in Table 6-1 the ISAJET event simulation package predicts that when no transverse momentum or pseudorapidity restrictions are placed on heavy quark production 1% of interactions which produce $b\bar{b}$ quark pairs also contain an associated $c\bar{c}$ quark pair. Since greater than 95% of all heavy quarks which produce muons with $P_T^{\mu} > 3$ GeV/c in the pseudorapidity region $|\eta_{\mu}| < 0.8$ are found themselves to lie in the pseudorapidity range $|\eta_q| < 1.2$ and to have $P_T^q > 4$ GeV/c, the subset of heavy quarks which have the ability to produce muons in the kinematic ranges of this analysis can be roughly approximated with these cuts. As shown in Table 6-1 the relative number of events which contain both charm and bottom quarks within these kinematic cuts with respect to those which contain a $b\bar{b}$ pair is roughly 2.5%. This fraction is larger than the original percentage of events with multiple heavy quark pairs since the probability for finding two quarks within the restricted kinematic region is substantially higher for events with more than one quark pair.

Monte Carlo	Cuts	Multiple Quark Pair Fraction
Unbiased Quark Sample	No Cuts	$\frac{\sigma(b\bar{b}+c\bar{c})}{\sigma(b\bar{b})} = 0.0097 \pm 0.0005$
Unbiased Quark Sample	$\lvert\eta_q\rvert < 1.2$ and $P_T^q > 4$ GeV/c	$\frac{\sigma(bc,b\bar{c},\bar{b}c,\bar{b}\bar{c})}{\sigma(b\bar{b})} = 0.023 \pm 0.003$
Unbiased Quark Sample	Account for Muon Branching Ratios	$\frac{\sigma(bc,b\bar{c},\bar{b}c,\bar{b}\bar{c} \rightarrow \mu\mu)}{\sigma(b\bar{b} \rightarrow \mu\mu)} = 0.028 \pm 0.004$
Dimuon Sample	$\lvert\eta_\mu\rvert < 0.8$ and $P_T^\mu > 3$ GeV/c and $M_{\mu\mu} > 6$ Gev/c^2	$\frac{\sigma(bc,b\bar{c},\bar{b}c,\bar{b}\bar{c} \rightarrow \mu\mu)}{\sigma(b\bar{b} \rightarrow \mu\mu)} = 0.028 \pm 0.003$
Dimuon Sample	All Analysis Cuts	$\frac{\sigma(bc,b\bar{c},\bar{b}c,\bar{b}\bar{c} \rightarrow \mu\mu)}{\sigma(b\bar{b} \rightarrow \mu\mu)} = 0.056 \pm 0.016$

Table 6-1: Results of a Monte Carlo study on the contribution of multiple heavy quark pair events to the dimuon sample relative to events produced from single $b\bar{b}$ quark pairs. Errors are statistical only.

An approximation of the relative fraction of dimuon events produced in the decay of heavy quark pairs which contain both charm and bottom quarks with respect to those produced in the decay of single $b\bar{b}$ pairs was made by weighting events in the quark level Monte Carlo based on the semileptonic branching fractions of each heavy quark found within the kinematic region described above. In events where more than two heavy quarks were found within this kinematic region, each quark pair was assigned a probability for dimuon production. Since the c quark semileptonic branching ratio is lower than that for the b quark, the dimuon branching fraction for quark pairs which contain both charm and bottom quarks is slightly smaller than that for single $b\bar{b}$ pairs. However, since the events which contain both bottom and charm quarks must originate from interactions in which multiple heavy quark pairs are produced, a larger fraction of these events have more than two quarks within the allowed kinematic region, and hence the dimuon branching fraction for this event subset is increased. The net result of these two effects is that the fraction of dimuon events expected from quark pairs which contain both charm and bottom quarks with respect to those expected from single $b\bar{b}$ pairs is found to be 2.8%.

As shown in Table 6-1 this approximated dimuon event fraction is in good agreement with a determination of the same fraction from the dimuon Monte Carlo sample utilized in this analysis. The best agreement was obtained with a minimal set of cuts on the dimuon Monte Carlo which restrict muons to a kinematic region consistent with the allowed kinematic range of heavy quarks in the previously discussed approximation. This fraction was found to be about a factor of two larger when the complete set of cuts utilized in this analysis was applied to the dimuon Monte Carlo, although the statistical size of the event sample was much smaller. Since the predicted contribution of dimuon events from multiple heavy quark pair events to the final event sample was found to be consistent between the

two Monte Carlo samples, the principal uncertainty associated with these events was determined to stem from the Monte Carlo prediction for the fraction of $b\bar{b}$ producing interactions which also produce associated $c\bar{c}$ pairs. A systematic error of 50% is assigned to the Monte Carlo prediction for the relative contribution of events containing multiple heavy quark pairs to the dimuon event sample since the cross section for these events is dependent on the product of two branching fractions for the decay of final state gluons into heavy quark pairs, neither of which is well determined.

6.4 Incorrect Sign Muon Track Reconstructions

The percentage of dimuon events in which one muon track is reconstructed with an incorrect sign is another important Monte Carlo parameter required to extract the mixing probability χ from the ratio of like sign to opposite sign events in the dimuon data sample. Since events in which one muon is assigned an incorrect sign will have an opposite like to unlike sign ratio to that which would be expected based on the event production mechanisms, the relative fraction of these events in the final event sample can have a significant effect on the measured value of the experimental parameter R.

As discussed in Section 3.2.1 the percentage of correct sign muon track reconstructions was determined as a function of reconstructed track P_T using single muon Monte Carlo events. These events were subjected to the MUSMEAR package as described in Section 4.2 which simulated individual chamber hit efficiencies and resolutions based on measurements utilizing muon tracks in the data. Since the Monte Carlo prediction for the percentage of wrong sign muon track reconstructions is directly related to the parameters of this package, the uncertainties associated with these parameters directly influence the uncertainties in the Monte Carlo prediction for the number of events in the final dimuon sample with one

incorrect sign reconstruction.

In order to reduce this uncertainty range, a comparison was made between the Monte Carlo prediction for the percentage of dimuon events produced in Υ decays and Drell-Yan processes which were reconstructed with like signs and equivalent percentages from the data. Since like sign dimuons from Υ decays and Drell-Yan production are found only in events where one muon is reconstructed with an incorrect sign, this comparison provided an excellent test of the Monte Carlo prediction for the percentage of muons with misreconstructed signs. The relative number of like and opposite sign dimuon events for these processes in the data was determined from maximum likelihood fits to an isolated, high mass subset of the DØ data sample [39]. The relative contributions of Υ decays, Drell-Yan production, cosmic ray events, and non-isolated QCD production to this data sample were determined by performing a simultaneous fit to the invariant mass, muon isolation, and floating t_o distributions associated with these events. The results of these fits to both the like sign and opposite sign dimuon samples are shown in Table 6-2. The Monte Carlo prediction for the number of like sign events associated with both Υ decays and Drell-Yan production based on the magnitude of the opposite side samples is also given for comparison.

The Monte Carlo prediction for the number of like sign events in these samples is found to agree with the number of events obtained from the data within the errors of the fits. However, the error ranges associated with these fits are relatively large with respect to the actual number of like sign events observed. In fact, the uncertainty range which was assigned to the Monte Carlo prediction for the fraction of reconstructed tracks with an incorrect sign could only be reduced to roughly 50% based on the combined results.

Process	Unlike Sign Events (Data)	Like Sign Events (Data)	Like Sign Events (Monte Carlo)
Υ	90 ± 11	3^{+4}_{-1}	1.8 ± 0.4
Drell-Yan	31^{+11}_{-10}	0^{+4}_{-0}	0.8 ± 0.5
Cosmic	8^{+6}_{-5}	15 ± 5	-
QCD	120^{+13}_{-14}	55^{+5}_{-7}	-

Table 6-2: Number of like sign and opposite sign events in the DØ isolated, high mass dimuon data sample associated with each dimuon production mechanism obtained from fits to the data. The Monte Carlo prediction for the number of like sign events based on the magnitude of the unlike sign sample is shown for comparison.

6.5 Jet Trigger Efficiency

As discussed in Section 4.3.2 a measurement of the Level 1 jet trigger efficiency made from a sample of unbiased jet data was shown to disagree with that determined from Monte Carlo events. Since 63 of the 183 events in the final data sample were collected exclusively with the Mu-1-Jet trigger bit which does include a Level 1 jet requirement, the effect of this discrepancy on the Monte Carlo prediction for the relative contributions of the different dimuon production mechanisms to the final event sample also had to be considered. As illustrated in Fig. 4-10 the Level 1 jet trigger efficiency in the Monte Carlo could be matched to the measured efficiency in the data by increasing the minimum energy which was required within a single calorimeter trigger tower in order to produce a Level 1 trigger. The systematic errors which were assigned to the Monte Carlo predictions for the relative contribution of events from each of six dimuon event categories based on the discrepancy in jet trigger efficiency between data and Monte Carlo were determined from the difference in the predicted values of each fraction obtained from corrected and uncorrected Monte Carlo.

6.6 Υ and Double Decay Monte Carlo

Since a complete event simulation was not available for generating dimuon events which are produced in the decay of bottomonium states or events in which both muons are produced from the in-flight decays of pions or kaons, larger uncertainties were associated with the Monte Carlo predictions for the relative contribution of these processes to the final event sample. These larger uncertainties result from the fact that energy deposition in the calorimeter was not properly modeled for either of these production mechanisms. The effect of cuts which involved calorimeter parameters on dimuon events which were produced in the decay of bottomonium states was assumed to be identical to the effect of the same cuts on Drell-Yan dimuon events. Similarly, the effect of these cuts on dimuons produced in the in-flight decays of two light mesons was determined using a sample of dimuon events which contained one muon produced in the decay of a c quark and another from the in-flight decay of a pion or kaon. An additional error of 50% was assigned to the Monte Carlo predictions for the relative contributions of these processes to the final event sample to account for the additional uncertainties associated with these assumptions.

6.7 Calculation of Systematic Errors

Once the uncertainties associated with each of the different Monte Carlo parameters were determined, corresponding systematic errors on the predicted relative contributions of the six dimuon event categories to the final data sample could be calculated. The technique utilized to determine these systematic errors is outlined in the remainder of this section. The effect of the uncertainty ranges associated with each of the various Monte Carlo parameters on the predictions for the relative contributions of the six event categories to the final data sample was studied

Error Type	P1	P2	P3	P4	P5	P6
BR($b \rightarrow \mu$)	.015	.003	.001	.006	.006	.000
BR($c \rightarrow \mu$)	.020	.009	.003	.006	.003	.000
Incorrect Sign ID	.004	.004	.000	.003	.000	.003
Multiple $b\bar{b}$,$c\bar{c}$ Pairs	.013	.003	.000	.001	.017	.000
f_b	.008	.002	.000	.008	.002	.000
f_c	.025	.005	.001	.010	.019	.000
f_{dec}	.012	.003	.000	.001	.016	.000
MC Jet Trigger	.002	.005	.001	.007	.001	.000
Υ MC	.008	.002	.000	.011	.002	.000
Double Decay MC	.003	.001	.000	.000	.004	.000
MC Statistics	.039	.017	.005	.018	.015	.000
Total Error	.057	.022	.006	.027	.035	.003

Table 6-3: The systematic errors associated with the Monte Carlo predictions for the relative contribution of dimuon events in the final data sample from each of the six categories which effect the ratio of like to unlike sign events in the sample.

independently with respect to the uncertainties in the other parameters. First, a correction factor to the cross sectional weight of each event in the Monte Carlo samples was determined based on a modification of the particular parameter under consideration to the upper or lower limit of its uncertainty range. For example, if the value of the b quark direct semileptonic branching ratio in the Monte Carlo event generator was raised to the upper limit of its error range (+ 5%), the cross sectional weight of individual Monte Carlo events was increased 5% for each muon within the event which resulted from the direct semileptonic decay of a b quark.

Upon modification of the cross sectional weights assigned to each of the events in the Monte Carlo samples, the Monte Carlo predictions for the relative contributions of the six dimuon event categories to the final data sample were recalculated based on the modified weights using the method discussed in Section 5.5. The difference between the Monte Carlo predictions for the relative contributions of the six categories to the final event sample from reweighted event samples and

that from the original Monte Carlo sample was used to set the error range of each parameter. It is important to note that the modification of a single Monte Carlo parameter often had a correlated effect on the relative contributions of different dimuon production mechanisms to the final event sample. For example, since over 90% of the events in the final data sample were predicted to contain at least one muon produced in the decay of a $b\bar{b}$ quark pair, increasing f_b to the upper limit of its uncertainty range (+ 12%) had only a minimal effect on the Monte Carlo prediction for the relative contributions of the six dimuon categories to the final event sample.

The complete set of systematic errors associated with the Monte Carlo predictions for the relative contributions of the six dimuon event categories to the final event sample are shown in Table 6-3. Since a reweighted calculation of these parameters was performed based on the modified values of each individual Monte Carlo parameter at both the upper and lower limits of its uncertainty range, the systematic errors were taken as the larger difference observed in each relative contribution. The total systematic errors were determined by adding the individual errors in quadrature.

Chapter 7

Conclusions

7.1 Result for χ

Using a sample of 183 dimuon events collected with the DØ detector during the 1992-1993 collider run at the Fermilab Tevatron, we have measured the time and flavor averaged $B^\circ - \bar{B}^\circ$ mixing probability χ. The dimuon event sample utilized for this measurement was chosen using a series of selection criteria designed to enhance the fraction of events produced in the direct semileptonic decays of both quarks in a $b\bar{b}$ pair. The dimuon invariant mass range was restricted to 6 GeV/c^2 $< M_{\mu\mu} <$ 40 GeV/c^2 in order to reduce the relative contributions of events from J/ψ decays and events created in two semileptonic decays associated with a single b quark. To decrease the relative contributions from Υ decay and Drell-Yan production which result in isolated muons, each event was also required to have an associated jet with $E_T^{jet} > 12$ GeV. Furthermore, each muon with an associated jet was also required to have a transverse momentum relative to its associated jet axis greater than 1.2 GeV/c which served to increase the fraction of muons in the sample which were produced in the direct semileptonic decays of b quarks. Since the absolute magnitude of muon transverse momentum was also found on average to be higher for muons produced in the direct semileptonic decays of b quarks with respect to those produced in c quark and in-flight π/K decays, each muon was additionally

required to have $P_T^{\mu} > 4$ GeV/c.

The mixing probability χ was extracted from this measured ratio of like sign to opposite sign dimuons in the final event sample based on the relative contributions of the different dimuon production mechanisms to the sample as determined from Monte Carlo. The ratio of like sign to opposite sign dimuons in the event sample was corrected for cosmic ray background based on independent maximum likelihood fits to the floating t_o parameter as defined in Section 5.4.1 for muon tracks in the like and opposite sign dimuon event samples. After cosmic ray background subtraction, a total of 168 events remained with a like to unlike sign ratio of $R = 49/119 = 0.41$.

The relative contribution of each dimuon production mechanism to the final event sample was determined from a full Monte Carlo simulation of the different processes. Next, the relative fractions of events in the final dimuon sample associated with each of the six dimuon categories which define the ratio of like to unlike sign events in the sample (P1-P6) were then extracted from the relative contributions of the different dimuon production mechanisms using the relationships shown in Table 5-1. The fraction of events associated with each production mechanism in which one muon is reconstructed with a wrong sign were assigned to the event category with the opposite ratio of like sign to opposite sign events. As a reference the relative contributions of the six event categories to the final dimuon sample as determined from Monte Carlo are listed in Table 7-1 along with the corresponding errors determined from the complete set of Monte Carlo uncertainties.

The result for the time and flavor averaged $B^o - \bar{B}^o$ mixing probability χ was extracted from the cosmic ray background corrected ratio of like sign to opposite sign events in the final dimuon sample as presented in (5.7) using the values for P1-P6 given in Table 7-1. The resulting value for χ which was obtained as the

Label	Primary Process	Fractional Contribution	Total Error
P1	$b \rightarrow \mu^-, \bar{b} \rightarrow \mu^+$	0.66	0.06
P2	$b \rightarrow c \rightarrow \mu^+, \bar{b} \rightarrow \mu^+$	0.14	0.02
P3	$b \rightarrow c \rightarrow \mu^+, \bar{b} \rightarrow \bar{c} \rightarrow \mu^-$	0.01	0.01
P4	$c \rightarrow \mu^+, \bar{c} \rightarrow \mu^-$	0.06	0.03
P5	π,$K \rightarrow \mu$ background	0.13	0.04
P6	-	0.00	0.00

Table 7-1: Monte Carlo predictions for the relative fraction of events in the final data sample from each of the six event categories which define the measured ratio of like to unlike sign events in the sample and the corresponding errors determined from the complete set of Monte Carlo uncertainties.

solution to the quadratic equation shown in (5.2) is

$$\chi = 0.09 \pm 0.04(stat) \pm 0.03(sys). \tag{7.1}$$

The systematic error in this result is due both to uncertainties in the method used to determine the cosmic background in the final event sample and to the complete set of uncertainties associated with the Monte Carlo predictions for the relative contribution of events to the final data sample from each of the six categories (P1-P6). The largest single contribution to the systematic errors is the statistical errors associated with the Monte Carlo samples. However, the total systematic error is smaller than the statistical error of the result.

A comparison of this result to other recent measurements of the $B^\circ - \bar{B}^\circ$ mixing probability χ obtained from collider experiments which observe $b\bar{b}$ quark pairs produced above the b-production threshold [16][17][18][19][20][21][22] is shown in Fig. 7-1. The LEP measurements are not directly comparable to those made at the Fermilab Tevatron since the values of f_d and f_s depend on the hadron mixture which results from the fragmentation of $b\bar{b}$ quark pairs. This fragmentation is not necessarily identical for $b\bar{b}$ pairs produced in e^+e^- and $p\bar{p}$ collisions due in part to

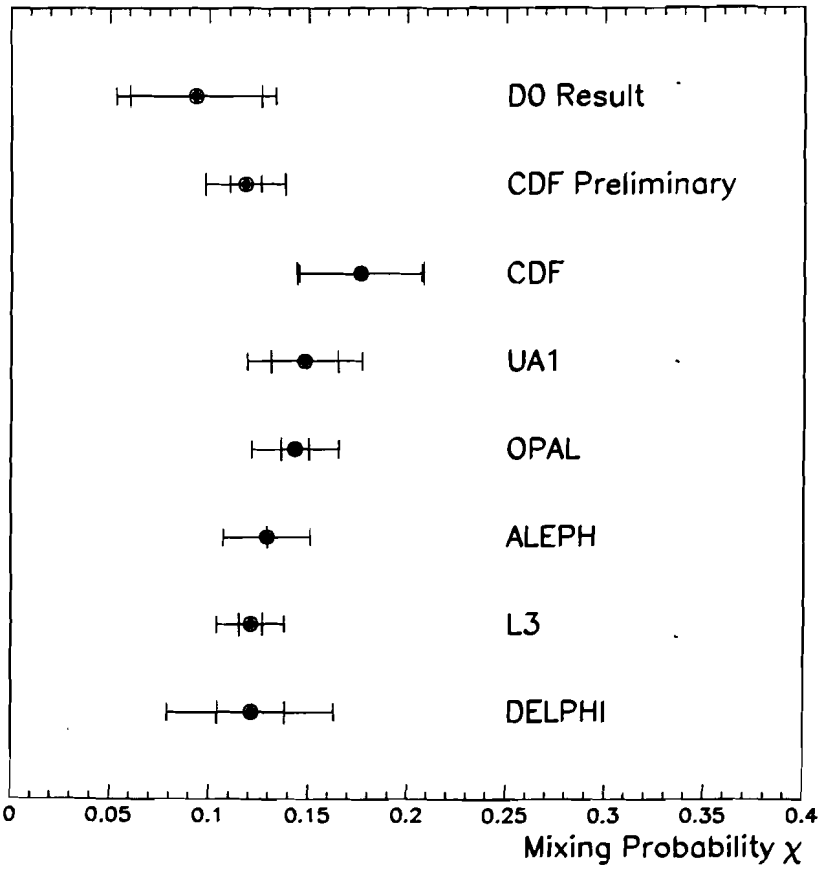

Figure 7-1: Comparison of the DØ result for the mixing probability χ with other recent experimental measurements of this parameter obtained from collider experiments which also observe $b\bar{b}$ pairs produced above the b-production threshold.

the fact that the b quark energies are slightly different. However, the differences in f_d and f_s are thought to be small with respect to the present scale of the errors associated with these measurements. In general, the DØ result for the mixing probability χ is in good agreement with other recent experimental results within the uncertainties of the measurements.

7.2 B_s Mixing

As previously discussed the $B^\circ - \bar{B}^\circ$ mixing probability which is measured using dimuon events collected with the DØ detector is a combined mixing probability averaged over all b hadron flavors. As shown in (1.23) this measured parameter can be defined in terms of the fundamental mixing probabilities for B_d° and B_s° mesons based on the relative contributions of each b hadron flavor to the mixture of mesons and baryons which are produced in the fragmentation of the individual b quarks. Since the value of the B_d° mixing probability χ_d is determined from experimental measurements utilizing b meson pairs produced at the Υ (4s) resonance [13][14][15], an extraction of the B_s° mixing probability χ_s using a new world average for the flavor averaged mixing probability χ which included the DØ result was possible.

A lower limit on the B_s° mixing probability χ_s was obtained using the new world average for the flavor averaged mixing probability χ in which the DØ measurement was included in conjunction with the present world average for the B_d° mixing probability χ_d [45]. The normalized contributions of the different b hadron flavors to the mixture produced in $p\bar{p}$ collisions at $\sqrt{s} = 1.8$ TeV were estimated to be $f_u : f_d : f_s : f_\lambda = 0.375 : 0.375 : 0.15 : 0.10$ as discussed in Section 1.4.2. A graphical illustration of the allowed values of the B_s° mixing probability χ_s is shown in Fig. 7-2. The two dotted lines indicate the present uncertainty range associated with experimental measurements of the B_d° mixing probability χ_d. The relationship between χ_d and χ_s is constrained to the region between the two dashed

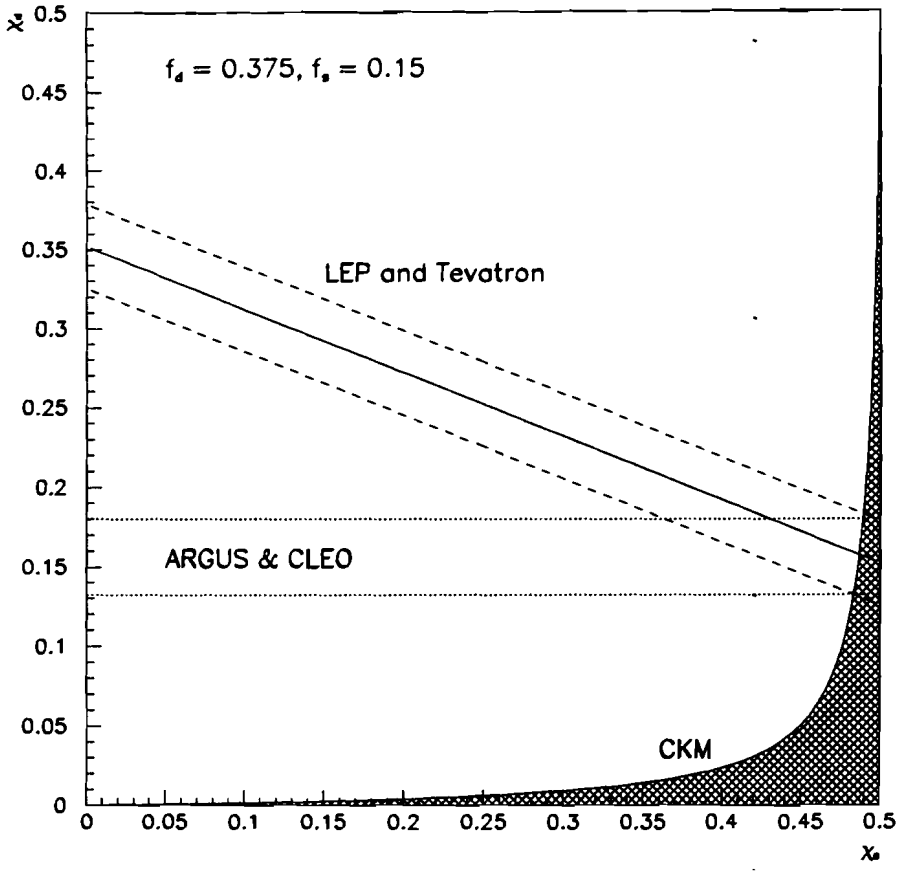

Figure 7-2: Graphical illustration of the the method utilized to extract a lower limit on the B_s° mixing probability χ_s using the new world average for the combined mixing probability χ which includes the DØ measurement in conjunction with the world average value for the B_d° mixing probability χ_d.

lines in the figure based on the new world average result for the flavor averaged mixing probability and the b hadron fractions given above. A large value for the B_s° mixing probability χ_s is suggested from the overlap in the region of the constrained relationship between χ_d and χ_s with the uncertainty range associated with experimental measurements of χ_d. The allowed relationship between χ_d and χ_s based on Standard Model constraints obtained from experimental measurements of the CKM matrix elements is indicated with the hatched region in Fig. 7-2. Based on the experimental measurements described here, the Standard Model relationship between χ_d and χ_s is satisfied only if the value of χ_s is near its maximum value.

Appendix A

The Maximum Likelihood Fit Method

The maximum likelihood fit method which was utilized several times in this analysis to extract the relative contributions of different contributing processes to specific event samples based on the distributions of different parameters associated with the events in those samples is described in detail in this section. In order to determine the fraction of the sample, A_j, from each of the contributing processes, j, $j = 1, \ldots, j_n$, which contribute to a sample, it was necessary to maximize the log-likelihood function

$$L = \ln \mathcal{L} \tag{A.1}$$

with respect to the variables A_j. The likelihood function, $\mathcal{L}$, is given by

$$\mathcal{L} = \prod_{i=1}^{i_n} \left[\sum_{j=1}^{j_n} A_j \prod_{k=1}^{k_n} v_k^j(x_k^i) \right] \tag{A.2}$$

where the functions $v_k^j(x_k)$, $k = 1, \ldots, k_n$ are the probability distributions for the variables x_k and the product in i is over all i_n events. The parameters A_j are subject to the normalization constraint

$$\sum_{j=1}^{j_n} A_j = 1. \tag{A.3}$$

This condition is included by transforming to a set of $j_n - 1$ independent parameters, θ_j, where $0 < \theta_j < 1$. For example, in a fit to four contributing processes, the transformation is given by the following set of equations:

$$\begin{aligned} A_1 &= \theta_1 \\ A_2 &= (1-\theta_1)\cdot\theta_2 \\ A_3 &= (1-\theta_1)\cdot(1-\theta_2)\cdot\theta_3 \\ A_4 &= (1-\theta_1)\cdot(1-\theta_2)\cdot(1-\theta_3). \end{aligned} \tag{A.4}$$

Note that these equations satisfy the normalization condition (A.3). The CERNLIB package MINUIT was used to find the minimum of L with respect to the parameters θ_j. The required set of conditions are that the derivative with respect to each variable be zero.

$$\frac{\partial(-2\cdot\ln L)}{\partial\theta_j} = 0, \quad j = 1,\ldots,j_n - 1. \tag{A.5}$$

The minus sign is necessary because the MINUIT program finds the minimum, not the maximum of a function. The factor of two is included so that a change of $\Delta(-2\cdot\ln L) = +1$ from the minimum value of the function corresponds to 1σ Gaussian errors on A_j. The MINOS error analysis package called from MINUIT finds the contour in the j_n-dimensional space which corresponds to $\Delta(-2\cdot\ln L) = +1$ above the minimum, and determines the maximum deviation in each of the variables θ_j along this contour. In general, this contour will not be symmetric in the variables θ_j and therefore the upper and lower errors will often be asymmetric.

REFERENCES

[1] C. N. Yang and R. L. Mills, Phys. Rev. **96**, 191 (1954).

[2] S. Abachi *et al.* (DØ Collaboration), Phys. Rev. Lett. **74**, 2632 (1995).

[3] F. Abe *et al.* (CDF Collaboration), Phys. Rev. Lett. **74**, 2626 (1995).

[4] P. Abreu *et al.* (DELPHI Collaboration), Nucl. Phys. **B418**, 403 (1994).

[5] X. Acciarri *et al.* (L3 Collaboration), Z. Phys. **C62**, 551 (1994).

[6] R. Akers *et al.* (OPAL Collaboration), Z. Phys. **C61**, 19 (1994).

[7] D. Buskulic *et al.* (ALEPH Collaboration), Z. Phys. **C62**, 539 (1994).

[8] J. Revol, "Future Neutrino Oscillation Experiments", CERN-PPE/93-84 (1993).

[9] P. W. Higgs, Phys. Lett. **12**, 132 (1964) ; Phys. Rev. Lett. **13**, 508 (1964).

[10] H. G. Moser, "B Mixing", CERN-PPE/93-164 (1993).

[11] L. Wolfenstein, Phys. Rev. Lett. **51**, 1945 (1983).

[12] A. Ali and D. London, "Prospects for Measuring the $B_s\overline{B}_s$ Mixing Ratio χ_s", DESY/92-152 (1992) ; A. Ali, "$B^\circ - \bar{B}^\circ$ Mixing and Rare B-Decays", DESY/92-152 (1992).

[13] H. Albrecht *et al.* (ARGUS Collaboration), Phys. Lett. **B324**, 249 (1994).

[14] J. Bartelt *et al.* (CLEO Collaboration), Phys. Rev. Lett. **71**, 1680 (1993).

[15] H. Albrecht *et al.* (ARGUS Collaboration), Z. Phys. **C55**, 357 (1992).

[16] F. Bedeschi *et al.* (CDF Collaboration), Proceedings of the 1995 $p\bar{p}$ Collider Workshop, Fermilab (1995).

[17] F. Abe *et al.* (CDF Collaboration), Phys. Rev. Lett. **67**, 3351 (1991).

[18] C. Albajar *et al.* (UA1 Collaboration), Phys. Lett. **B262**, 171 (1991).

[19] R. Akers *et al.* (OPAL Collaboration), Z. Phys. **C60**, 199 (1993).

[20] D. Buskulic *et al.* (ALEPH Collaboration), Phys. Lett. **B284**, 177 (1992).

[21] B. Adeva *et al.* (L3 Collaboration), Phys. Lett. **B288**, 395 (1992).

[22] P. Abreu *et al.* (DELPHI Collaboration), Phys. Lett. **B301**, 145 (1993).

[23] A. Breakstone *et al.*, Phys. Lett. **B135**, 510 (1984).

[24] S. Abachi *et al.* (DØ Collaboration), Nucl. Instr. Meth., **A338**, 185 (1994).

[25] J. Thompson, "Introduction to Colliding Beams at Fermilab", DØ Internal Note # 2367, (unpublished).

[26] UAZHEP::USR$ROOT1:[JAMES.THESIS]BAD_RUN.LST

[27] CAFIX DØLIBRARY program package.

[28] LUMIN_UTIL DØLIBRARY program.

[29] H. T. Diehl, "Cosmic Ray Muon Rejection in the Level 2 Filter at DØ ", DØ Internal Note # 1517, (unpublished).

[30] N. J. Hadley, "Cone Algorithm for Jet Finding", DØ Internal Note # 904, (unpublished).

[31] R. Astur, "Study of Fake Jets in the DØ Detector", DØ Internal Note # 1662, (unpublished).

[32] R. Astur, J. Blazey, and D. Elvira, "A Study of standard Jet Cuts and their Efficiencies using DØ Collider Data", DØ Internal Note # 1763, (unpublished).

[33] A. Milder, PhD thesis, Arizona University, unpublished (1993).

[34] F. Paige and S. Protopopesco, "ISAJET 7.13. A Monte Carlo event generator for pp and $p\bar{p}$ Interactions", Fermilab Computing Division, PM0059 (1992).

[35] L. Song, PhD thesis, University of Pennsylvania, unpublished (1991).

[36] S. Abachi *et al.* (DØ Collaboration), Phys. Rev. Lett. **74**, 3548 (1995).

[37] F. Abe *et al.* (CDF Collaboration), Phys. Rev. Lett. **68**, 3403 (1992) ; Phys. Rev. Lett. **69**, 3704 (1992) ; Phys. Rev. Lett. **71**, 500, 2396, 2537 (1993); Phys. Rev. **D50**, 4258 (1994).

[38] P. Nason, S. Dawson, and R. K. Ellis, Nucl. Phys. **B327**, 49 (1989).

[39] A. Smith, PhD thesis, Arizona University, unpublished (1995).

[40] F. Abe *et al.* (CDF Collaboration), Phys. Rev. Lett. **61**, 1819 (1988).

[41] T. Huehn, PhD thesis, University of California Riverside, unpublished (1995).

[42] D. Hedin, P. Quintas, and D. Wood, "Muon Wide Angle Chamber Efficiencies in Run Ia", DØ Internal Note # 2127, (unpublished).

[43] C. Murphy, PhD thesis, Indiana University, unpublished (1995).

[44] M. Mangano, Program HQOUNW.FOR, described in "Quarkonium Production Codes: Documentation", (unpublished).

[45] L. Montanet *et al.* (Particle Data Group), Phys. Rev. D **50**, 1173 (1994).

[46] R. Akers *et al.* (OPAL Collaboration), Z. Phys. **C60**, 199 (1993).

[47] W. Venus, " *b* Weak Interaction Physics in High Energy Experiments", AIP Conference Proceedings, Lepton and Photon Interactions, XVI International Symposium, 274 (1993).

[48] H. Albrecht *et al.* (ARGUS Collaboration), Phys. Lett. **B278**, 202 (1992).